UNIVERSITY OF BIRMINGHAM

Nanoparticle Catalysts for Proton Exchange Membrane Fuel Cells: A Study of Surfactant Effects on Dispersion and Catalysis

A Thesis submitted in partial fulfilment of the requirements for the degree Doctor of Philosophy at the University of Birmingham (United Kingdom)

School of Chemical Engineering

by

Jill Elizabeth Newton

June 2014

Acknowledgements

I would like to thank my supervisors: Jon Preece, who has been a consistent source of encouragement throughout, Kevin Kendall who inspired me at the start and Neil Rees who has helped me with the writing. I would also like to thank Sarah Horswell, who although not my official supervisor, gave invaluable help with electrochemistry.

I would like to thank all the students and staff, in both the Chemistry and Chemical Engineering Departments, who have helped and encouraged me.

I also thank the EPSRC for funding this work.

Finally, I thank my three sons, William, David and Richard and I dedicate this thesis in memory of their father Robert Newton, who encouraged me to start this PhD but died before I had finished.

Abstract

Carbon-supported Pt nanoparticles are currently the most effective catalysts used in proton exchange membrane fuel cells (PEMFCs). Because Pt is expensive, minimisation of Pt loading is necessary to achieve large-scale commercialisation of PEMFCs. Nanoparticle aggregation is a problem because well-dispersed nanoparticles have a higher available surface area and so exhibit higher mass activity than aggregated nanoparticles.

There are many complex factors affecting the activity of catalysts in fuel cells. It is often difficult to examine these factors in isolation. The introductory chapters discuss these factors and the work of previous authors. In the present work, an aqueous colloidal route was chosen for the catalyst preparation. A range of anionic, non-ionic and polymeric stabilizers was used to give colloidal stability by attaching to the surfaces and preventing particle aggregation. Such organic molecules which adsorb on the surface of nanoparticles are generally regarded as undesirable species which block catalytic sites and slow reaction kinetics. The surfactants or polymers used to stabilise nanoparticles are usually removed by washing or heating before electrochemical testing. Many studies have focused on finding the most efficient method of surfactant removal [1, 2]. However, the removal processes, such as heating or solvent washing, are likely to lead to particle aggregation and so it would be advantageous if Pt nanoparticles could be utilised in catalytic reactions without extensive cleaning procedures.

The key question addressed in this thesis is ‘Are the surfactants giving beneficial dispersion, or causing damaging catalyst blockage?’

In this work platinum nanoparticles were successfully prepared using tetradecyltrimethylammonium bromide (TTAB), cetyltrimethylammonium bromide (CTAB), polyvinylpyrrolidone and nonylphenolethoxylate (NP9). Preparations using anionic surfactants were unsuccessful. Gold/platinum nanoparticles were successfully prepared by reducing chloroplatinic acid in the presence of a gold seed.

The aggregation behaviour of the particles was studied using transmission electron microscopy (TEM), Nanosight [3] and dynamic light scattering (DLS). The performance of a few of these catalysts was studied by using a rotating disc electrode (RDE). Electrochemical testing showed that TTAB had a strong poisoning effect on the platinum catalytic activity for the oxygen reduction reaction (ORR). Nanoparticles prepared using NP9 surfactant had catalytic activity similar to the commercial catalyst TKK. To test the catalyst blocking effect, several nonionic surfactants were adsorbed onto the Pt RDE, and their ORR performance was studied, confirming the importance of surfactant structure on catalyst performance.

Finally the performance of the Pt+NP9 nanoparticles was compared with the commercial catalyst TKK using single cell MEA testing. The main difference in performance was in the mass transport region of the polarisation curve. The

conclusion was that surfactant stabilization of Pt nanoparticles is important to fuel cell performance, while subtle effects of molecular structure on catalytic activity require more investigation.

List of Publications from this work

[1] J. Newton, J. Preece, N. Rees, S. Horswell, Physical Chemistry Chemical Physics, 16 (2014) 11435-11446.

[2] J.E. Newton, J.A. Preece, B.G. Pollet, International Journal of Low-Carbon Technologies, 7 (2012) 38-43.

Contents

Index of Figures

Index of Tables

Abbreviations

AFM Atomic force microscopy

BriJ O10 Decaethylene glycol oleyl ether

cmc Critical micelle concentration

CV Cyclic voltammogram

CTAB Cetyltrimethylammonium bromide

CTAOH Hexadecyltrimethylammonium hydroxide

DLS Dynamic Light Scattering

DLVO Derjaguin and Landau, Verwey and Overbeek.

ECSA Electrochemical Surface Area)

EIS Electrochemical Impedance Spectroscopy

EDX Energy-dispersive X-ray Spectroscopy

GC Glassy Carbon

GDE Gas Diffusion Electrode

GDL Gas Diffusion Layer

HAADF-STEM High angle annular dark field – scanning transmission electron microscopy

HOR Hydrogen Oxidation Reaction

HRTEM High resolution transmission electron microscopy

H_{upd} Underpotentially-deposited hydrogen

LSV Linear sweep voltammogram

MEA Membrane Electrode Assembly

Milli-Q water Deionised water with a conductivity of 18.2MΩ.cm

Nafion® is a registered trademark of E. I. Du Pont de Nemours and Company ,it is an ionomer derived from polytetrafluroethylene, containing sulfonic acid.

NP9 nonylphenol ethoxylate

ORR Oxygen Reduction Reaction

PFA Pentadecafluorooctanoic acid

PEMFC Proton Exchange Membrane Fuel Cell or Polymer Electrolyte Membrane Fuel Cell

PVP Polyvinylpyrolydone

RDE Rotating Disc Electrode

RHE Reversible Hydrogen Electrode. Potentials throughout this paper are quoted against this reference electrode, unless otherwise stated.

rpm Revolutions per minute

RRDE Rotating Ring-Disc Electrode

SDS Sodium dodecyl sulphate

SHE Standard Hydrogen Electrode

TEM Transmission Electron Microscopy

TGA Thermogravimetric Analysis

TKK Tanaka Kikinzoku Kogyo (Japan).

TTAB Tetradecyltrimethylammonium bromide

HRTEM, HAADF-STEM and EDX

Chapter 1 Introduction

1.1 Energy Landscape

Energy and transport systems are now based mainly on fossil fuels and are not sustainable. Depletion of world oil reserves and the need to reduce carbon dioxide emissions are driving the development of alternative energy technologies.

Energy requirements are expected to continue to rise in the coming decades [4], driven by the increasing industrialisation of developing countries and continued growth in the world's population, particularly in Asia and South America. Global oil supplies are limited and it is estimated that the end of the petroleum supply will probably take place around 2050 [5], considering the rate of growth of oil consumption and the rate of increase of known oil reserves. Natural gas could be an alternative, in the medium term, but supplies of this are also limited (70–100 years). Coal is the only fossil fuel expected to be available for another couple of centuries.

Global oil and gas reserves are concentrated in a few regions of the world. Many of these regions have a tendency to political instability and this has encouraged the UK to gain more energy from renewable sources and become less reliant on politically unstable countries.

Most scientists and politicians agree that greenhouse gas emissions, which keep rising, are leading to global warming and need to be reduced in order to prevent dangerous consequences, for example, sea level rises and extreme weather events. It has been estimated [6], that 80% reduction of CO_2 emissions by 2050 may require 95% decarbonisation of road transport. Local air pollution, especially from road transport, is a major issue in the world's largest cities. Reduction in the burning of fossil fuels in road transport will reduce levels of particulates and NO_2, which are bad for our health. We need to find ways to provide the energy required for our economy and reduce emissions. Reduction in energy consumption by increased efficiency and reduced wastage is one obvious way to achieve this. For example, walking, cycling and use of Public Transport rather than cars.

Oil sands and oil shale [7], gas produced by fracking, synthetic Fischer-Tropsch fuels and bio-fuels are all alternatives to conventional oil production. They have high volumetric energy density and can use the existing distribution and refuelling infrastructure. However, these fuels do not reduce CO_2 emissions. Most of these also have other serious environmental impacts.

The ideal energy sources are renewable such as wind, solar, tidal, geothermal and wave power. However, energy production from renewable sources is intermittent. At certain times of day production is greater than demand. Instead of this energy being wasted, it can be stored [8-10] by means such as: compressed air energy storage, pumped hydro energy storage or batteries. The energy can also be used to produce hydrogen from water by electrolysis and hydrogen acts as an energy

storage vector. The different types of energy storage entail varying energy losses, environmental impacts and cost. The energy stored in hydrogen can be efficiently used in transport, where the energy needs to be stored before use. For most stationary applications it is more efficient to feed the energy from renewable sources into the electricity grid and use it directly.

1.2 The Hydrogen Economy

At present hydrogen is mostly produced from fossil fuels; natural gas, oil, and coal, using production processes which release CO_2. However, if used in combination with carbon capture technology, this hydrogen may be a useful stepping stone to the hydrogen economy and CO_2 reductions.

Hydrogen is the most abundant element in the known universe. The use of hydrogen and the vision of a hydrogen economy are not new. Until the 1960s town gas, containing a high proportion of hydrogen [11] was used in many countries for street lighting as well as for home energy supply, for cooking and heating.

Hydrogen is an explosive gas but the energy stored in hydrogen can be safely and efficiently converted to electricity using fuel cells. The only by products are water and a small amount of heat. Hydrogen can be used in many different applications (mobile, stationary and portable) but the transport sector is likely to play the most important role for the possible introduction of hydrogen. Fuel cells have high conversion efficiencies compared to the internal combustion engine and hydrogen

offers a range of benefits as a clean energy carrier. At the point of final use the main emission is water. In the long term hydrogen could be produced entirely from renewable energies.

There are several barriers to the widespread introduction of hydrogen fuel cells, and a hydrogen economy. Criticisms of the hydrogen economy include several objections: currently most hydrogen is produced from natural gas which is not a renewable resource and releases CO_2, into the environment, unless carbon capture technology is used. The electrolysis used to convert renewable forms of energy into hydrogen is inefficient. Also hydrogen is not easily stored or distributed and the cost of setting up a hydrogen based infrastructure to replace the existing oil based infrastructure is very high. There are also safety issues with hydrogen which is a flammable gas with a very wide range of explosive mixture compositions in O_2/air. Also hydrogen fuel cells are complex and expensive. Platinum is currently the most effective catalyst in proton exchange membrane (PEM) fuel cells which are used in cars, but it is very expensive and worldwide supply is limited.

The work in this thesis will address the use of platinum in fuel cells. At present hydrogen fuel cells for transport are expensive compared to combustion engines powered by hydrocarbon fuels. Reduction in platinum loadings will allow costs to be reduced.

At present (2014) there are some commercial fuel cell systems available, but many more applications are being developed. For example, fuel cell cars, taxis, and

buses are being demonstrated worldwide, but these are very expensive. Fuel cell systems which have a technological advantage over existing systems are the ones which are progressing to market, for example hydrogen fuel cell fork lift trucks are non-polluting and quiet, and can be easily refuelled on site. These factors are particularly important when working inside a warehouse. Small, mobile fuel cells are also being developed for use as battery chargers for applications such as computers and mobile phones. Niche applications such as delivery trucks, taxis, and other fleet vehicles can help demonstrate the viability of hydrogen and fuel cells for mobile applications. For example, hydrogen fuel cell buses were operating in London during the 2012 Olympic Games. These demonstrated to the public that hydrogen buses work and are safe. The Mckinsey Report [6] says that fuel cell vehicles, battery electric vehicles and petrol hybrid electric vehicles will all be necessary going forward to wean the consumer from fossil fuelled vehicles and each will have a place in the marketplace.

Technological development must bring about a reduction in the costs of hydrogen production, distribution, storage and utilisation before the hydrogen economy can be successful. An alternative to the hydrogen economy could use renewable energy as the electricity source and employ hybrid systems based on conventional lithium batteries and bio-fuels to power its cars. This system however has many problems; bio-fuels reduce land available for food growth, batteries do not hold their charge and battery cars do not have the driving range to satisfy consumers.

The International Energy Agency (IEA) [12] has analysed several political and technological scenarios for the future. In the most favourable situation for the development of a hydrogen economy (ESTEC D) global hydrogen usage for energy will begin to increase rapidly in 2020. In 2050 30% of the cars will be powered by hydrogen fuel cells and there will be a capacity of 200–300 GW in installed fuel cells to cogenerate heat and electricity in the residential sector. By 2050 there is expected to be a diversified network of energy sources and reduced reliance on fossil fuels. Hydrogen and other clean technologies including carbon capture and electricity from renewable energies can help to stabilize CO_2 emissions to the atmosphere.

Mackay [13] discusses possible ways of providing our energy requirements without producing CO_2, of which there are many, all relying on a range of energy sources. He points out that it is very unlikely that we will be able to meet our energy requirements totally from our own renewable sources. Two of his scenarios either include significant uses of nuclear energy or solar power from the Sahara desert.

1.3 Fuel Cells

A fuel cell is an electrochemical device in which the chemical energy of a fuel is converted directly into electrical energy. The fuel is typically an alcohol, a hydrocarbon or hydrogen and is supplied continuously. The fuel cell has an anode at which the fuel is electrocatalytically oxidised with the production of electrons and a cathode at which the oxygen is reduced. Different types of fuel cells run on

different fuels and are useful for different applications. Some of the properties are summarized in Table 1.1.

This project will concentrate on proton-exchange membrane fuel cells (PEMFCs) which often run on pure hydrogen. These are promising for use in transport applications, due to their rapid start up time and low operating temperature compared to other types of fuel cell.

Penetration of PEM fuel cell technology into the market place has been limited by cost and reliability issues. A worldwide effort has been underway to develop catalysts and membranes and to study long term behaviour of fuel cells. So far (2014) fuel cell market penetration has been limited: some of the barriers to be overcome are discussed in Section 1.2. In the early 1960s, the first PEM systems were used in the Gemini space missions as power plants. However, the cell membranes, which consisted of a copolymer of sulphonated polystyrene and divinylbenzene, were prone to degradation.

Table 1-1 *The most common types of fuel cells, characterised by electrolyte [14]*

Fuel cell type	Electrolyte	Operating Temp. /º C	Fuel	Start up time
Proton-exchange membrane	polymer	50-80	Pure hydrogen, formic acid	seconds
Direct methanol	Polymer	60–200	Liquid methanol	seconds
Phosphoric acid	Phosphoric acid	160-210	Hydrogen and alcohol	hours
Alkaline	Potassium hydroxide	50–200	Pure hydrogen, hydrazine, NH_3	minutes
Molten carbonate	Molten carbonate	630–650	propane, marine diesel	hours
Solid oxide	Stabilized zirconia	500-1000	Hydrogen, Methane, propane, butane,	minutes-hours

1.3.1 Advantages of PEMFC's

Fuel cells offer many advantages over conventional energy conversion devices [15, 16]. As they use an externally supplied fuel, they can be compared to traditional generators or combustion engines which burn the fuel. The following characteristics make the PEMFC a possible alternative to conventional energy conversion systems [15],[17-19].

Efficiency: Because the PEMFC converts chemical energy directly into electrical energy, the efficiency of a practical fuel cell engine is typically, approximately 20

double that of a modern internal combustion engine [20]. Energy is lost in the combustion engine as a result of factors such as friction, heat transfer and inefficient combustion.

Low emissions: When pure hydrogen is used directly as a fuel, only water is produced and no pollutant is emitted at the point of use.

Cogeneration capability: The heat produced in exothermic electrochemical reactions can be used.

Scalability: They can be used as a power source for vehicles, small or large power plants as well as portable electronics and computers.

Reliability and low maintenance: There are no moving parts and so maintenance requirements are minimized.

Quiet operation: The operation is quiet and there is no noise pollution.

1.3.2 Challenges for PEMFC's

There are significant barriers facing the commercialization of fuel cells. These include:

Cost: They are currently more expensive than the alternatives; the cost of platinum used as a catalyst is high.

Fuel supply: PEMFCs require extremely pure hydrogen and the processing of hydrocarbon fuels into hydrogen can result in a small output of NO_x, SO_x, CO, and CO_2.

Durability: Fuel cell systems are required to operate at 40-80 $^{\circ}$C for transport systems and -35 to 40 $^{\circ}$C for stationary systems. They must also be able to endure

5000 hours (150000 miles) for transport applications and 40000 hours for stationary applications.

Little current infrastructure: Currently there is little infrastructure for hydrogen fuel storage and distribution. Hydrogen is a low density gas and must be compressed or stored in a way that meets packaging requirements in vehicles.

Safety and public perception: Hydrogen is an explosive gas, it is not necessarily more dangerous than hydrocarbon fuels but issues of safety need to be addressed.

Availability: Platinum has limited worldwide supply.

1.3.3 Cost of Fuel Cells

The most expensive components of PEMFCs are the electrodes which account for over 30 % [21] of the overall cost of the fuel cell stack, although this has reduced from 50 % in 2007 [15]. The electrodes contain the electrocatalyst, which takes the form of nanometre-sized particles of platinum supported on a porous carbon substrate. Worldwide supply of platinum is limited, and it is expensive, and therefore reduction of platinum loading is one of the most important factors for commercial viability of PEMFC technology [22].

Many governments have set targets for the cost of fuel cell technologies [23, 24]. A 2014 article [25] suggests that the cost-per-kW generated using fuel cells will need to drop by a factor of 10 for fuel cells to enter the market. However once fuel cells are produced on a commercial scale the cost will drop significantly.

1.3.4 Availability of Platinum

Pure platinum catalysts are used for hydrogen-fuelled PEMFCs, while alloys of platinum with ruthenium are typically used for reformed hydrocarbon fuels to improve the tolerance of the catalyst to carbon monoxide.

South Africa was the main producer of platinum [26], in 2005, accounting for around 80 % of world production. Significant deposits are also found in Russia, Canada, Zimbabwe, the United States and Australia. South Africa has been expanding production rapidly to take advantage of increasing demand. A New Scientist article [26] estimated 'that there are 360 years of platinum reserves available, if we continue to extract it at the current rate of production. However, this drops to 15 years if predicted growth in demand is taken into account'. Some reports suggest [27] platinum availability should not be a constraint to the introduction of hydrogen fuel cell cars, but this is highly dependent on future demand for platinum. Platinum is a vital component of catalytic converters and of fuel cells, supplies are running out and the cost of platinum continues to rise.

Calculations suggest that if fuel cell vehicles achieve 50 % market penetration by 2050, the platinum industry has potential to meet the requirements but 80 % market penetration could exceed the capabilities of the industry. In this case, economic recycling of the Pt, to the required purity, will become important.

1.4 PEMFC Components

The main components of PEM fuel cells are: electrodes (anode and cathode), polymer electrolyte membrane (PEM), gas diffusion layer (GDL) and the flow field/current collector.

A schematic diagram of a membrane electrode assembly (MEA) is shown in Figure 1.1. This is composed of the electrodes, polymer electrolyte membrane and gas diffusion layers. It is the part of the fuel cell in which the chemical reactions take place. Hydrogen fuel is converted into protons (H^+) and electrons (e^-) at the interface between the anode catalyst, which is typically Pt based, and the electrolyte. The protons travel through a PEM, which does not conduct electrons, to the cathode side. The important property of a PEM is that it allows protons to diffuse but not electrons. The electrons travel through an external wire and deliver part of their energy to a 'load' on their way to the cathode. At the interface between the cathode catalyst, also typically Pt based, and the electrolyte, the protons and the electrons combine with oxygen to produce water. Gaseous oxygen or air is the most common choice for the oxidant because it is readily and economically available.

The hydrogen fuel cell uses H_2 gas as the fuel and provides very high fuel cell performance and efficiency for pure hydrogen. The direct methanol fuel cell uses liquid methanol as a fuel and gives lower efficiency efficiency, but methanol is more readily available and safer to use than pure hydrogen.

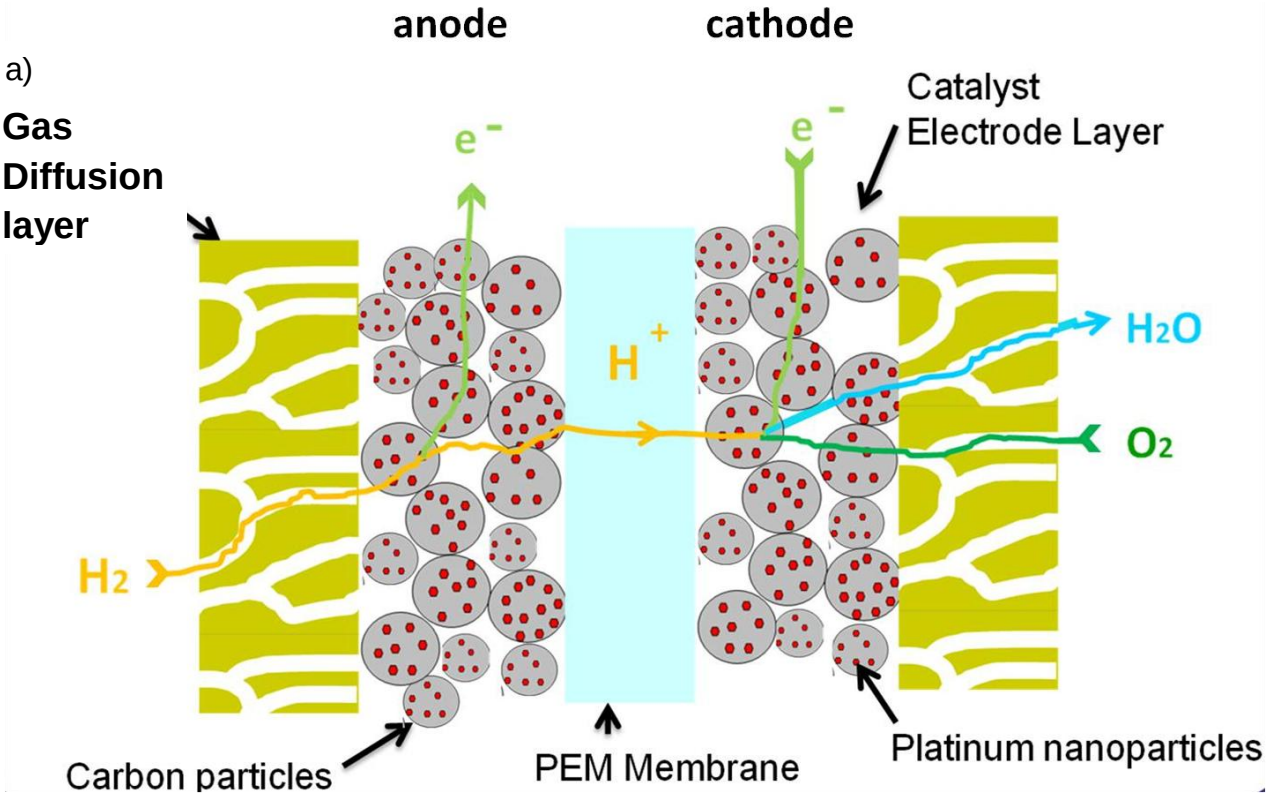

Figure 1-1 *a) Schematic cross section of a membrane electrode assembly b)expanded view depicting triple phase boundary*

1.4.1 Electrodes

The electrodes consist of platinum nanoparticles (3-5 nm) supported on carbon particles (30 μm) and mixed with proton conducting ionomeric material. The platinum acts as the catalyst for electrochemical reactions. The carbon acts as an electrically conductive support over which the catalyst is evenly distributed, and the pores allow gases to diffuse. On the top of each electrode layer is a 100-300 μm thick gas diffusion layer made from carbon cloth or porous carbon paper. Figure 1.1 shows the typical cross section of a membrane electrode assembly (MEA) showing the platinum supported on the carbon black. The catalyst layers within the PEMFC MEA are a fundamental component affecting many aspects of the fuel cell operation and performance.

Research into PEMFC catalysts, over the last 40 years, has resulted in significant reductions in platinum loading and increases in performance. Platinum black was used as the electrocatalyst, at the anode and cathode, in the first PEMFCs. The catalyst particle size was around 50-100 nm giving a physical surface area of Pt black catalysts of around 10 $m^2\ g^{-1}$ Pt. With these low specific surface areas, Pt loadings of > 4 mg Pt cm^{-2} were required to achieve useful power densities. By the 1990s [28, 29] Pt black catalysts were replaced by Pt nanoparticles supported on carbon. These consist of Pt nanoparticles (diameter < 10 nm) dispersed on a high surface-area carbon black. The surface area of the carbon black support is 300-1500 $m^2\ g^{-1}$. The high carbon surface area enables dispersion of Pt nanoparticles

up to metal loadings of 60 wt % Pt/C and Pt physical surface areas of 120 $m^2 g^{-1}$ Pt can be achieved.

Another significant development was the inclusion of proton-conducting polymer (ionomer) in the pore structure of the catalyst layer [30], in the 1980s, The catalyst layers are typically applied as an ink containing a mixture of Nafion® (ionomer) dispersion and the carbon-supported catalyst. The Nafion® increases the triple-phase contact between catalyst, ionomer and conductive carbon support [30-32]. This enables a greater proportion of catalyst to remain electrochemically active, since reactions only occur at regions where catalyst surfaces are in simultaneous contact with carbon black, proton-conducting polymer and reactant gases; this is shown in Figure 1.1b. For early PEMFC's based on Pt/C the triple phase boundaries were restricted to a thin layer at the interface between the polymer membrane and the catalyst layer. This meant that the remainder of the Pt catalyst was not in contact with the membrane and showed relatively low activity. PTFE is sometimes added on the cathode side to improve water management [33].

In PEM fuel cells, the type of fuel used dictates the appropriate type of catalyst needed. If the hydrogen is formed from fuel reforming, tolerance to carbon monoxide (CO) is an important issue. It has been shown that PEM fuel cell performance drops with a CO concentration of only a few parts per million due to the strong chemisorption of CO onto the catalyst. The best performance is obtained with pure hydrogen, which can be obtained from electrolysis of water.

1.4.2 Proton Exchange Membranes (PEM)

The important property of the PEM is that it allows protons to diffuse but not electrons. Early PEMs were based on sulphonated polystyrene but most modern membranes are made from perfluorinated sulphonated ionomer materials such as Nafion®, which is more chemically-resistant, with a structure shown in Figure 1.2. The polymer is based on a polytetrafluoroethylene (PTFE) backbone and has side chains, with sulphonic acid groups at the end [34]. This type of membrane has exceptional stability and has been extensively used in the chloralkali industry as it has good ion selectivity, chemical resistance and ionic conductivity. The typical thickness of the Nafion® membrane (Dupont) for fuel cell applications is between 50 and 175 microns. In the membrane the hydrophilic, sulfonated side chains cluster together, forming regions which, when adequately hydrated, facilitate transport of protons. Nafion® membranes need liquid water to remain hydrated, they do not operate well above 90 ºC. There is growing interest in operating PEMFCs at higher temperatures (120-200 ºC) in order to improve tolerance to impurities and water management. This has encouraged research into new PEM materials.

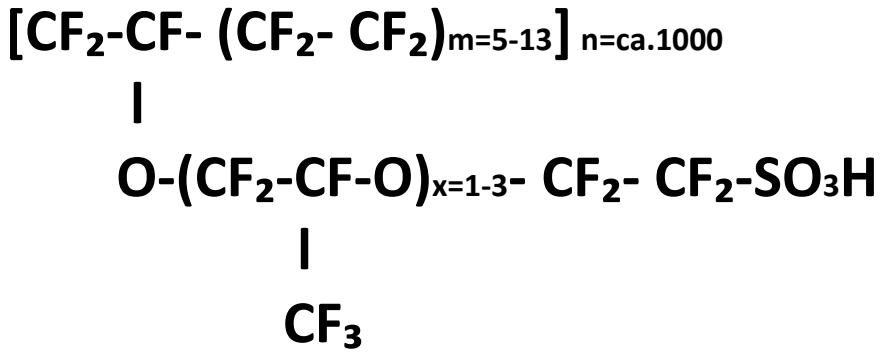

Figure 1-2 *Nafion® polymer, chemical structure*

Nafion® membranes formed from sheets of the sulphonyl fluoride polymer which is then hydrolysed to the sulphonate [35]. The sulphonated polymer membranes swell in some organic solvents. Nafion is extremely insoluble in most solvents but can be suspended in some mixed solvents.

1.4.3 Gas Diffusion Layer (GDL)

As shown in Figure 1.1 there are two GDLs, one next to the anode and the other next to the cathode. They are usually made of a porous carbon paper or carbon cloth, typically 100–300 μm thick [36]. The GDL material is porous and allows diffusion of each reactant gas to the catalyst on the membrane electrode assembly. The GDL also assists in water management during the operation of the fuel cell by enabling the liquid water produced at the cathode to leave the cell so that it does not flood. The GDL is treated with hydrophobic coating e.g. PTFE, to prevent clogging of its pores with water. The GDL should also allow an appropriate amount of water vapour to reach the membrane electrode assembly keeping the membrane humidified, improving the efficiency of the cell.

1.4.4 Flow field/ Current Collector

On the outer side of the MEA is the current collector plate. In most cells a flow field is machined in the current collector plate, which is designed to allow uniform gas supply to the electrodes and efficient removal of liquid water from the cathode. Various flow field geometries are commonly used, e.g., parallel channel flow, single

serpentine channel and series-parallel combinations [37]. The flow-field geometry is designed to allow uniform gas supply to the electrodes and effective liquid water removal from the cathode. In a PEMFC stack the current collector plate becomes the bipolar plate. It should have high electronic conductivity and be impermeable to oxygen and hydrogen gases. Bipolar plates are commonly made from graphite or metals like stainless steel or titanium. These materials are non-corrosive for fuel cell operations. The load containing circuit completes the PEM fuel cell [38].

1.4.5 Fuel Cell Stack

A single fuel cell will produce approximately 1 V, which isn't enough to power most devices, and so fuel cell manufacturers stack them together in series, from 10 to 100 in practice, separated by electrically-conducting plates. This assembly is illustrated in Figure 1.3 and is called a fuel cell stack. The electric potential of each cell is summed to give the electric potential of the whole stack.

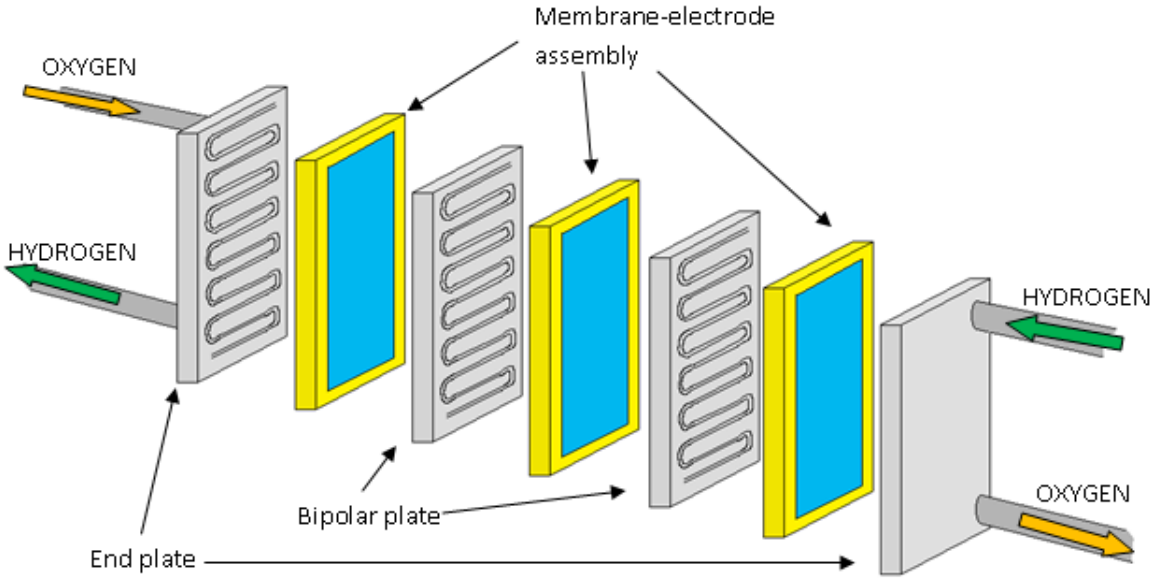

Figure 1-3 *An exploded view of a PEMFC stack composed of repeating cells of Membrane Electrode Assemblies [39] and bipolar gas-flow plates.*

Chapter 2 Electrocatalysis in the Direct-Hydrogen PEMFC

This Chapter describes the theoretical considerations that are relevant to electrocatalysis in the hydrogen fuel cell. For a fuel cell, the maximum energy available for conversion to useful (electrical) work is given by the Gibbs free energy change for the overall cell reaction. The half cell reactions (at 298K and 1 atm) for the hydrogen PEM fuel cell are as follows:

Anode: $H_2 \rightleftharpoons 2H^+ + 2e^-$ $\Delta G^0 = 0.00$ kJ/mol (2.1)

Cathode: $½O_2 + 2H^+ + 2e^- \rightleftharpoons H_2O$ $\Delta G^0 = -237$ kJ/mol (2.2)

Overall: $H_2 + ½O_2 \rightleftharpoons H_2O$ $\Delta G^0 = -237$ kJ/mol (2.3)

The Gibbs free energy change is a function of temperature and reactant concentration (or partial pressure for gaseous reactants) according to

$$\Delta G = \Delta G^{o} + RT \ln \left[\frac{p_{H2O}}{p_{H2} . p_{O2}{}^{½}} \right] \quad (2.4)$$

The Gibbs free energy change of a chemical reaction is correlated to the cell voltage as:

$$\Delta G = -nFE_{eq} \quad (2.5)$$

Where n is the number of electrons involved in the reaction, F is the Faraday constant, and E_{eq} is the cell voltage for thermodynamic equilibrium in the absence of a current flow i.e., open circuit conditions, at equilibrium.

Hence, the equilibrium cell potential, E^0 at 25 ºC is calculated for hydrogen fuel cell as:

$$E^0 = -\Delta G/nF = 1.23V \quad (2.6)$$

In a hydrogen-fed PEMFC, the equilibrium electrode potentials are as follows:

Anode: $H_2 \rightleftharpoons 2H^+ + 2e^-$ E^0= 0.00V vs RHE (2.7)

Cathode: $½O_2 + 2H^+ + 2e^- \rightleftharpoons H_2O$ E^0= +1.23V vs RHE (2.8)

The reaction at the anode is known as the hydrogen oxidation reaction (HOR) and the reaction at the cathode is the oxygen reduction reaction (ORR). Both reactions occur at the surface of the electrocatalyst, normally Pt, within the catalyst layers of the electrodes. The rate of HOR is typically about 10^3 times the rate of the ORR. This means that the platinum loading at the cathode needs to be around four times higher than at the anode, to achieve similar performance at both electrodes.

The slow kinetics of the ORR leads to a considerable negative overpotential at the PEMFC cathode [40]. Improvement of the mass-specific activity of the cathode electrocatalyst towards the ORR can lead to reduction in the amount of Pt required.

2.1 Impact of Catalyst Morphology on Electrocatalytic Activity

The size and shape [41-44] of the catalyst nanoparticles on the conductive support will affect the observed catalytic activity. Nanoparticles with a polyhedral shape can normally be described as having a mixture of (111) and (100) and (110) surfaces connected by edges and corners in which atoms have a low coordination number. Figure 2.1 shows a model nanoparticle with (111), (100) and (110) crystal faces. Among these three faces, (111) faces have the lowest surface energy while (110) faces have the highest [45, 46]. Nanoparticle shape determines which crystal faces are exposed at the surface of a nanoparticle. For example, a perfect cubic Pt

nanoparticle has six (100) surfaces. In a Pt octahedron all the exposed surfaces are (111), in a Pt cube-octahedron the exposed surfaces are a mixture of (111), (100) and (110) faces. These differences can give rise to different catalytic activity. The ORR rate on each crystal face is dependent on surface electronic properties and geometric factors. These also affect adsorption of anions such as OH^- and SO_4^{2-}. The catalytic activity of these surfaces, decreases in the order Pt (110) ≥ Pt (111) > Pt (100) [47, 48] in perchloric acid solution. The ORR rate is limited by O_{ads} and OH_{ads} adsorption on Pt [49] at high positive potentials; the less reactive high-coordinate Pt (111) surfaces are more conducive than the Pt (100) surfaces to the ORR [50-52] .

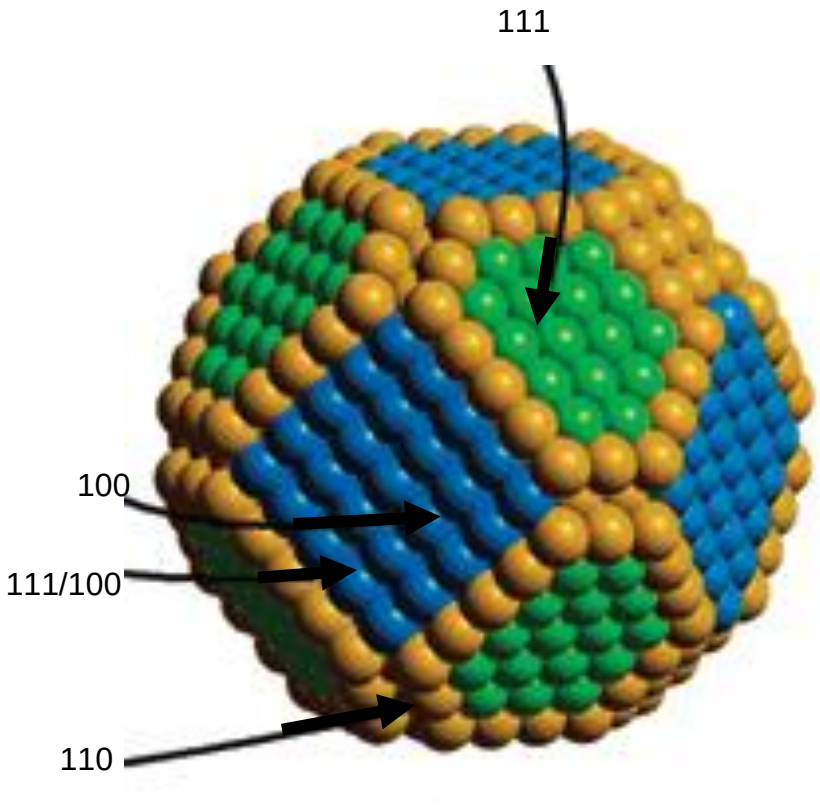

Figure 2-1 *Model Pt nanoparticle with truncated octahedral shape with dissolved edges and corners showing the Pt (111), (100) and steps [53]*

The mass activity is kinetic current per unit mass of the active electrocatalyst (Pt) within an electrode and is usually measured at 0.9 V. It is often used as a measure of catalyst effectiveness in terms of fuel cells. This activity should increase according to the surface area available for reaction and so smaller particles with higher surface/volume ratios would be expected to produce superior mass activity. However, this is not necessarily the case and there is much debate in the literature concerning particle size effects [47, 49, 54-59].

Pt surface area specific activity (the current density per unit electrochemically-active surface area of the electrode) has been found to reduce with decreasing particle size and the studies have shown that mass activity reaches a maximum at about 2.5 nm particle diameter [53, 60, 61]. The mechanisms of this decrease in specific activity are not fully understood and a few different explanations have been given, including a lower ratio of preferable crystal faces [47, 56],[62] stronger interaction between oxygen-containing species and Pt atoms [62-64] and lower potential of total zero charge (pzc) [62, 65, 66], as particle size decreases. According to Mayrhofer et al. [66], the potential of total zero charge shifts negative from 0.285 V for polycrystalline Pt to about 0.245 V for 1 nm Pt nanoparticles and this is caused by a decrease in the average coordination number of atoms with decrease in the particle size. This means that at a given potential the surface coverage by OH_{ads} and/or O_{ads} increases with decreasing the particle size. These OH_{ads} and/or O_{ads} species come directly from the ORR as reaction intermediates and from the aqueous electrolyte. These OH_{ads}/O_{ads} can block the active sites required for the adsorption of O_2 and/or the splitting of the O–O bond and so this increase in

adsorption of oxygenated species for smaller particles leads to a decrease in specific activity.

Other researchers have argued that the specific activity depends on the interparticle distance [67-69]. According to this theory, the full electrochemical surface area of the Pt is only available to O_2 molecules if Pt particles are well-separated from neighbouring particles on the carbon support. In contrast, Arenz et al. [70] recently found that maximum activity of PEMFC catalysts was achieved by decreasing Pt interparticle distance (while avoiding NP agglomeration).

In practice it is not possible to prepare clean, monodisperse Pt nanoparticles, all with the same shape and so separating the factors involved is a major challenge.

2.2 Impact of Catalyst Dispersion on Electrocatalytic Activity

The way in which catalyst particles are distributed across the carbon support can significantly affect catalyst utilisation, and therefore observed mass activity. One of the main degradation modes of PEMFC catalysts is the loss of active surface area by agglomeration of catalyst particles.

Nanoparticles have a tendency towards aggregation due to inter-particle attraction and thermodynamically-driven minimisation of the surface energy. Stabilizers, usually surfactants or polymers, are often used to prevent aggregation, they attach to particle surfaces and prevent aggregation. Stabilizers generally operate either by

steric or electrostatic repulsion, or in some cases a combination of the two. Surfactants and polymers are commonly used in nanoparticle synthesis to prevent particle aggregation. It is usually thought that these surfactants and polymers block electrochemically active sites on the catalyst surface and need to be removed before the catalyst can be used in a fuel cell. The act of surfactant/polymer removal, which usually involves heating or extensive washing with solvents, is likely to cause particle agglomeration. Once the stabilizer is removed the nanoparticles are more likely to aggregate during fuel cell use, thereby causing degradation. It therefore seems preferable not to remove the stabilizer. The objective of this work is to determine the effect of the surfactant on the catalytic activity. It is likely that different stabilizers will adsorb on the platinum surface in different ways and so will affect catalytic activity to different extents. In the field of homogeneous catalysis physical properties and catalytic activity of mononuclear transition metal complexes are systematically modified by the incorporation of organic ligands [71] in the metal coordination sphere. Higher reactivity, better selectivity, and decreased sensitivity to poisoning, compared to heterogeneous supported metal catalyst systems has been achieved in many cases.

2.3 Brief Theory of Colloid Stability

Colloids consist of small particles, < 1 μm, of one substance dispersed (not dissolved) in another. When solid particles are dispersed in water, they will move and collide under Brownian motion. In these systems the most stable thermodynamic state is one in which surface energy is minimised and all the

particles stick together into one solid mass (aggregation). Colloidal systems are only kinetically stable, an energy barrier must exist to prevent particles sticking together when they collide. This depends on the balance of the repulsive and attractive forces that exist between particles as they approach one another. If all the particles have a mutual repulsion then the dispersion remains stable. However, if the particles have little or no repulsive force then the particles may adhere to one another and form aggregates of successively increasing size. If the particles are more dense than the dispersion medium, they will settle out under the influence of gravity.

There are at least two general procedures for preventing colloidal particles from aggregating. The first method of imparting stability utilises electrostatic repulsion between charged particles. The second is known as steric stabilization and usually involves adsorption of nonionic macromolecules, which are soluble in the dispersion medium, onto the particle surfaces. Sometimes stabilization is caused by a combination of steric and electrostatic effects, for example, when polyelectrolytes are adsorbed onto particle surfaces.

Electrostatic Stabilization

Most colloidal particles have a surface charge. Some have surface groups such as -COOH, $-OSO_3H$ or $-NH_2$ which react with acids or bases to give surface charges. Some particles adsorb ions or surfactants from solution onto their surfaces. DLVO theory [72, 73] describes the stabilization of colloids by electrostatic forces and suggests that the stability of a particle in solution is dependent upon its total

potential energy function V_T. This theory recognizes that V_T is the balance of several competing contributions:

$$V_T = V_A + V_R + V_S \quad (2.9)$$

The attractive potential, V_A, is caused by the van der Waals forces and is given by:

$$V_A = -A/(12 \pi D^2) \quad (2.10)$$

Where A is the Hamaker constant and D is the particle separation.

The repulsive potential V_R is a far more complex function.

$$V_R = 2 \pi \varepsilon a \xi^2 exp(- \kappa D) \quad (2.11)$$

Where a is the particle radius, π is the solvent permeability, κ is a function of the ionic composition and ξ is the zeta potential. The zeta potential is the potential difference between the dispersion medium and the stationary layer of fluid attached to the dispersed particle. Zeta potential can be calculated from the particle's electrophoretic mobility, which can be measured experimentally.

V_S is the potential energy due to the solvent, it usually only makes a marginal contribution to the total potential energy over the last few nanometres of separation.

DLVO theory suggests that as particles approach each other due to the Brownian motion, the stability of the colloidal system is determined by the sum of the van der Waals attractive and electrical double layer repulsive forces that exist between the particles. The theory proposes that an energy barrier, resulting from the repulsive

force, prevents two particles approaching one another and adhering together as shown in Figure 2.2.

In stable colloids the primary maximum energy barrier prevents particles from approaching close enough to cause aggregation. If the particles collide with enough energy to overcome that barrier, the van der Waals attractive force will pull them into contact where they adhere strongly together. Therefore for colloidal system to be stable, the particles need sufficiently high repulsion to resist aggregation. If a repulsion mechanism does not exist, aggregation will result. Addition of electrolyte to the medium screens the charge in the electrical double layer, lowering the repulsive energy barrier, eventually causing aggregation. For this reason sterically stabilized colloids, described in the following section, are usually more stable in electrolyte solutions. In certain situations there may be a “secondary minimum” where a much weaker and potentially reversible adhesion between particles occurs. This is known as flocculation and the weak flocs are stable enough not to be broken up by Brownian motion, but may dissociate under vigorous agitation.

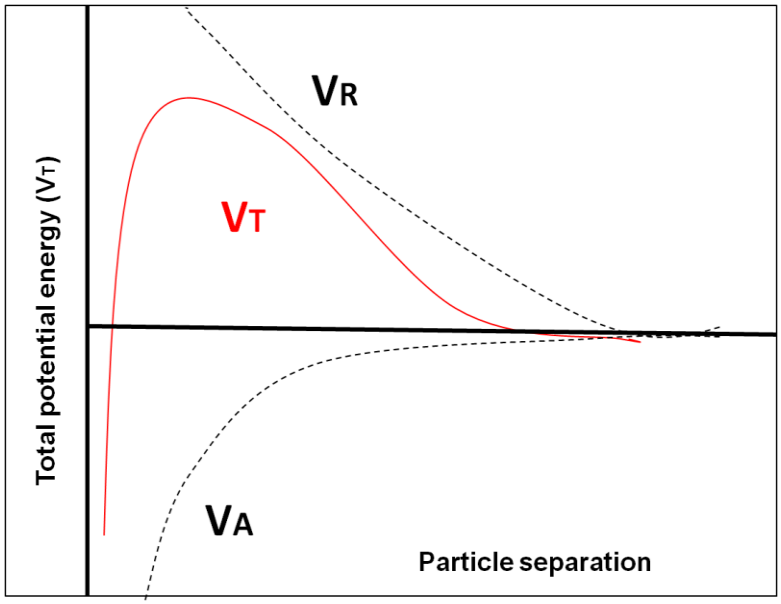

Figure 2-2 *Schematic diagram of the variation of potential energy with particle separation according to DLVO theory. The net energy is given by the sum of the double layer repulsion (V_R) and the van der Waals attractive (V_A) forces that the particles experience as they approach one another.*

Aggregation and agglomeration are terms that are used interchangeably in the field of nanotechnology. In the field of powder technology, the term aggregation refers to particles connected by their surfaces and the term agglomeration refers to particles connected by their corners [74]. The term flocculation is used when the attraction between particles is weak and reversible, perhaps in a secondary minimum of the DLVO curve.

Steric Stabilization

Steric stabilisation involves polymers added to the system which adsorb onto the particle surface and prevent the particle surfaces coming into close contact, as shown in Figure 2.3. If enough polymer adsorbs, the thickness of the coating keeps particles separated by steric repulsions between the polymer layers, and at these

separations the Van der Waals forces are too weak to cause the particles to aggregate. The term *"steric"* denotes a thermodynamic repulsion [75-80]. For two colloidal particles, each surrounded by polymer chains, inter-penetration of the dissolved polymer chains must occur to permit aggregation to proceed. If the dispersion medium is a good solvent for the polymer concerned, mixing of the polymer chains causes a rise in osmotic pressure, also known as osmotic repulsion. Close approach of the particles also results in an unfavourable reduction in configurational entropy of the polymer chains. Steric stabilisation results if the positive free energy of inter-penetration outweighs the Van der Waals attraction between the core particles.

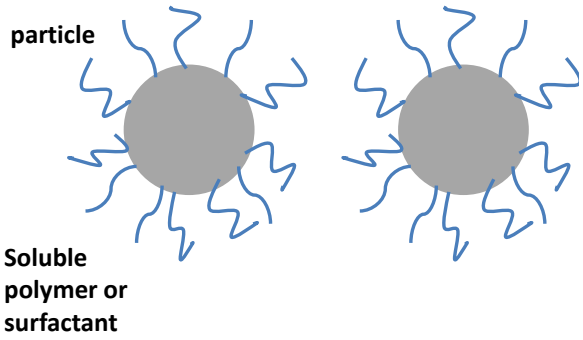

Figure 2-3 *Schematic diagram depicting steric stabilization.*

Steric stabilization can also result from the adsorption of nonionic surfactants. The adsorption can be caused by the 'hydrophobic' interaction [81]. The interaction between water molecules is much stronger than the interaction between water molecules and organic groups like CH_{3-} or CH_{2-}. Therefore the hydrophobic parts of the surfactant molecules are rejected from the water phase and adsorb on the nanoparticle surfaces. The hydrophilic parts of the molecules are extended into the aqueous solution and provide the steric stabilization.

2.4 Organic Materials Adsorbed onto Platinum Electrocatalysts

It is known in the field of colloid science that adsorbed surfactants and polymers can impart colloid stability and prevent aggregation as described above. However, in the field of electocatalysis these materials are thought to block catalytic sites and reduce activity. This section contains a literature review of the effect of adsorbed organic materials on the catalytic activity and colloid stability of platinum nanoparticles. In the literature these materials are usually termed: polymers, surfactants or ligands. Polymers and surfactants are often used to give colloid stability and are generally considered to block catalytic sites and be detrimental to catalytic activity. Ligands on the other hand are often considered to improve catalytic activity.

2.4.1 Polymers

The water-soluble polymer poly(vinylpyrrolidone (PVP) is commonly used as a steric stabilizer for platinum nanoparticles. The polymer chains are thought to attach to the surface of metal particles via carbonyl groups [82], as shown in Figure 2.4. Redox treatment of PVP/Pt samples was found to induce degradation of PVP, catalysed by the metal nanoparticles. The pyrrolidone rings released from the aliphatic polymer backbone can then strongly adsorb on the metal surface, blocking catalytic sites, as shown in Figure 2.5. It is thought that for thorough evaluation of catalytic activity it is necessary to remove the PVP from the surface of the particles

[83]. From this example it appears that the problem is caused by degradation of the polymer.

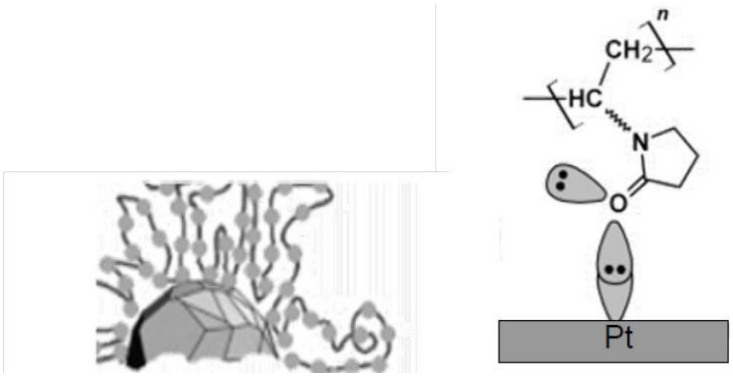

Figure 2-4 *Schematic showing the proposed stabilization mechanism for PVP [82]*

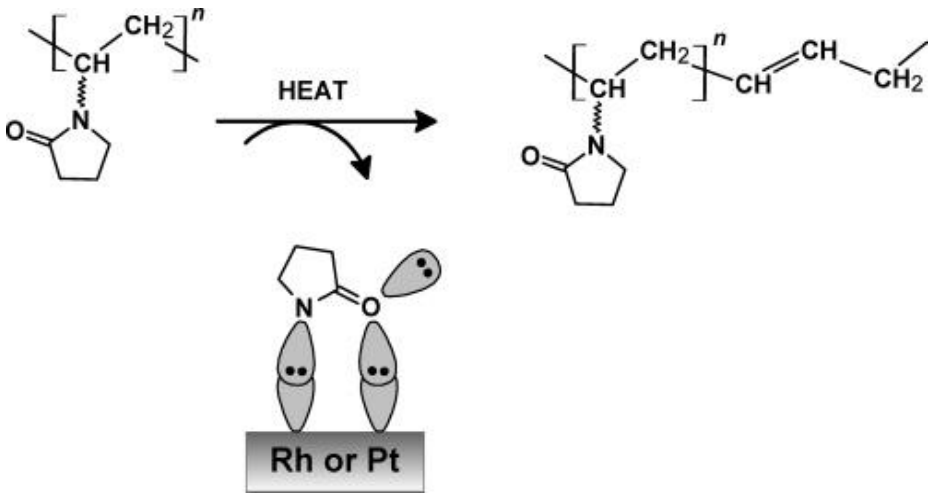

Figure 2-5 *Schematic showing the proposed degradation mechanism for PVP [82]*

Lee et al. [84] have reported the effect of stabiliser type on catalytic performance of platinum nanoparticles towards a range of reactions. Pt cubes with the same shape were synthesized using PVP or tetradecyltrimethylammonium bromide (TTAB) as stabilizer. They particularly noted that PVP, which has a strong interaction with platinum, has a greater inhibiting effect, for most reactions studied, than TTAB

which interacts weakly with Pt. They conclude that since TTAB interacts only weakly with Pt, the TTAB stabilised particles will have groups of Pt atoms which are not covered by TTAB and that these are essential for catalytic reactions to occur.

Other polymers such as polyacrylates [85] poly(vinyl)formamide derivatives [86], aminodextran [87], and polydiallyldimethylammonium chloride [88] and polyacrylamides [89] have also been used in the preparation of platinum nanoparticles. All these polymers will interact with the platinum surface in different ways.

2.4.2 Surfactants

Surfactants, also called surface active agents, are molecules in which a non polar tail is attached to a polar head. Their name derives from their ability to modify the properties of surfaces. In water, they self-associate at concentrations above the critical micellar concentration (cmc) to form micelles. Micelles have interfacial regions containing ionic or polar head groups. It is well known that surfactants can inhibit corrosion by blocking the surface of metal. Surfactant adsorption at the solid /liquid interface may be due to electrostatic interaction, van der Waals interactions or hydrogen bonding.

Many studies have been carried out on the adsorption of surfactants on gold surfaces [90]; Gutig et al. [91] found that nonionic polyethylene glycol

monododecyl ether ($C_{12}EO_6$) forms a monolayer like structure, while cetyltrimethylammonium bromide (CTAB) forms a bi-layer structure on gold

Standard anionic surfactants, such as sodium dodecyl sulphate (SDS) [92], and cationic, such as tetradecyltrimethylammonium bromide, (TTAB) [93], have been used to give electrostatic stability to platinum nanoparticles. There is concern that the presence of surfactants may reduce platinum catalytic activity by blocking active sites [94, 95]. However Wang et al. [96] found that the presence of surfactants did not affect electrochemical activity. They suggest that small molecules like H_2 and O_2 can diffuse through the surfactant layer.

As described earlier surfactant adsorption is driven by the tendency of the alkyl chains to be expelled from the water. A review by Lipkowski et al. [97] suggests that surfactants can adsorb at metal surfaces in many ways which are dependent on molecular structure as well as electrical potential. The structure of the adsorbed layer will affect the degree to which catalytic active sites are blocked.

Jaschke [98] used AFM to investigate the adsorption of surfactants onto gold surfaces their findings are summarised in Figure 3.6. For sodium dodecyl sulphate (SDS) and hexadecyltrimethylammonium hydroxide (CTAOH), alkane chains adsorb horizontally along the gold symmetry axes, leading to half-cylindrical stripes (A) Surfactant adsorption is driven by tail group substrate dispersion forces. The gold lattice controls aggregate orientation.

A

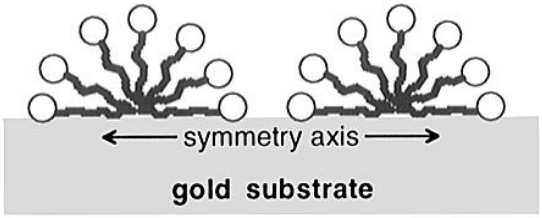

B

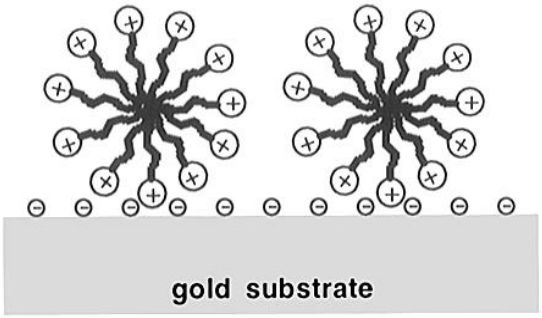

Figure 2-6 *Schematic showing the proposed mechanism of adsorption [98] of SDS and CTAOH (A) and TTAB(B) on gold surfaces*

For TTAB, bromide counterions adsorb preferentially to the gold surface, creating a negatively charged layer. Surfactant adsorption is driven by headgroup surface electrostatic forces, leading to full cylindrical aggregates (B). The surface interacts with only a small portion of the cylindrical aggregate, leading to weak surface control and flexible stripes.

Surfactant adsorption on nanoparticle surfaces will be limited by the surface area of the crystal faces. It is likely that in the case of TTAB, bromide counterions will adsorb preferentially to the Pt surface, creating a negatively charged layer and surfactant adsorption will be driven by headgroup surface electrostatic forces. The TTAB molecules are likely to adsorb in bi-layers with the ionic head groups interacting with the metal surface. Nonionic surfactants may absorb in monolayers with the alkyl chains interacting with the metal surface.

B

2.4.3 Adsorption of Organic Ligands

Recently, it has been reported that the electrocatalytic activity can be promoted by adsorbed organic species. Pietron et al. [71] have shown that platinum nanoparticles functionalized with the organophosphine ligand triphenylphosphinetriphosphonate, TPPTP, are active electrocatalysts for hydrogen oxidation and oxygen reduction. Since triarylphosphine-based ligands coordinate Pt particles through an electron-rich phosphorous, the authors suggest a weakening of Pt–O bonds on Pt-TPPTP causing a relative improvement in ORR electrocatalytic activity compared to bare Pt nanoparticles.

Chung et al. [99] showed that oleylamine, adsorbed on platinum nanoparticles, caused significant enhancement of the electrochemical activity for the oxygen reduction reaction. They suggest that organic molecules capping electrocatalysts can improve reactivity by both electronic and structural modification. Zhou et al.[100] prepared Pt nanoparticles capped with para-substituted (R = $-CH_3$, $-F$, $-Cl$, $-OCF_3$, and$-CF_3$) phenyl groups. They found that ORR activity increased with electronegativity of the capping group. They suggested that the more electronegative ligands weaken the Pt-O bond. In another study Cavaliere et al. [101, 102] showed that organic crown ligands on Pt nanoparticles do not block electrochemical activity.

Chapter 3 Preparation of Nanoparticles

This chapter describes the preparation and initial characterisation of metallic nanoparticles. In this work most nanoparticle preparations were carried out, using a colloidal route in aqueous solution, due to environmental, safety and cost considerations. A wide range of Pt nanoparticles were prepared in this work and some of these were chosen for scale up and electrochemical testing, which is described in chapter 5. A few bimetallic Au/Pt nanoparticles were also prepared. The preparation procedures used and results are described later in this chapter.

The preparation of gold nanoparticles in aqueous solution, using citrate reduction of Au^{3+} has been well documented over many years [103-105]. In this method citrate acts both as the reducing agent and the stabilizing agent for the formation of gold nanoparticles. The citrate route to produce monodisperse gold nanoparticles was developed by Turkevich et al. [103] in 1951. The method was refined by Frens [105] and can produce gold nanoparticles of controlled and uniform size and shape from 10-100 nm. Initial work in this thesis was carried out on the preparation of gold nanoparticles, in order to test the preparation and characterisation techniques available.

There is also considerable work in the literature on the colloidal preparation of platinum nanoparticles. Extensive reviews have been published [45, 46, 55, 106]. Platinum nanoparticles tend to have less well controlled size and shape. The

general reaction scheme involves the chemical reduction in aqueous solution of a precursor containing platinum in its +2 or +4 oxidation state.

$PtCl_6^{2-}{}_{(aq)} + 2e^- \rightleftharpoons PtCl_4^{2-}{}_{(aq)} + 2Cl^-$ $E^0 = +0.726$ V *vs* RHE (3.1)

$PtCl_4^{2-}{}_{(aq)} + 2e^- \rightleftharpoons Pt_{(S)} + 4Cl^-{}_{(aq)}$ $E^0 = +0.758$ V *vs* RHE (3.2)

The aim is to produce a stable colloid consisting of well dispersed particles with a narrow size distribution.

Sodium borohydride was chosen as the initial reducing agent. Previously documented [107-109] procedures were followed initially which used readily available, inexpensive reagents. The method of Lee et al. [93] was chosen, because these workers were able to prepare fairly monodisperse particles, of controlled shape. The authors had used the cationic surfactant, tetradecyltrimethylammonium bromide (TTAB).

3.1 Theory of Precipitation Reactions

The preparation of nanoparticles, described in this thesis, involves the reduction of water soluble metal cations to the insoluble metal. If the rate of this reaction is significant, the solution will quickly become supersaturated and precipitation of solid metal occurs. Formation of a stable nanoparticle dispersion requires some mechanism preventing particle aggregation, as described in section 2.3.

It is generally accepted that the preparation of nanoparticles in a solution system consists of a nucleation stage followed by growth and Ostwald ripening on the

existing seeds [46]. In the rapid nucleation stage, kinetic deposition of atom clusters is driven by their super saturation in solution. In the Ostwald ripening and growth stages the nanoparticle shape may be controlled by the difference of the surface energy on each crystallographic face. The energetically most stable crystallographic faces have lowest growth rate. Adsorption of surfactants and ligands onto specific crystallographic faces can increase the stability of these faces, thus affecting particle shape. The following factors are important for the synthesis of a colloidal dispersion of monodisperse nanoparticles [110, 111]:

- The processes of nucleation and growth must be separated in time, so that all nuclei form at the same time. There should be no new nucleation after growth has begun.
- The nucleation process should be relatively fast and growth & ripening relatively slow.

Following the nucleation and growth stages, there is a tendency towards agglomeration due to inter-particle attraction and minimisation of surface interfacial energy. The agglomeration process can be inhibited by introduction of a stabilizer, which attaches to particle surfaces and prevents aggregation (as discussed in Chapter 2).

3.2 Materials

The use of clean glassware is extremely important in the preparation of nanoparticles. Any impurities have an effect on the nucleation and growth of nanoparticles. All glassware was cleaned before use, with aqua regia, and rinsed

thoroughly using Milli-Q ultra pure water. All solutions were prepared using Milli-Q ultra pure water with resistivity ≥18.2 MΩ cm.

The following commercially available chemicals and solvents were purchased from Sigma-Aldrich and used as received:

$HAuCl_4.3H_2O$ (99.99 %)

K_2PtCl_6 (99.99 %)

$H_2PtCl_6.6H_2O$ (99.995 %)

$NaBH_4$ (>99 %)

sodium citrate (>99.5 %)

L-ascorbic acid (>99 %)

tetradecyltrimethylammonium bromide (99 %) (TTAB)

cetyltrimethylammonium bromide (99 %) (CTAB)

nonylphenol ethoxylate (NP9)

decaethylene glycol oleyl ether (BriJ O10)

sodium dodecyl sulphate (SDS) (>99 % Sigma-Aldrich)

pentadecafluorooctanoic acid (PFA)

polyvinylpyrolydone (mw 40,000) (PVP)

ethylene glycol (99.95 %)

3.3 Synthesis of Gold Nanoparticles

Procedure

Citrate-stabilized gold nanoparticles were synthesised via the Frens method [105]. An aqueous solution of $HAuCl_4.3H_2O$ (9.9 mg, 100 mL) was heated under reflux for 5-10 minutes. The mixture was stirred at around 600 rpm using a magnetic stirrer bead. An aqueous solution of sodium citrate (22.8 mg, 2 mL) was added. Heating under reflux was continued for a further 10 minutes to ensure complete reduction of the gold salt. The red colloidal solution was centrifuged three times for 10 minutes each time at 3500 rpm and the supernatant collected.

3.4 Synthesis of Platinum Nanoparticles

Procedure

The method of Lee et al. [93] was followed and adapted for the preparation of Pt nanoparticles. The exact quantities of reagents used are given in Tables 4.2-4.4. In a typical synthesis, aqueous solutions of K_2PtCl_4 and surfactant were mixed in a 20 mL round-bottomed flask at room temperature. The flask was immersed in a water bath maintained at 50 ºC. After about 5 minutes when the solution became clear, ice-cold $NaBH_4$ was added. The vial was capped with a rubber septum immediately and the H_2 gas pressure inside the vial was released through a needle in the septum for 10 minutes. The needle was then removed and the solution was kept at 50 ºC for 6 hrs. The mixture was stirred at around 600 rpm using a magnetic stirrer bead.

In this work the procedure was repeated using a range of anionic, cationic, non-ionic and polymeric surfactants/dispersants. In some cases the procedure was not successful and mass aggregation occurred, or the platinum was not reduced [105].

The reagent quantities, reaction times and temperatures are given in Tables (4.2-4.4). The use of nonionic surfactants along with $NaBH_4$, as reducing agent, resulted in Pt aggregation. The procedure was adapted to prepare stable Pt+NP9 nanoparticles. The use of ascorbic acid as the reducing agent resulted in the successful preparation of nanoparticles using nonionic surfactants. In some cases the nonionic surfactants themselves acted as reducing agents. In this case an aqueous solution of NP9 was heated at 50 ºC and a solution of K_2PtCl_6 was added. The mixture was stirred at 50 ºC for 4 hours.

3.4.1 Purification of Colloidal Platinum

A repeated centrifugation/redispersion procedure was used to remove excess surfactant and soluble inorganic species. The dispersions were centrifuged for 20 minutes at 20,000 rpm (33,987x*g*) and 4 ºC in a Sigma 3K30 refridgerated centrifuge. The supernatant was discarded, and the precipitate redispersed in Milli-Q water. The process was repeated once.

The Pt+NP9 particles are smaller than the Pt+TTAB particles. They were centrifuged as described above but at 26,000 rpm for 1.5 hrs.

3.5 Preparation of Gold/Platinum nanoparticles

One possible strategy to improve the catalytic activity of platinum based catalysts is the use of core-shell nanoparticles [112-114], where the shell is platinum and the core is a less expensive metal. In this work two different procedures were chosen from the literature to prepare gold/platinum particles [115, 116].

3.5.1 Polyol Procedure

The procedure of Garcia-Gutierrez et al. [115] was followed. Nanoparticles were synthesized according to the following procedure. Polyvinylpyrrolidone (MW 40,000, Sigma Aldrich) (PVP) (0.8 g) was dissolved in 100 mL of ethylene glycol 99.95 %, Fischer Chemicals)(EG)and stirred. After complete dissolution of PVP in ethylene glycol, 4 mL of an aqueous solution of $H_2PtCl_6.6H_2O$ (0.05 M) was added to the EG/PVP solution. The mixture was then heated to 140 ºC and refluxed under air. On reaching 140 ºC the colour of the solution changed from a yellowish to a dark brown (suggesting the reduction of Pt), 2 mL of an aqueous solution of $HAuCl_4.3H_2O$ (0.1 M) was added to the system. The mixture was stirred at 140 ºC for 3 hours. It was then removed from the heat and stirring ceased.

3.5.2 Aqueous Procedure

In this case Au (core)–Pt(shell) (Au/Pt) nanoparticles were synthesized via sequential precipitation of Au and Pt salts, according to the procedure of Schmid [117], adapted by Braidy et al. [116]. An aqueous suspension of citrate stabilised Au

nanoparticles was prepared by the Frens method [105], described in section 4.3. The Au nanoparticles were coated with Pt using the following procedure. Briefly, 9.6 mL of the Au nanoparticle suspension was mixed with 10 mL of $HAuCl_4.3H_2O$ (5.3×10^{-4} wt.%) and 1.5 mL of ascorbic acid (1.76 wt.%) in an ice bath. The dispersion was stirred for 90 minutes. This procedure was repeated with varying ratios of Au:Pt.

3.5 Physical Characterisation of Nanoparticles

The nanoparticles were characterised using transmission electron microscopy (TEM), Nanosight [118] and dynamic light scattering [119-124].

3.5.1 Transmission Electron Microscopy (TEM)

TEM Specimen preparation

A drop of the purified nanoparticle dispersion was placed onto a formvar-coated carbon-on-copper TEM specimen grid (300 mesh, Agar Scientific). The specimen was dried for 12 hours in a desiccator and then stored in a sealed container.

Bright-field imaging was performed using a JEOL 1200ex LaB_6 TEM at an accelerating voltage of 80 kV. The particle size distributions were calculated using using ImageJ software [125]. The diameter of over 200 individual particles was measured.

High-resolution images were recorded using a FEI Tecnai F20 Field-Emission HRTEM operating at 200 kV.

3.5.2 Nanosight Particle Tracking Analysis

Nanoparticle tracking analysis was carried out on a NanoSight LM10 with a 405 nm (blue) laser. Nanoparticle Tracking Analysis (NTA) is a new method for the direct analysis of nanoparticles in liquids [3]. The technique requires a small (250 µL) sample of liquid containing dispersed particles, at a concentration of approximately 10^8 /mL, to be introduced into a scattering cell through which a focused laser beam is passed. Particles within the path of the laser beam are observed via a microscope-based system. The Brownian motion of nanoparticles is analysed using a video camera, each particle is separately tracked by a dedicated particle tracking image analysis program. The particle size distribution obtained by NTA is a direct number/frequency distribution [3]. The particle size distribution measured by NTA does not suffer from the limitation of being an intensity weighted distribution, which is obtained using dynamic light scattering (DLS). The ability of NTA to simultaneously measure particle size and particle scattering intensity allows polydisperse mixtures to be resolved.

The 3-dimensional Brownian movement is tracked in 2 dimensions. The average distance each particle moves in *x* and *y* in the image is automatically calculated. From this value, the particle diffusion coefficient, *Dt*, can be obtained and, at temperature *T*, and solvent viscosity *η*, the particle hydrodynamic diameter d

calculated. The following variation of the Stokes-Einstein equation, where k_B is Boltzmann's constant is employed.

$$\frac{(x,y)^2}{4} = Dt = \frac{Tk_B}{3\pi\eta d} \quad (3.3)$$

The technique is limited to particles of 10-20 nm, and above and to concentration ranges between 10^7 – 10^9 particles per mL. The technique complements DLS for the sizing of nanoparticles and data obtained from these methods can be validated by direct TEM observations of the sample [3, 118, 126].

3.5.3 Dynamic Light Scattering (DLS)

DLS is a light-scattering technique [119, 120, 123, 124] in which the intensity of laser light scattered by particles undergoing Brownian motion is used to determine their size distribution by the Stokes-Einstein equation:

$$D = \frac{Tk_B}{3\pi\eta d} \quad (3.4)$$

where *D* is the diffusion constant, η is the viscosity of the dispersant and *d* is the particle hydrodynamic diameter. The equipment uses a correlator to determine the autocorrelation function of the recorded intensity of scattered light. The diffusion constant, *D* can then be calculated. The technique requires knowledge of the viscosity and refractive index of the dispersant.

A Beckman Delsa Nano Particle analyser was used to analyse nanopaticles by DLS in this work. Dispersions were diluted to give suitable scattering intensities using Milli-Q water water. CONTIN software was used to analyse particle size distributions.

The diameter reported is that of a sphere with equivalent hydrodynamic radius to that determined by the Stokes-Einstein equation. It may not represent the true dimensions of a faceted particle, or one that is highly anisotropic. The technique involves far less preparation than the TEM technique and is useful for quickly comparing size distributions.

DLS directly measures intensity (weighted) size distributions, displayed as intensity histograms in the DelsaNano. In these histograms, the magnitude of each peak is proportional to the amount of the total scattered intensity due to particles. The DelsaNano measures intensity distributions and optionally converts them to volume or number distributions. A major limitation of the technique is that it is inherently sensitive to the presence of larger particles in a sample. A major limitation of DLS is that it is inherently sensitive to the presence of larger particles in a sample. This is because using the Rayleigh approximation, the intensity, of scattered light is proportional to the sixth power of the particle radius. The scattered intensity of any larger particles or aggregates contributes heavily to the DLS measurement whereas the scattered intensity from the smaller particles is lost in the background signal. This means that even a few large particles or aggregates in a sample will dominate the signal, resulting in an over-estimate in the mean diameter [127].

Table 3-1 *Comparison of particle measurement techniques*

Technique	Strengths	Weaknesses
NTA	Low cost small sample volume accurate particle size distribution	Sample needs diluting instrument is not easy to use cannot measure particles <10nm hydrodynamic radius measured particles assumed to be spherical
DLS	Low cost fast throughput, easy to use can measure particles > 1nm.	Sample needs diluting complex data evaluation size distribution not accurate for a polydisperse sample. tends to give over estimate of particle size for a polydisperse sample hydrodynamic diameter is measured particles assumed to be spherical
TEM	Visualisation of particle shape and degree of aggregation, for particle diameters >10 nm	High cost time consuming this technique analyses the smallest number of particles dispersion needs to be dried on a TEM grid degree of aggregation will be affected by drying and the electron beam
HRTEM	Visualisation of particle shape and degree of aggregation, for particle diameters down to 1nm	Disadvantages as for TEM The HRTEM requires highly skilled operation.

3.6 Results and Discussion

3.6.1 Gold nanoparticles

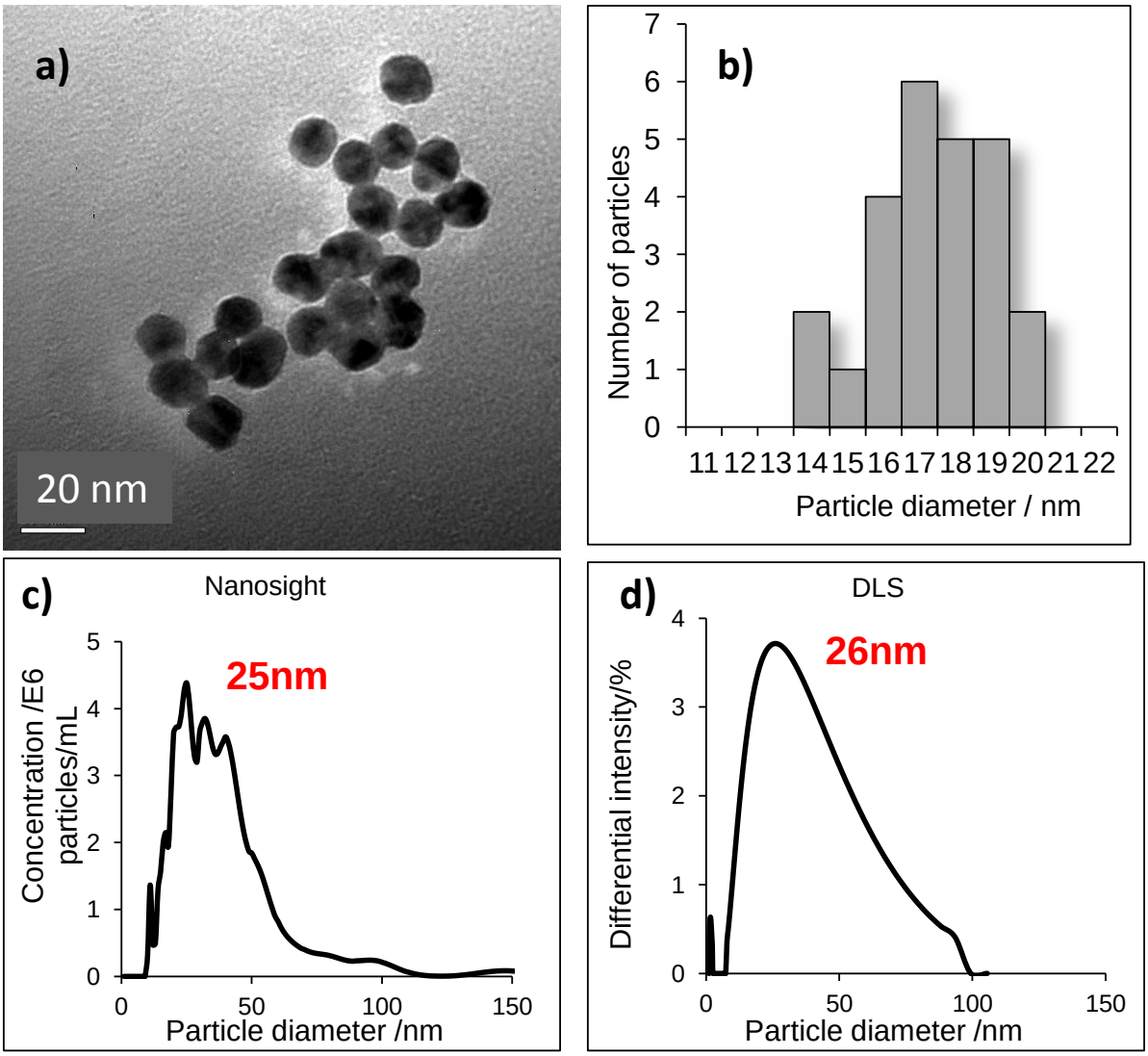

Figure 3-1 *Gold nanoparticles (JN1) a) TEM, b) paticle size distribution from TEM, c) particle size distribution from Nanosight, d) particle size distribution from DLS*

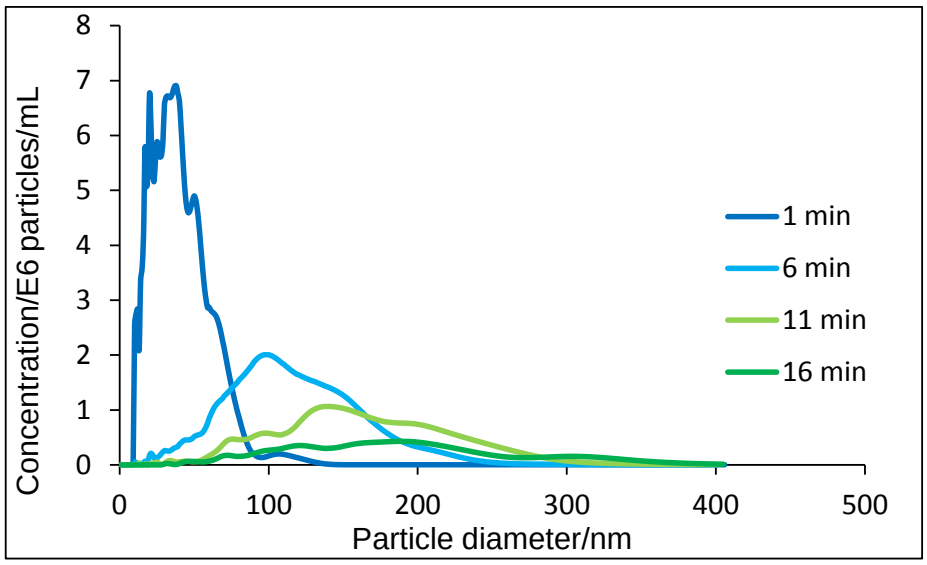

Figure 3-2 Nanosight results showing increase in particle size for gold sol JN12 with time.

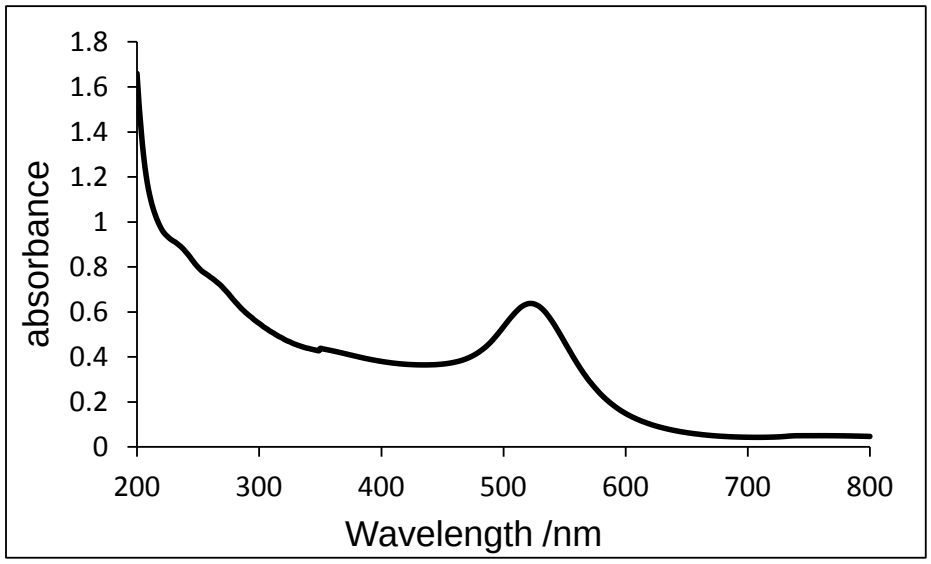

Figure 3-3 *UV Visible absorption spectrum for the Au sol JN1*

Three gold sols were prepared using the same procedure (JN1, JN10, JN12). The TEM, DLS and Nanosight results for JN1 are given in Figure 3.1. The mean particle size from TEM was 17.8 nm with a standard deviation of 1.6 nm. No individual particles bigger than 21 nm were observed. The DLS and Nanosight size

distributions agree well with each other with peaks around 25 nm. These techniques measure hydrodynamic diameter which is expected to be slightly larger than the diameter measured from TEM. Both Nanosight and DLS distributions show some particles larger than 60 nm. These are not observed by TEM. A major limitation of DLS is that it is inherently sensitive to the presence of larger particles in a sample. This means that even a few large particles or aggregates in a sample will dominate the signal, resulting in an over-estimate in the mean diameter [127]. The Delsa Nano software will convert intensity distributions to number distributions. These results are inaccurate and give much lower particle sizes than TEM. For example when the software was used to convert the intensity distribution for JN1 to a number average distribution, the result showed a single peak at 1 nm. Direct observation by TEM shows that this is obviously inaccurate.

Nanosight results were not always reproducible. Figure 3.2 shows how particle size increases with time as the sample is left in the cell. This suggests that, if the particles are left in the cell for more than 1 minute aggregation occurs. The gold sol needs to be diluted more than 100 fold with Milli-Q water for nanosight measurements, which may cause desorption of citrate ions from the particle surface and reduce the charge stabilization, causing aggregation. It is also possible that the smaller particles are sticking to the sides of the cell.

In conclusion the average particle sizes measured by DLS and Nanosight agree well with that from TEM. This suggests that the particles are well dispersed. All the gold sols had the expected red colour and appeared stable to the eye. The UV

absorption spectrum for the Au sol JN1 is shown in Figure 3.3 and shows an absorption maximum at 522 nm. This agrees well with previous work [128, 129] and again suggests well dispersed particles of 15-20 nm. 'It is well known that the optical spectrum of colloidal gold is dominated by a strong absorption in the visible region called the surface plasmon resonance band, which is due to the collective dipole oscillations of the free electrons in the conduction band of the gold' [130]. Factors such as particle size, shape and degree of aggregation affect the position, intensity and shape of the plasmon resonance band. [131].

3.6.2 Platinum nanoparticles

Pt +CTAB/TTAB

Table 3-2 *Pt+CTAB/TTAB nanoparticle formulations*

	JN4	JN5	JN8	JN42 (Pt+TTAB)
$K_2Pt\ Cl_4$	0.0063 g	0.0063 g	0.0063 g	0.03125 g
$NaBH_4$	0.0113 g	0.0113 g	0.0113 g	0.0565 g
UHQ water	9.385 g	9.385 g	9.385 g	50 g
TTAB	-	-	0.597 g	2.525 g
C TAB	0.597 g	0.597 g		
Reaction temperature	50 ºC	50 ºC	50 ºC	50 ºC
Reaction time	6 hrs	6 hrs	6 hrs	6 hrs
Observations	Stable black/brown dispersion	Stable black/brown Dispersion	Stable black/brown dispersion	Stable black/brown dispersion

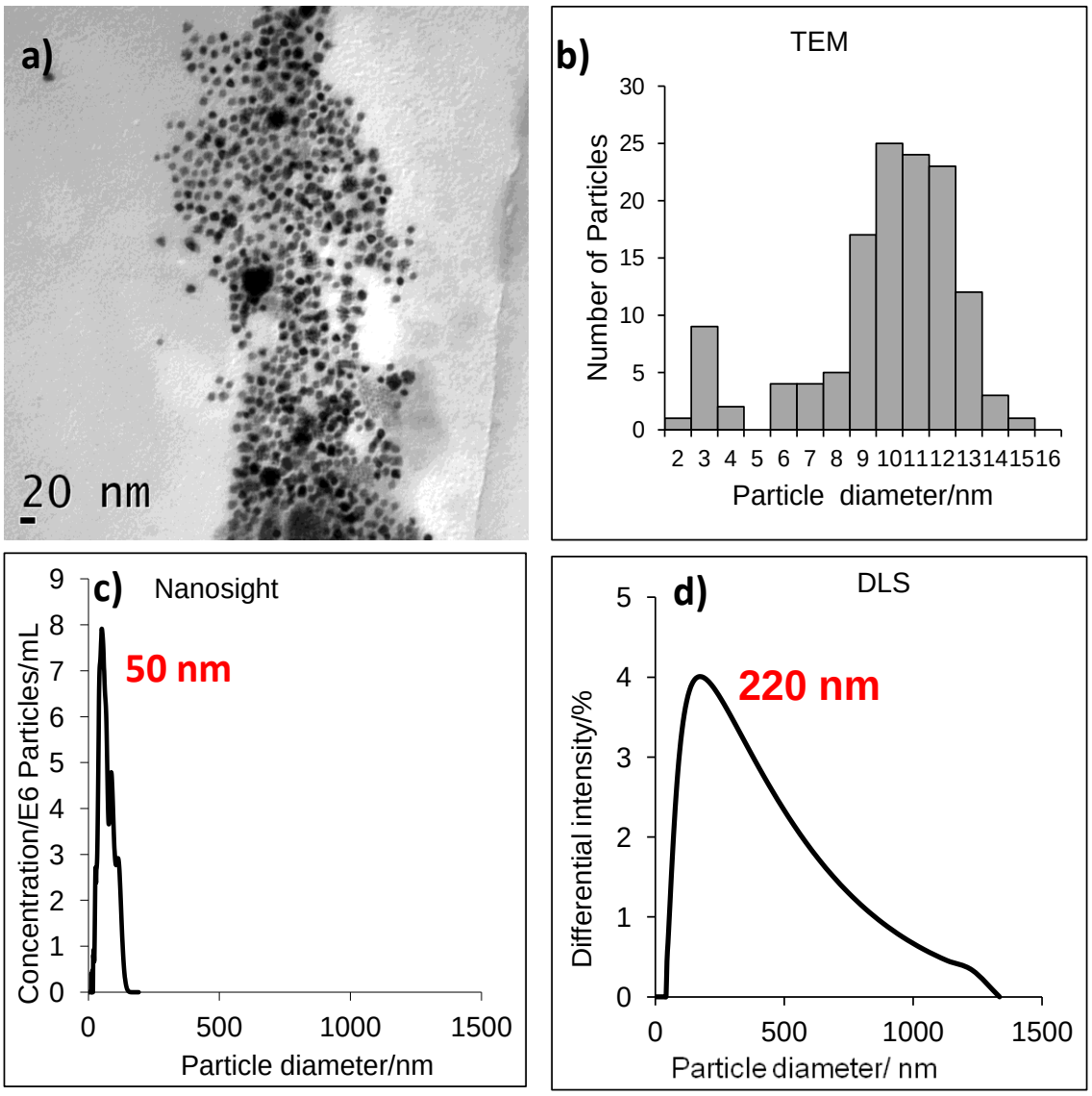

Figure 3-4 *Pt+CTAB nanoparticles (JN4) (a) TEM, (b) size distribution from TEM, (c) size distribution from Nanosight, (d) size distribution from DLS.*

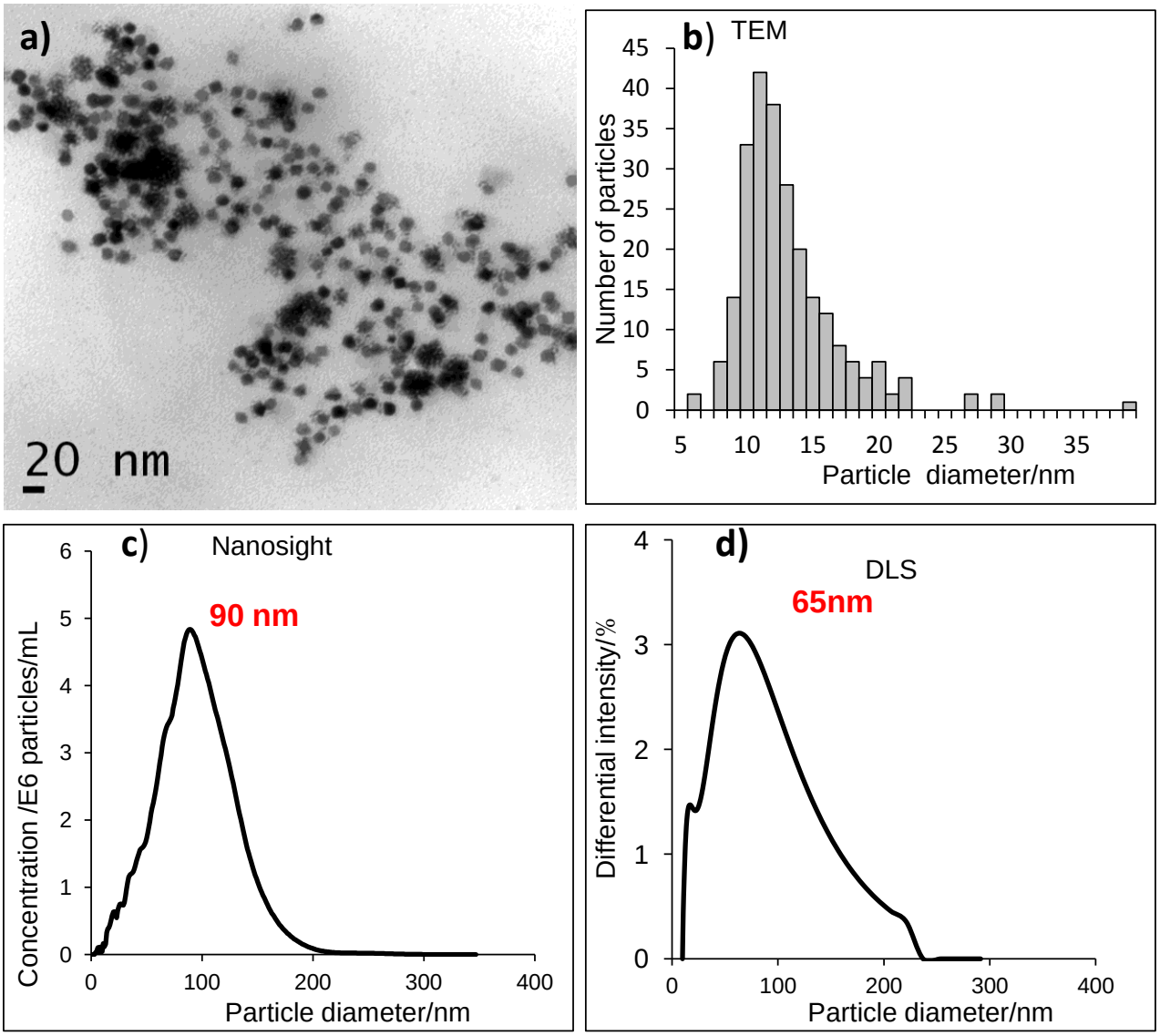

Figure 3-5 *Pt+TTAB nanoparticles (JN8) (a) TEM, (b) size distribution from TEM, (c) size distribution from Nanosight, (d) size distribution from DLS*

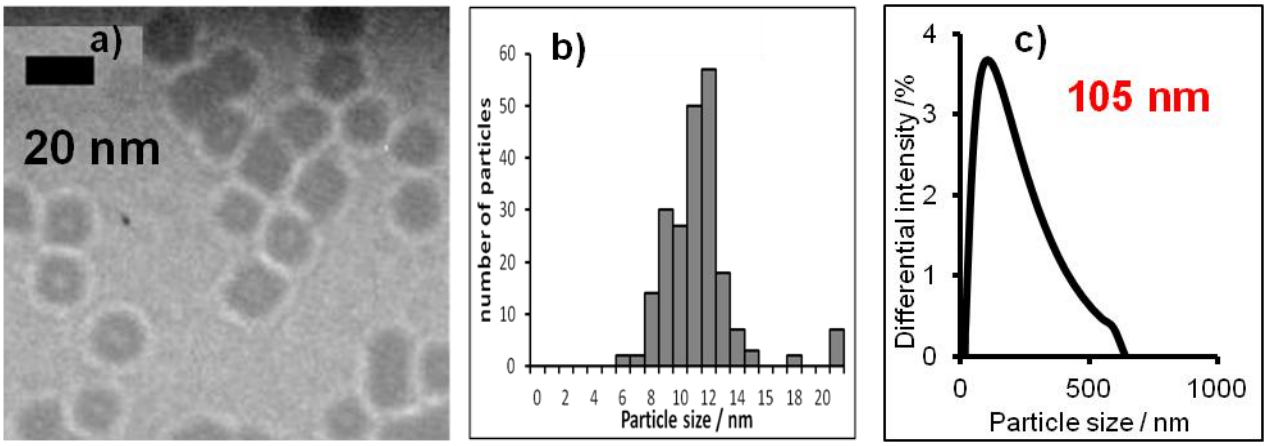

Figure 3-6 *Pt+TTAB nanoparticles, scale up (JN42) (a) TEM, (b) size distribution from TEM, (c) size distribution from DLS*

The exact formulations for each CTAB/TTAB nanoparticle dispersion are given in Table 3.2. Both cationic surfactants, CTAB and TTAB, gave stable nanoparticle dispersions. They all appear dark brown/black. Results for these are shown in Figures 3.4 and 3.5. The dispersions appeared stable to eye, showing no visible sedimentation or aggregation on storage over several weeks. In all cases the TEM results show individual particle sizes much smaller than DLS and Nanosight. The reasons are the same as those discussed in section 3.6.1. A very small proportion of larger particles or agglomerates can dominate a DLS experiment. The difference in average particle size between TEM and DLS is considerably greater for platinum nanoparticles than for gold nanoparticles. This is likely to be caused by the broader particle size distributions obtained for the platinum nanoparticles, but may be caused by a few small aggregates.

The particle size for the Pt dispersions is at the lowest detection limit for the Nanosight (10 nm). It is likely that the Nanosight results in this case are being dominated by the large particles and aggregates.

The Pt dispersions had a black, opaque colour and needed to be diluted > 10 times for DLS and >100 times for nanosight. This may have caused desorption of surfactant and caused some aggregation.

Figure 3.6 shows results for nanoparticles (JN42) prepared using the same procedure as JN8 (Figure 3.5), but on a larger scale.

TEM results show that the majority of CTAB and TTAB stabilized platinum nanoparticles are separated by a space of 2 to 4 nm when dried onto carbon-coated grids, as shown in Figure 3.7b. This separation may be due to the CTAB/TTAB molecules forming a bi-layer around the platinum nanoparticles as depicted in Figure 3.8. In comparison, citrate stabilized gold nanoparticles, prepared by the Frens method [105], appear to be touching (Figure 3.7a). The gold nanoparticles are stabilized in aqueous dispersion by the negative charges on adsorbed citrate ions. These ions are relatively small and do not present a physical barrier to prevent apparent touching of the particles when dried on the TEM grid. The CTAB and TTAB molecules are larger. The CTAB bi-layer is about 2nm thick. This finding is consistent with the work of other authors [132-134], who have found that CTAB forms bi-layers around gold nanoparticles. It is also consistent with the work discussed in Section 2.4.2. TTAB bromide counterions will adsorb preferentially to the Pt surface, creating a negatively charged layer and surfactant

adsorption will be driven by headgroup surface electrostatic forces. The TTAB molecules are likely to adsorb in bi-layers with the ionic head groups interacting with the metal surface.

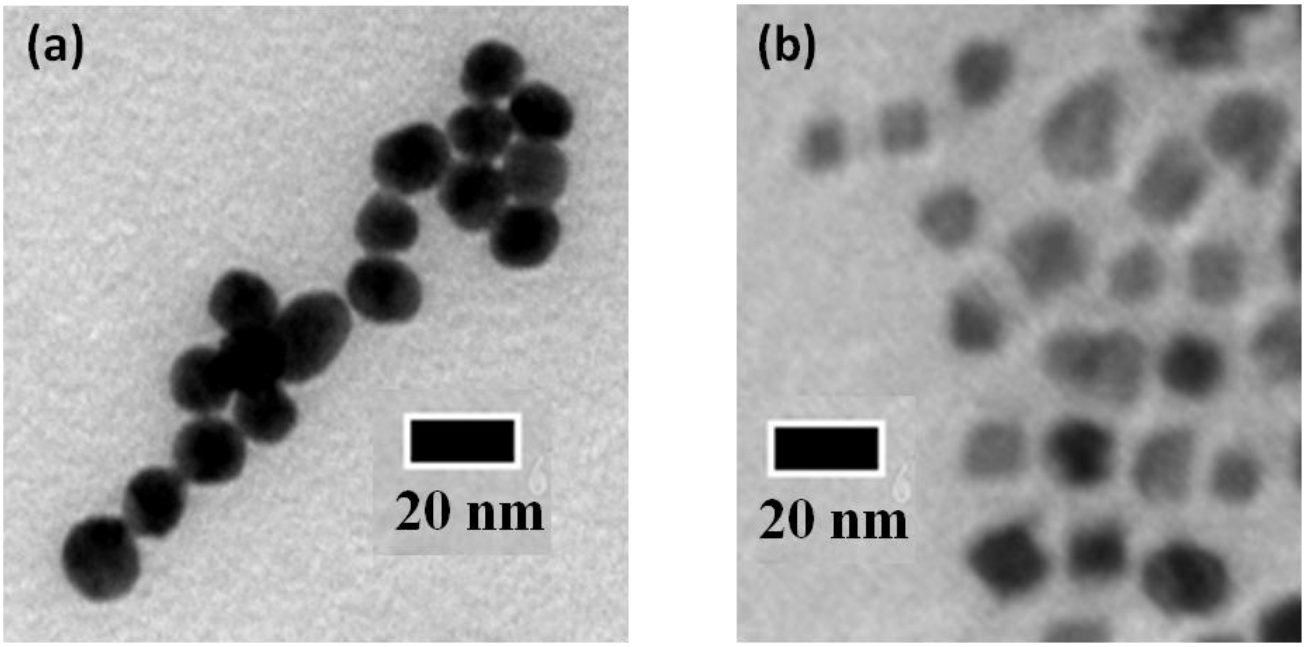

Figure 3-7 *TEM images of (a) Citrate stabilized gold nanoparticles (JN1) b) CTAB stabilized platinum nanoparticles (JN4). Showing a measurable gap between CTAB stabilized particles, while citrate stabilized particle appear to be touching.*

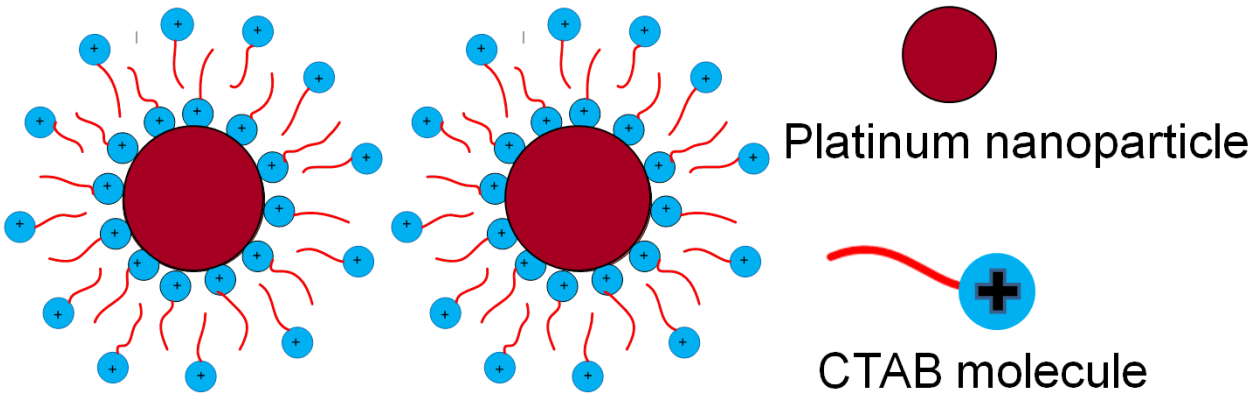

Figure 3-8 *Schematic diagram demonstrating possible method of CTAB stabilisation and cause of observed particle separation in TEMs*

Pt +Other surfactants

Table 3-3 *Pt+other surfactant nanoparticle formulations*

	JN7	JN20	JN21	JN33	JN35	JN36	JN61
$K_2Pt\ Cl_4$/g	0.0063	0.0063	0.0063		0.0033	0.0033	0.005
$H_2PtCl_6.6H_2O$ /g				0.0033			
$NaBH_4$/g	0.0113	0.0113	0.0113	0.005			
Ascorbic acid/g					0.01	0.01	
UHQ water/g	9.385	9.385	9.385	4.99	4.99	4.99	6.0
NP9/g							
Brij O10							0.36
PVP/g	0.597						
SDS/g		0.597		0.12	0.24		
APFA/g			0.597			0.24	
Reaction temperature	50 ºC	50 ºC		20 ºC	50 ºC	50 ºC	50 ºC
Reaction time	6 hrs	6 hrs	6 hrs	4 hrs	4 hrs	4 hrs	24hrs
Observations	Black stable dispersion	Unstable precipitate	Unstable precipitate	Unstable precipitate	No precipitate	No precipiitate	No precipitate

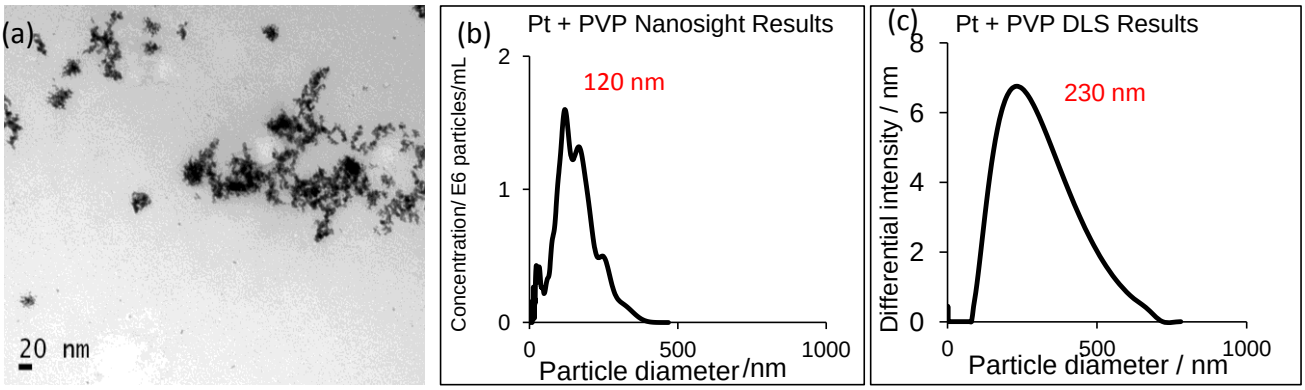

Figure 3-9 Pt+PVP nanoparticles (JN7) (a) TEM, (b) size distribution from Nanosight, (c) size distribution from DLS

An attempt was made to prepare Pt nanoparticles using a range of anionic, nonionic and polymer stabilizers. The formulations are given in Table 3.3; of these only the PVP formulation produced stable nanoparticles. Results for Pt+PVP nanoparticles are shown in Figure 3.9. The dispersion appeared stable aftter several weeks storage. The TEM shows primary particle < 5 nm aggregated into larger flocs.

Table 3-4 *Pt+NP9 nanoparticle formulations*

Pt+NP9

	JN7	JN30	JN34	JN40	JN46	JN47* (Pt+NP9)
$K_2Pt\ Cl_4$/g	0.0063			0.0033	0.033	0.066
$H_2Pt\ Cl_{6.}.6H_2O$ /g		0.066	0.0033			
$NaBH_4$/g	0.0113					
Ascorbic acid/g			0.01	0.02	0.2	
UHQ water/g	9.385	9.88	4.99	4.99	46.6	73.2
NP9/g	0.597	0.12	0.24	0.24	2.4	4.8
Reaction temperature	50ºC	20ºC	20 ºC	50 ºC	50 ºC	50 ºC
Reaction time	6 hrs	6 hrs	24 hrs	4 hrs	4 hrs	4 hrs
Observations	Unstable precipiitate	Unstable precipitate	Black stable dispersion	Black stable dispersion	Black stable dispersion	Black stable dispersion

*JN47 was successfully scaled up, using 0.1g $K_2Pt\ Cl_4$ (JN47R) and 0.2g $K_2Pt\ Cl_4$ (JN47R2)

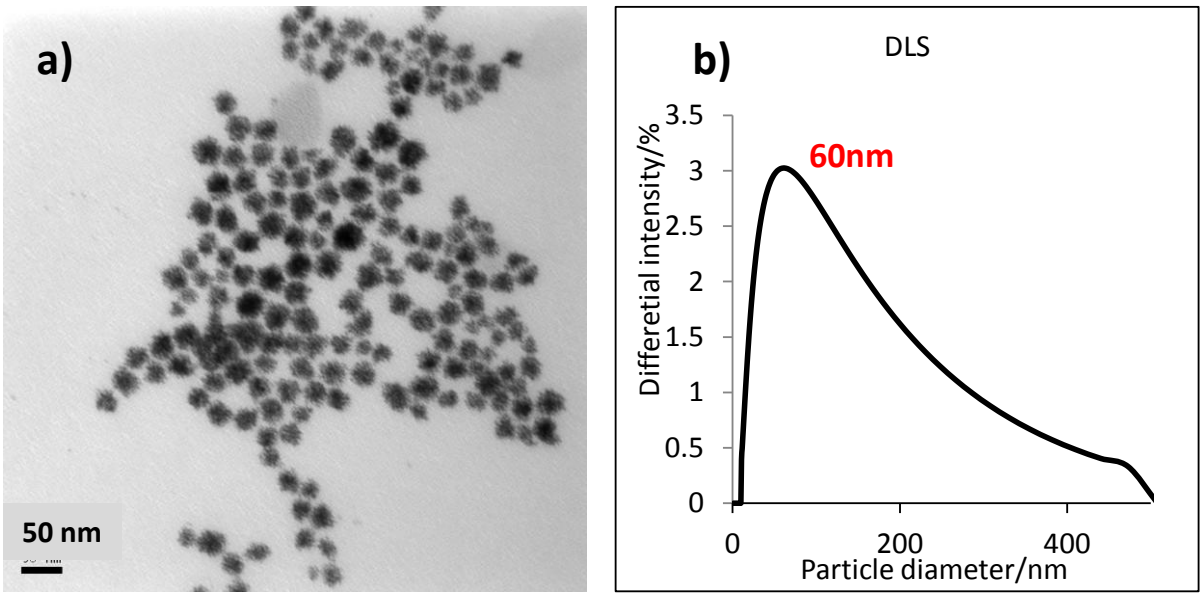

Figure 3-10 *Pt+NP9 nanoparticles (JN40) (a) TEM, (b) size distribution from DLS*

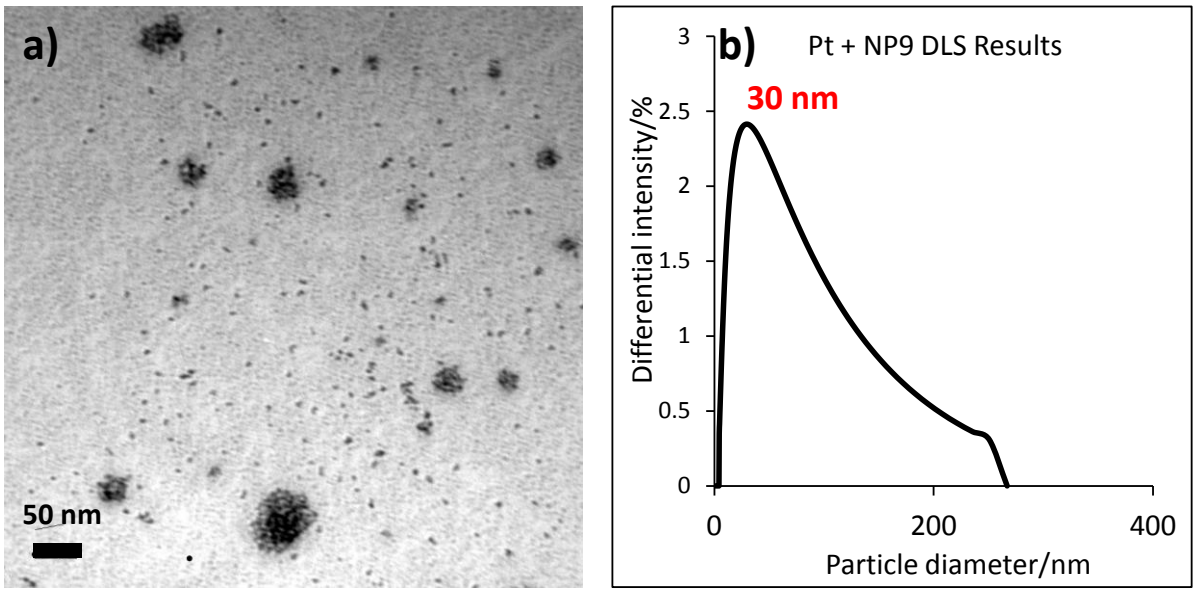

Figure 3-11 *Pt+NP9 nanoparticles (JN34) (a) TEM, (b) size distribution from DLS*

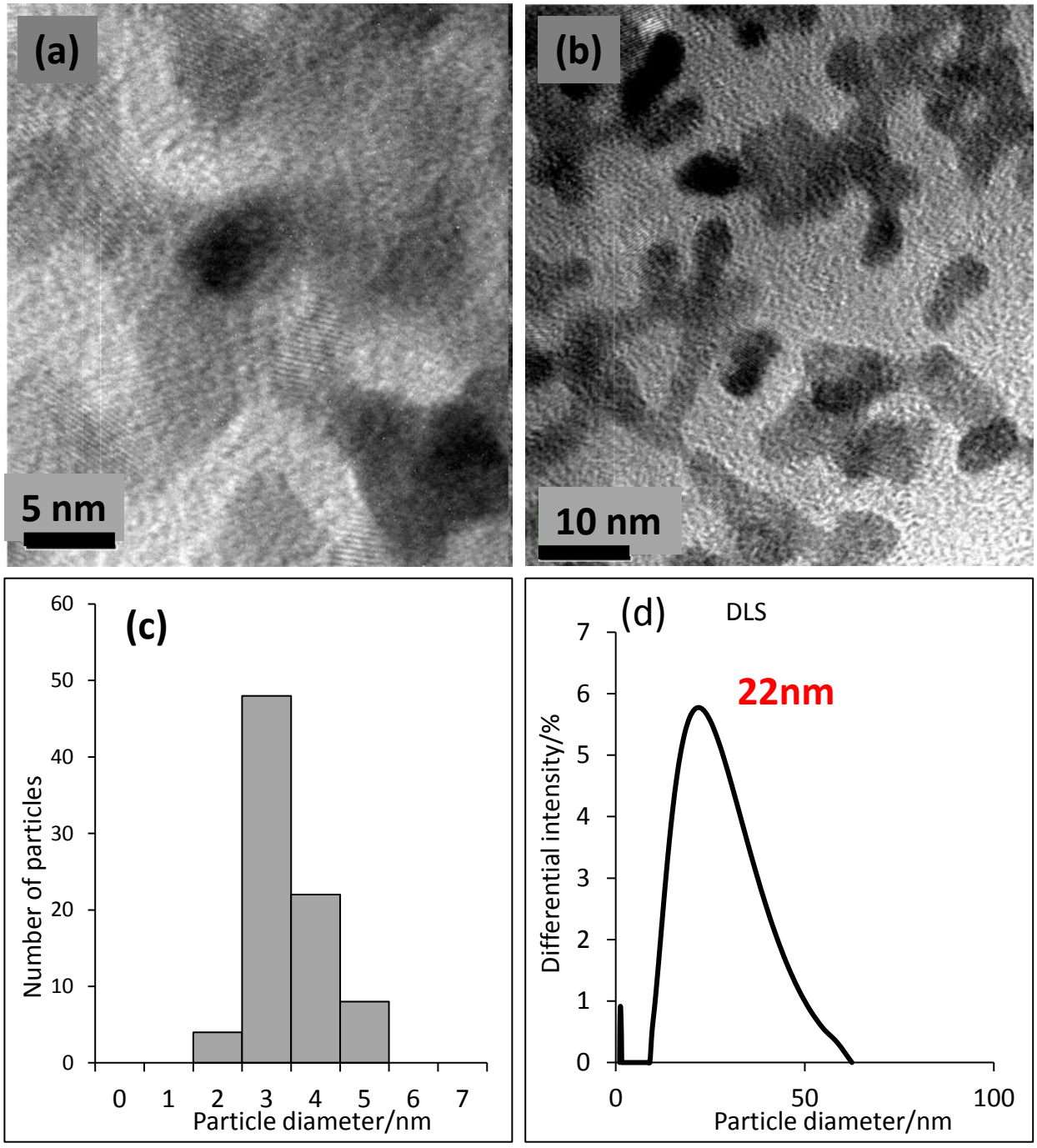

Figure 3-12 *Pt+NP9 nanoparticles (JN46) (a) HRTEM, (b) HRTEM at increased magnification, (c)size distribution from HRTEM, (d)size distribution from DLS*

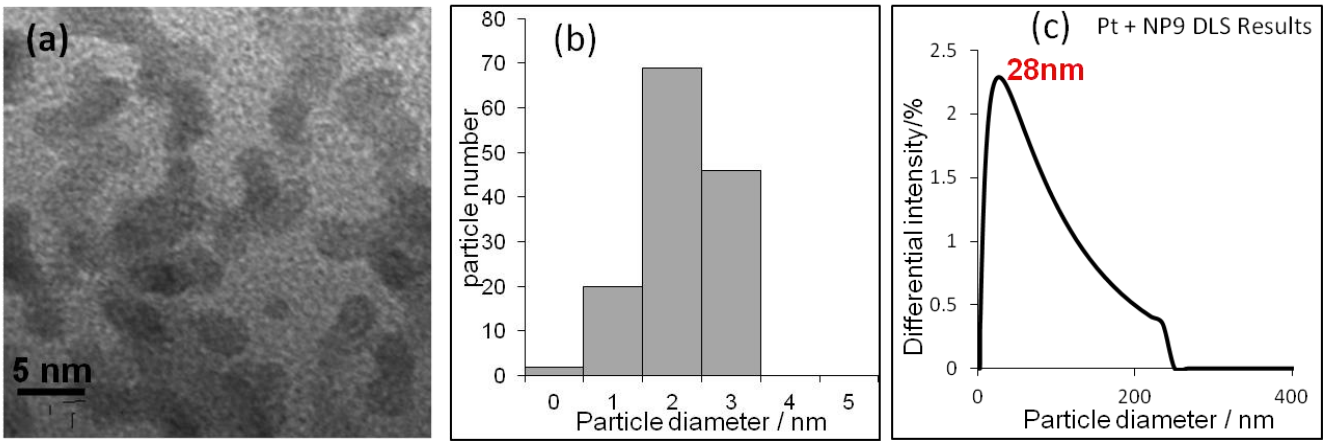

Figure 3-14 *Pt+NP9 nanoparticles (JN47) a) HRTEM, b) size distribution from HRTEM, d) size distribution from DLS*

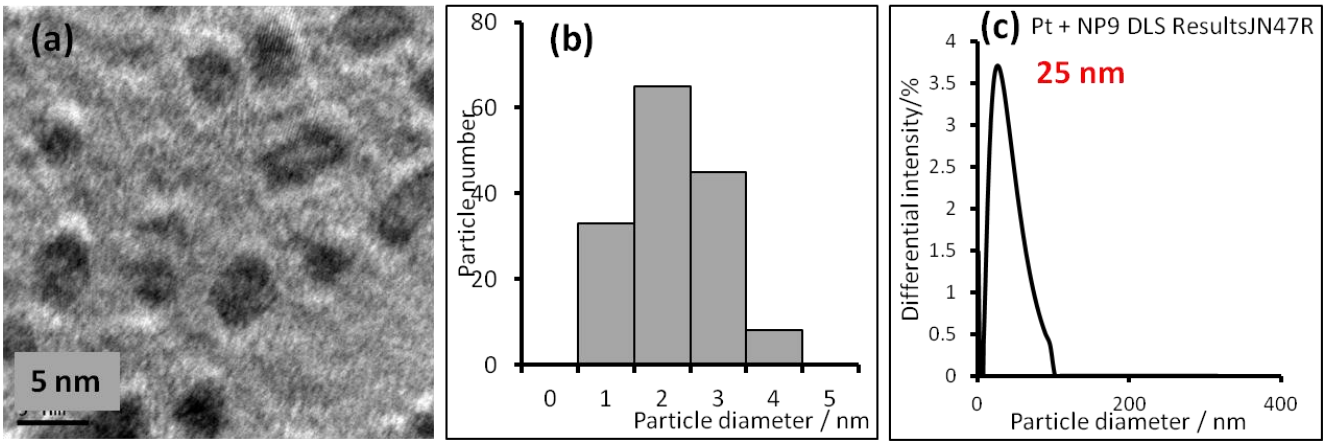

Figure 3-13 *Pt+NP9 nanoparticles (JN47R) (a) HRTEM, (b) size distribution from HRTEM, (d) size distribution from DLS*

The procedure used to prepare the Pt+CTAB/TTAB nanoparticles needed to be adapted in order to give stable nanoparticles with NP9. The formulations are given in Table 3.4 and the results are shown in Figures 3.8-3.14. In some cases ascorbic acid was used as reducing agent, in others NP9 itself acted as reducing agent. All these dispersions appeared stable for several months and the primary particle size

was 2-3 nm. JN47 was stored for over a year, it still appeared stable. TEM and DLS results were unchanged. The procedure was highly repeatable as can be seen from Figure 3.13 and 3.14 which compare samples prepared on separate occasions.

Due to the small size and high colloidal stability of these dispersions purification was difficult. They were centrifuged at 26,000 rpm for 1.5 hours before sedimentation occurred. Electrochemical experiments were conducted using these dispersions, without further purification, in order to investigate the effect of the surfactant on catalysis.

3.6.3 Gold/Platinum Nanoparticles

Polyol procedure

This procedure produced very small nanoparticles 3-5 nm along with some much larger ones, > 20nm. HRTEM images are shown in Figure 3.15. The nanoparticles were analysed by TD Tran [135] using HRTEM, HAADF-STEM and EDX analysis. The results are shown and discussed in detail in his thesis. In summary, the particles did not show a core shell structure. The EDX analysis showed that the smallest particles contain the greatest proportion of platinum, whereas the larger particles consist mainly of gold, as shown in Table 3.5.

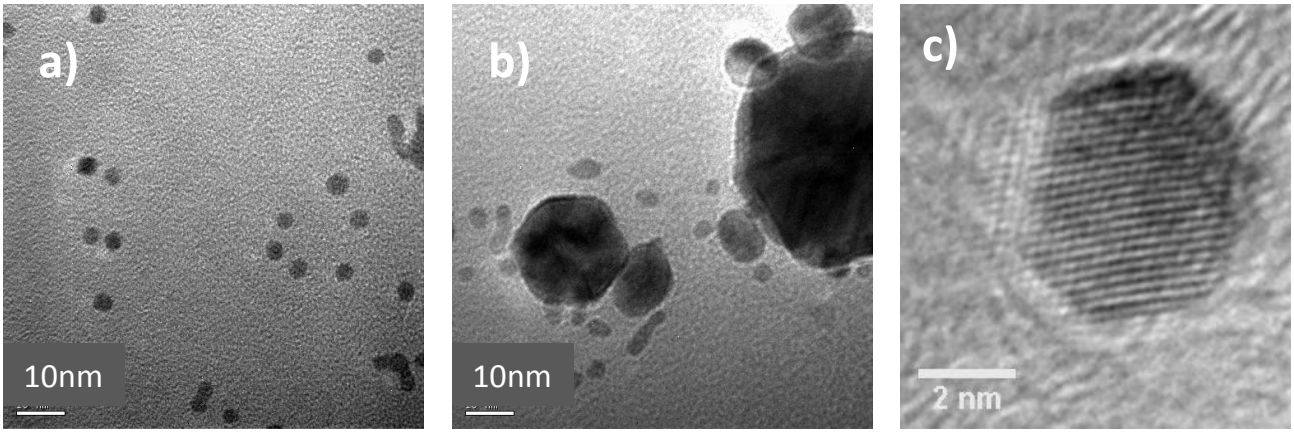

Figure 3-15 *Au/Pt nanoparticles (JN3) HRTEM images a)& b) showing mix of particle sizes c)higher magnification image of one of the smaller particles*

Table 3-5 Pt:Au atomic ratios for PVP-stabilized Au/Pt nanoparticles (JN3) of different sizes

Particle size / nm	4	8	12
Pt:Au ratio	2.45	0.45	0.1

This synthetic route employs PVP as a stabilizer to prevent aggregation and the H_2PtCl_6:$HAuCl_4$ molar ratio added to the reaction mixture was 1:1. H_2PtCl_6 was added to the PVP solution and Pt was allowed to nucleate before addition of $HAuCl_4$. This explains the presence of Pt rich small particles (~ 4 nm). It is interesting that the Au added to these particles has mixed evenly throughout the particle rather than forming a shell around the Pt core. This suggests that the solubility of Au in the nanoparticles is far greater than it would be in the bulk, and is consistent with previous work [115, 116].

Aqueous Procedure

In this case H_2PtCl_4 was reduced in the presence of Au seed particles which were stabilized by citrate. Electron micrographs of nanoparticles prepared by the aqueous route are shown in Figure 3.16. The 2:1 (molar ratio) Au/Pt nanoparticles (JN13) have a ragged surface similar to those reported by Henglein [136]. 'This is understood in terms of the initial formation of Pt islands on the gold particle surface, which then grow in preference to the further reduction on gold. The catalytic action of a Pt surface for the chemical reduction of $PtCl_4^{2-}$ seems to be stronger than that of an Au surface.' Thermodynamic considerations will also be important Pt has higher surface and cohesive energies (2.49 J m^{-2} and 5.48 eV/atom, respectively) than gold (1.50 J m^{-2} and 3.81 eV/atom, respectively) [137-139] and so it is more favourable to have gold surface exposed than platinum surface. The 25:1 Au/Pt nanoparticles (JN11) are not shown as they appear the same as the seed particles. The 1:1 Au/Pt particles have appear larger and have a smooth surface, but some of the seed particles appear to have fused. The size distribution is not shown due to the difficulty in distinguishing individual particles.

Figure 3.17 shows the UV absorption spectra for the Au, Au/Pt and Pt dispersions. The gold seed dispersion JN10 has well dispersed particles of narrow size distribution and the absorbance spectrum shows the characteristic plasmon absorption for gold nanoparticles of this size, at 521 nm. The absorption maximum at 521 nm, typical for gold nanoparticles, is present in the 25:1 Au/Pt but the height of the peak is reduced. At higher proportions of Pt the peak at 521 nm is not present. As the proportion of Pt:Au is increased the UV-Vis. absorption spectrum

resembles more closely that of Pt nanoparticles. The spectrum of the Pt particles (JN4) exhibits an increasing absorption toward shorter wavelengths.

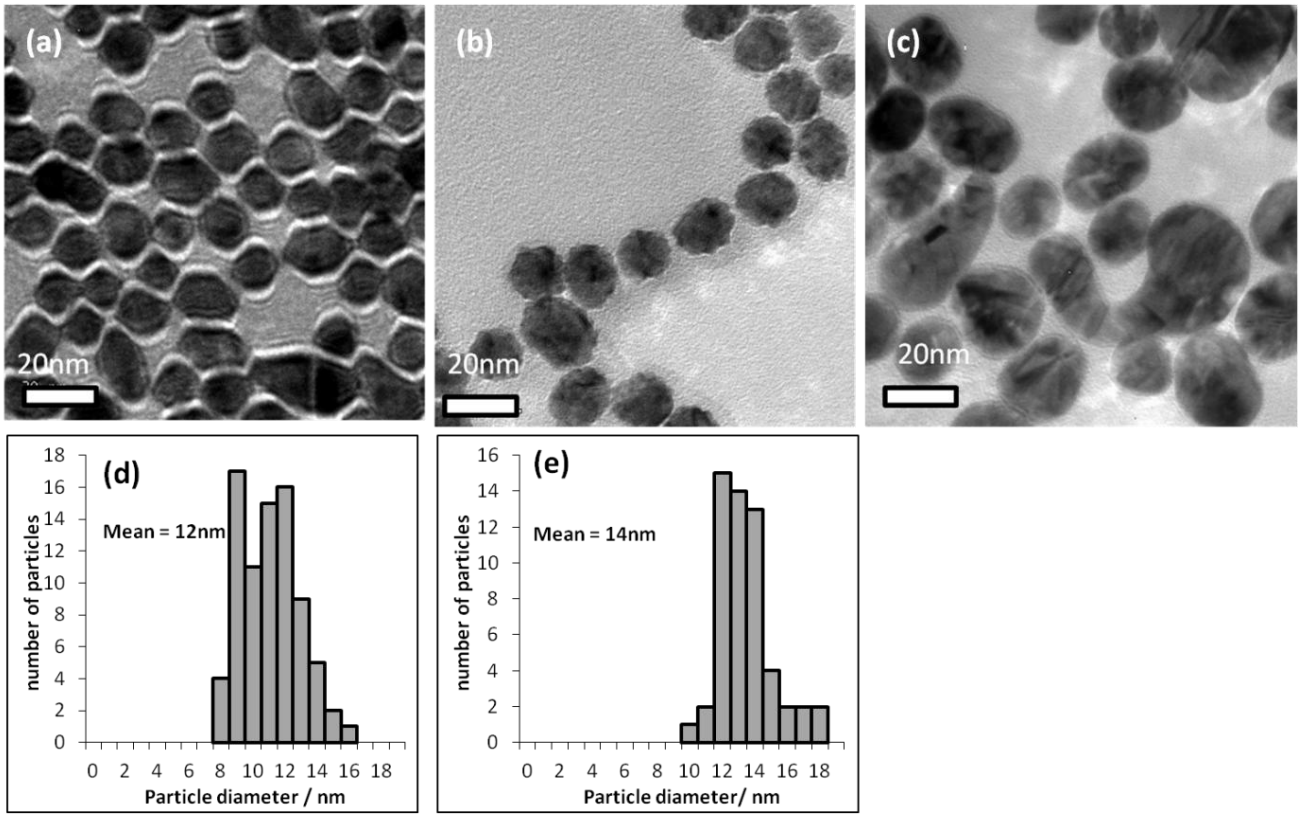

Figure 3-16 *Au/Pt nanoparticles HRTEMs (a) Au seed (JN12), (b) Au/Pt 2:1 (JN13), (c) Au/Pt 1:1 (JN14), (d) size distribution for JN12, (e) size distribution for JN13*

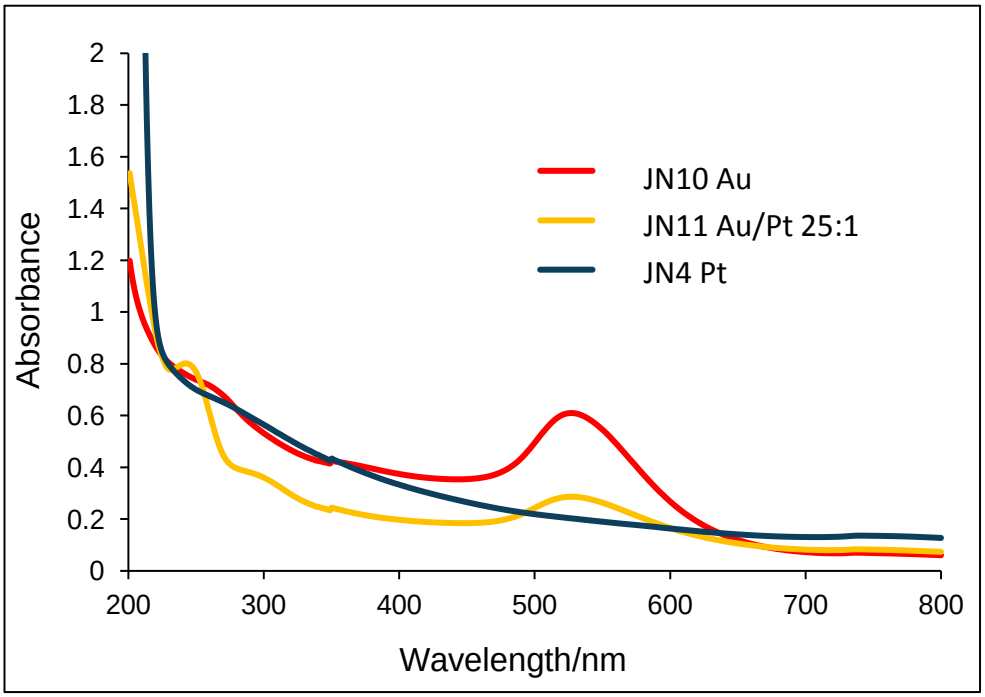

Figure 3-17 *UV-Visible absorption Spectra for Au/Pt Sols. Compared with spectra for Au seed and Pt sol*

3.6.4 Comparison of Particle Size Determination Techniques

In summary it is important to understand the strengths and weaknesses of the technique used. The techniques used here complement each other. DLS and Nanosight give information about particle size in dispersion. Most of the particles used in this work are too small (>10 nm) for accurate Nanosight measurements. TEM allows much more detailed assessment of individual particle size and shape. It is important to view as many particles as possible and take representative micrographs. HRTEM was found to be the most suitable technique for assessing particle size and shape of particles >5 nm diameter. This technique is expensive and requires skilled operation.

3.7 Conclusion

In this chapter the preparation and characterisation of many Pt, Au and Au/Pt nanopartice dispersions have been described. The advantages and disadvantages of several particle sizing methods have been assessed. Au/Pt core shell nanoparticle dispersions were prepared with uniform particle size and shape along with good dispersion and stability. There was not time to scale up and test these particles electrochemically. They could form an interesting fuel cell catalyst. The size of the gold seed and proportion of Pt could be varied.

Two Pt nanoparticle dispersions were chosen for electrochemical testing, to test whether the surfactant blocks electrochemical sites or has a beneficial effect. Pt+NP9 and Pt+TTAB (JN47 and JN42) dispersions could be reliably repeated and scaled up.

Chapter 4 Oxygen Reduction on Platinum

In this chapter rotating ring disc experiments are described using platinum ring and disc electrodes. The electrochemical measurements were first carried out on the clean polycrystalline platinum disc. The purpose of these experiments was to confirm that reproducible results could be obtained which compared well with those expected from the literature. This was important before using the techniques to test nanoparticle catalysts. In chapter 6 the effect of surfactants on Pt electrochemistry is investigated and in chapter 7 the method is used to investigate the catalytic performance of platinum nanoparticles.

4.1 Fundamental Electrochemistry

In this section the main theoretical concepts of electrochemistry, relevant to fuel cell applications, are explained. The main topic of interest in this work is the catalytic performance of platinum towards the oxygen reduction reaction (ORR). Half-cell experiments, using a rotating disc electrode and aqueous electrolytes are often used to investigate new electrocatalyst materials. Half-cell testing has advantages over testing which involves preparation of single-cell PEMFCs (described in Chapter 7), for initial testing of catalyst materials and fundamental research; it involves fewer variables and requires smaller quantities of catalyst material (a few μg).

4.1.1 Thermodynamics

The maximum net work, ΔG, which can be obtained from a chemical reaction is the change in the free-energy of the reaction. Consider the reaction

$$O + e^- \rightleftharpoons R \quad (4.1)$$

The free energy of reaction varies with temperature and activity of reactants,

$$\Delta G = \Delta G^0 + RT \ln \frac{[R]}{[O]} \quad (4.2)$$

Where ΔG^0 is the standard free energy change for the reaction, R is the gas constant (8.314 J K^{-1} mol^{-1}) and T is the absolute temperature at which the reaction is occurring. $[R]$ is the activity of species R, $[O]$ is the activity of species O. For an electrochemical reaction, free energy of reaction relates to the maximum electrical work that can be done as follows,

$$\Delta G = -nFE \quad (4.3)$$

This gives rise to the **Nernst equation**:

$$E = E^0 - \frac{RT}{nF} \ln \frac{[R]}{[O]} \quad (4.4)$$

E is the measured potential difference of the cell, E^0 is the standard cell potential, F is the Faraday constant (96485 C mol^{-1}) and n is the number of electrons transferred.

This explains how the electrode potential varies with temperature and reactant concentrations, under equilibrium conditions, where no net current flows.

4.1.2 Electrode Kinetics

The Nernst equation gives the electrode potential at equilibrium. In this section the non equilibrium situation will be explored. This happens, for example, if a potential is applied. Electrochemical reactions involve the transfer of electrons, to or from the electrode material, to one or more reactants. The electrical current flowing is a direct measure of the rate of the reaction. The forward and reverse reaction rates can be expressed as:

$$\vec{J} = J_0 e^{\frac{-\alpha F\eta}{RT}} \qquad \overleftarrow{J} = J_0 e^{\frac{(1-\alpha)F\eta}{RT}} \tag{4.5}$$

J_0 is the exchange current density; this is a measure of the amount of electron transfer at equilibrium, when the rates of forward and reverse reactions are equal.

$\vec{J}$ and $\overleftarrow{J}$ are the current densities for the forward and reverse reactions measured at an overpotential $\eta = E - E_{eq}$ where E is the applied potential and E_{eq} is the equilibrium potential, n is the number of electrons transferred in the rate determining step, α is the transfer coefficient ($0 < \alpha < 1$) and is normally assumed to equal 0.5 [140], for a single electron process.

The net rate of reaction (net current) can be obtained by subtracting the backward reaction from the forward reaction. This gives the **Butler-Volmer equation** (4.6)

$$J = \vec{J} - \overleftarrow{J} = J_0 \left[e^{\frac{-\alpha nF\eta}{RT}} - e^{\frac{(1-\alpha)nF\eta}{RT}} \right] \tag{4.6}$$

At high negative overpotentials, the Butler-Volmer equation simplifies to:

$$J_k = J_0 e^{\frac{-\alpha nF\eta}{RT}} \tag{4.7}$$

$$lnJ_k = ln\, J_0 - \frac{\alpha nF\eta}{RT} \quad (4.8)$$

$$logJ_k = log\, J_0 - \frac{\alpha nF\eta}{2.303RT} \quad (4.9)$$

$$\eta = \frac{2.303RT}{\alpha nF} logJ_0 - \frac{2.303RT}{\alpha nF} logJ_{\mathrm{k}} \quad (4.10)$$

It is clear from (4.8) that a plot of lnJ_k against η should give a straight line, from which the number of electrons transferred in the rate determining step can be calculated. The exchange current density (J_0) can be determined by extrapolating to η =0. This is known as a **Tafel plot.**

4.1.3 The Rotating Disc Electrode (RDE)

When measuring rates of electrochemical reactions, the reaction rate is dependent on the concentration of reactants at the electrode surface. At some point the rate is limited by the rate at which reactants can move towards the electrode surface (mass transport effects). The working electrode is rotated at known uniform rates.

The Rotating Ring Disc Electrode (RRDE)

The reduction of O_2 on Pt may proceed via two routes: either directly to H_2O via a 4-electron pathway (4.11), or via a 2-electron series pathway to H_2O_2, as shown in (4.12).

$O_2 + 4H^+ + 4e^- \rightleftharpoons 2H_2O \quad E^0 = 1.23$ V (4.11)

$O_2 + 2H^+ + 2e^- \rightleftharpoons H_2O \quad E^0 = 0.672$ V (4.12)

The RRDE can be used to measure peroxide production during ORR [141-143]. It is a variation on the RDE in which the disc electrode is surrounded by a concentric Pt ring electrode as shown in Figure 4.1. Peroxide generated on the disc, flows outwards towards the ring, under rotation, and is oxidised according to the reverse reaction (4.12).

In this work the potential on the ring was held at +1.1 V, so that the oxidation of peroxide proceeded under pure diffusion limitation. In practice only a fraction of the peroxide produced is detected, and the *collection efficiency, N,* of the RRDE can be measured experimentally [144]. Once the collection efficiency is known, the rate of peroxide formation can be calculated at any potential using Equation (4.13) [145]:

$$X_{H_2O_2} = \frac{2I_R N}{I_D + I_R N} \qquad (4.13)$$

Where $X_{H_2O_2}$ is the number of moles of H_2O_2 formed per mole of O_2, I_R is the ring electrode current and I_D is the disc electrode current. The rate of peroxide formation is dependent on the disc potential. with Pt/C catalyst typically yielding 5-10 % H_2O_2 at *E*=+1.1 V [141-143].

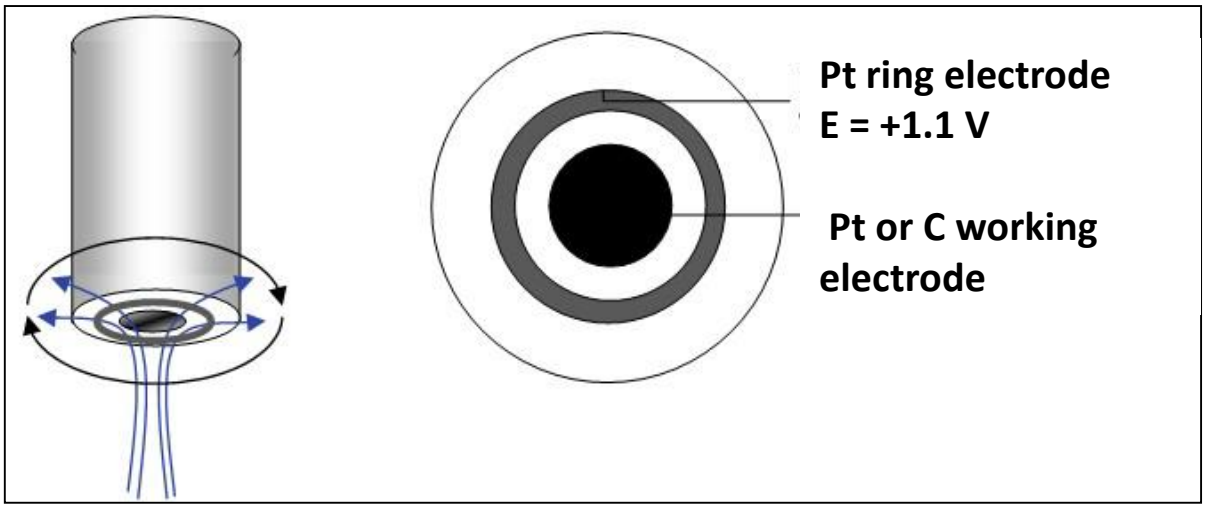

Figure 4-1 *Schematic of the RRDE assembly and its mass transport characteristics*

4.2 Experimental Methods and Materials

Electrochemical measurements were carried out using a Metrohm Autolab PG302N potentiostat with an FRA2 impedance module, a SCAN250 analogue scan generator and a BA bipotentiostat/array. The jacketed glass electrochemical cell was enclosed in a grounded Faraday cage. A reversible hydrogen electrode (RHE) was used as reference electrode, to avoid contamination with impurities. This was prepared in-house and was similar to that described by Garsany [146]. The electrode consisted of a platinised Pt gauze (300 mesh) sealed in a glass pipette, which was then filled with 0.1 M $HClO_4$. Hydrogen was generated on the Pt gauze by electrolysis so that the electrode was half filled with hydrogen. All potentials in this work are referred against the RHE. The RHE potential was measured against the Ag/AgCl reference electrode before and after each experiment, to confirm the stablility of the electrode. Counter electrodes for this study were made from Pt

gauze (300 mesh, Alfa Aesar) with surface areas of >10 cm^2, and were flame-annealed before experiments to remove impurities.

Rotating ring disc electrodes (RRDE) with removable 5 mm diameter glassy carbon and Pt discs enclosed in PTFE with Pt ring were purchased from Pine Instruments (USA). The diameters of the Pt and carbon discs were found, by white light interferometry, to be 5 mm within 0.01 mm. The electrodes were polished on Microcloth™ (Buehler) using aqueous alumina slurries of 1 μm, 0.3 μm and 0.05 μm grain size in sequence. The polished electrodes were rinsed well with Milli-Q ultra pure water, with resistivity ≥18.2 MΩ cm, then sonicated (40 kHz bath) for 30 seconds in Milli-Q water to remove any residual alumina.

A jacketed glass electrochemical cell was cleaned by soaking in a 50:50 mixture of concentrated nitric acid and sulphuric acid for several hours. The cell was rinsed thoroughly with Milli-Q water and then rinsed with the electrolyte solution, a 0.1 M $HClO_4$ solution (prepared from 70% TraceSelect, Sigma and Milli-Q water). 110 mL of this solution was then added to the cell.

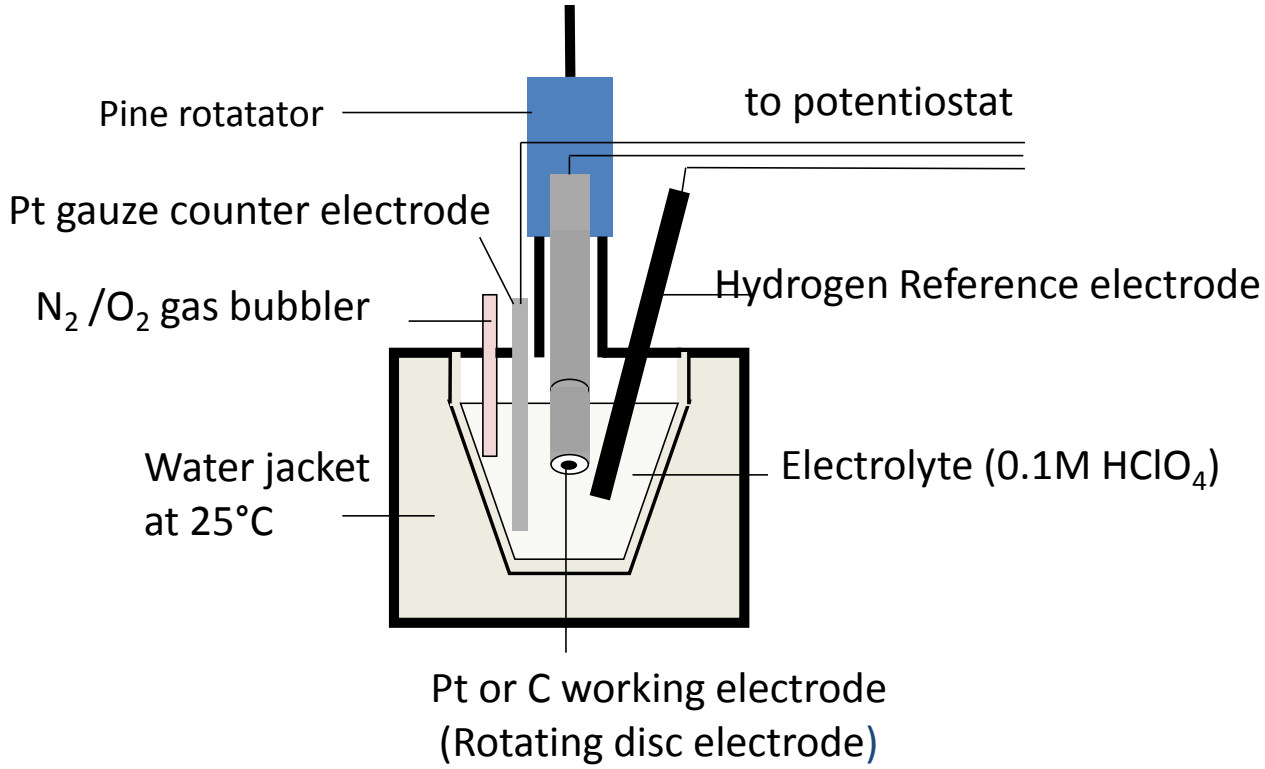

Figure 4-2 *Schematic diagram of experimental setup used for the half cell electrochemical characterisation of electrocatalysts*

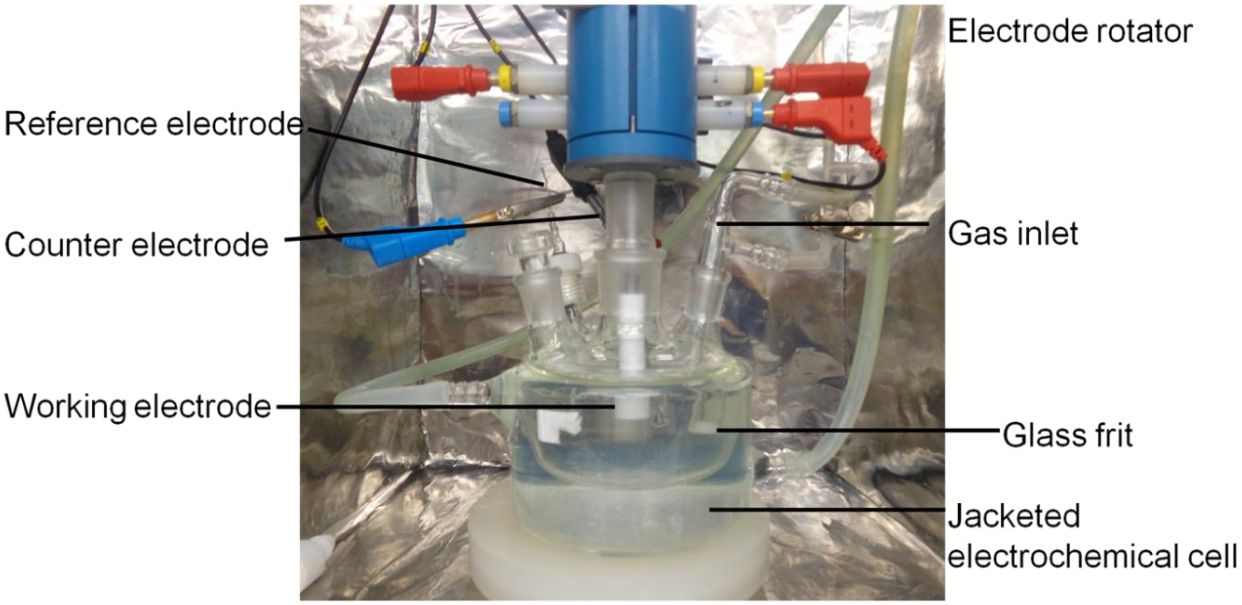

Figure 4-3 *Experimental setup used for the half cell electrochemical characterisation of electrocatalysts in this work.*

The working electrode was mounted in an RDE assembly (ASR, Pine Instruments, USA) and immersed in the electrolyte. Air bubbles were removed from the electrode surface by rotating the electrode briefly. The cell was thermostatted at 25 ºC using a circulating water bath. The electrolyte was purged with nitrogen (Grade 4.8, ultra-high purity, BOC) for at least 30 minutes before electrochemical conditioning of the working electrode. This involved cycling between +0.05 and +1.0 V at 250 mV s^{-1} for up to 200 cycles, until stable cyclic voltammograms were observed. For the measurement of ECSA, cyclic voltammograms were recorded using analogue scan cyclic voltammetry (using the SCANGEN module) at 25 mV s^{-1} between +0.05 and +1.1 V.

The oxygen reduction reaction (ORR) polarization curves were measured and corrected for capacitive current and ohmic resistance of the solution. Background linear sweep voltammograms (LSVs) were recorded, while the solution was saturated with N_2, from +0.05 to +1.1 V at 25 mV s^{-1} at the following rotation rates 400, 800, 1200, 1600, 2000, 2400 and 2800 rpm. The electrolyte was then bubbled with oxygen (N5 ultra-high purity, BOC Special Gases) for at least 30 minutes. LSV scans were then repeated in the O_2 saturated electrolyte at the same rotation rates. While measurements were being taken, the appropriate gas was allowed to flow above, rather than below the solution maintaining positive pressure. As far as possible the cell was sealed to the external atmosphere. The Ohmic resistance of the electrolyte was measured using electrochemical impedance at 10 kHz, using an AC perturbation of 5 mV. The oxygen concentration was measured using a Clark cell at intervals throughout the ORR experiment and was found to remain

approximately constant at (1.02±0.15) $\times 10^{-6}$ mol cm^{-3}. It was important to demonstrate that the oxygen concentration remained constant throughout the experiments because the limiting current is dependent on oxygen concentration(*C*) (equation 4.21). In the calculations the value for *C* of 1.26 x 10^{-6} mol cm^{-3} (at 25 ºC), commonly used by other authors in the field [147, 148] was chosen.

4.2.1 Measurement of RRDE Collection Efficiency

In an RRDE experiment, only a fraction of the electroactive species generated on the disc is detected by the ring. This fraction is known as the collection efficiency (*N)* and can be calculated theoretically [149] from the geometry of the electrode, using the three principal diameters: the disc outer diameter, the ring inner diameter and the ring outer diameter. In practice, the actual RRDE dimensions may not be known due to uncertainties in the machining process and changes in the dimensions caused by electrode polishing or temperature cycling.

As a test system it was decided to measure experimentally the collection efficiency using the ferricyanide/ferrocyanide redox couple. The RRDE was placed in a solution containing 10 mM potassium ferricyanide in 0.1 M NaOH background electrolyte. A silver/silver chloride reference electrode was used. The disc potential was swept from + 0.6 to + 0.0 V (vs. RHE) at 25 mV s^{-1} and the ring potential was maintained at +1.1 V vs. RHE, so that the reaction occurring at the ring was entirely diffusion-limited. The results are shown in Figure 4.4. Initially, both the ring and disc electrodes were held at a positive potential so that no reaction occurred. When the

potential of the disc electrode was swept towards more negative potentials, a cathodic current was observed which corresponds to the reduction of ferricyanide to ferrocyanide at the disc, as in equation (4.14).

$$Fe(CN)_6^{3-} e^- \rightarrow Fe(CN)_6^{4-} \quad (4.14)$$

As ferricyanide was reduced at the disc electrode, the ferrocyanide generated was swept outward away from the disc electrode and toward the ring electrode. The ring electrode was held constant at a +1.1 V (vs.RHE) throughout the experiment. Some (but not all) of the ferrocyanide generated at the disc travelled close enough to the ring electrode that it was oxidized back to ferricyanide. The anodic current at the ring electrode is due to the oxidation of ferrocyanide to ferricyanide, as in equation (4.15).

$$Fe(CN)_6^{4-} \rightarrow Fe(CN)_6^{3-} + e^- \quad (4.15)$$

The ratio of the ring limiting current to the disc limiting current is the collection efficiency (N).

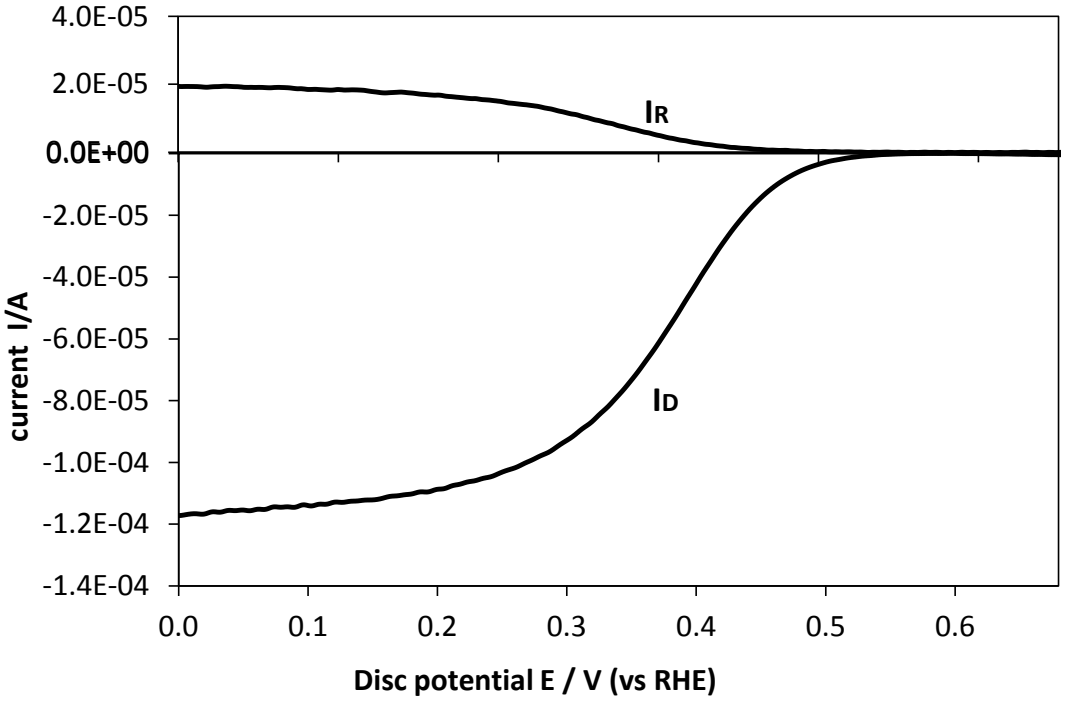

Figure 4-4 *Currents measured at the Pt disc and Pt ring electrodes for the ferri/ferrocyanide redox couple at 1600 rpm*

The measured ratio of the ring limiting current to the disc limiting current is the collection efficiency (N). As the rotation rate increases, both the disc and the ring currents increase. The collection efficiency is expected to be independent of the rotation rate. Using this method the collection efficiency was calculated to be N=0.21. The theoretically calculated collection efficiency given by the manufacturer for this (E6 series) electrode was N=0.256 [150]. This is calculated using precise measurements for ring and disc and assuming the surface is completely flat, In practice it is not possible to manufacture the electrode with such precision.

4.3 Results and Discussion

4.3.1 Cyclic Voltammetry

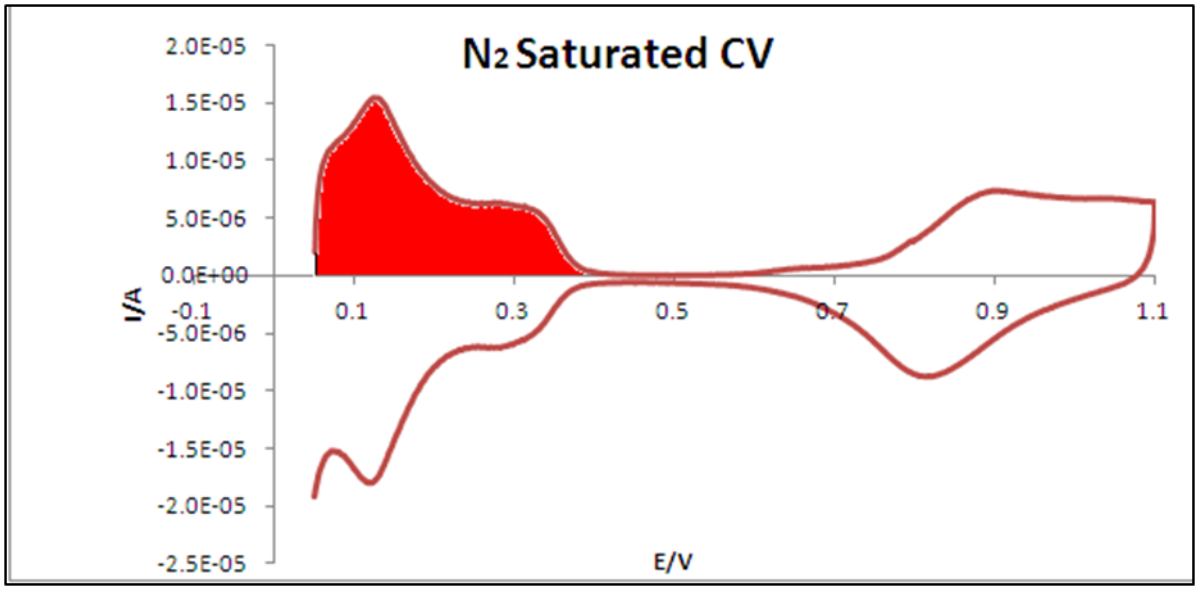

Figure 4-5 *CV recorded at 25 mV s^{-1} in N_2-saturated electrolyte for 5mm Pt disc electrode in 0.1 M $HClO_4$ at 25 ºC, showing shaded region due to H_{upd} desorption.*

Figure 4.5 shows the cyclic voltammogram (CV) of the 5 mm Pt disc electrode. The voltammogram shows characteristic H desorption peak [151-155] at 0.12 and a plateau between 0.22 V and 0.3 V, along with the corresponding cathodic adsorption peaks. The peak at 0.12 V is thought to result from hydrogen underpotential deposition (H_{upd}) on Pt (110) sites, while the peak at 0.22 V corresponds to Pt (100)-type step sites or terrace sites close to steps and high co-ordination edge and corner Pt sites [43, 47, 156-158]. The peaks at voltages greater than 0.6 V are caused by adsorption and desorption of oxygen species [47].

Electrochemical surface area (ECSA) was measured by integrating the desorption wave for underpotentially deposited hydrogen and assuming a charge passed per unit area of Pt of 210 C cm^{-2} [159]. ECSA is typically higher than the geometric area of the electrode. The ratio of the electrochemically active surface area to the geometric surface area is known as the roughness factor [66]. In an acidic electrolyte, H^+ is reversibly adsorbed, on platinum to form a full monolayer at potentials between +0.05 and +0.4 V vs RHE via the reaction [160]:

$$Pt + H^+ + e^- \longrightarrow Pt - H_{upd} \quad (4.16)$$

where H_{upd} represents underpotentially-deposited hydrogen adsorbed on the platinum surface. A baseline is set to correct for capacative current as shown in Figure 4.5 (although this is barely noticeable for the Pt disc). The integrated area of the H_{upd} desorption peak gives total charge passed during H^+ desorption (Q_H). The electrochemically active surface area ECSA (cm^2) can then be calculated using equation 4.17

$$ECSA = Q_H / \sigma_H \quad (4.17)$$

Where σ_H = 210 μC.cm^{-2}, which is the charge required for the formation of a monolayer of H_{upd} on a clean, smooth polycrystalline Pt surface. This value for σ_H is only approximately correct for highly-faceted Pt nanoparticle surfaces, but is widely used in the literature [146, 161].

4.3.2 Oxygen Reduction

The ORR is a complex electrochemical reaction, involving several steps, with the overall transfer of 4 electrons. It has been studied extensively [162-167] but there is

no general agreement on the exact reaction mechanism, or even the rate-determining step, for the ORR on platinum [168]. There are several possible mechanisms for the overall reaction, which exhibit strong dependence on the nature of the electrode surface.

The mechanism of the reaction has been simplified by Damjanovic, as a multistep process in which more than one reaction pathway can be followed, as shown in Figure 4.6 [165].

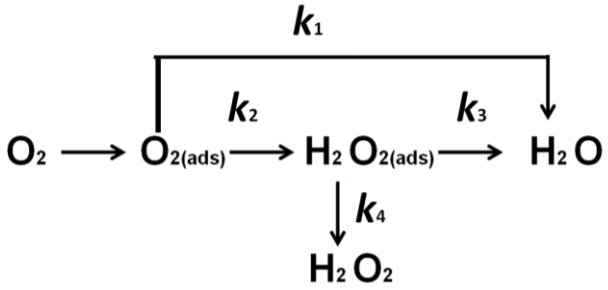

Figure 4-6 *Simplified multistep reaction pathway for the ORR*

According to this scheme, molecular oxygen is first adsorbed onto the Pt surface to form $O_{2(ads)}$..Reduction of $O_{2(ads)}$ can proceed either via a "direct" $4e^-$ pathway (with rate constant k_1), or via a peroxide intermediate ($H_2O_{2(ads)}$) which can undergo either a further $2e^-$ reduction to water (rate k_3) or desorption from the surface into solution (k_4). It is preferable from a themodynamic point of view for the H_2O_2 to remain adsorbed and be reduced to water since the four-electron pathway in reaction 4.11 generates a larger cell voltage than the two-electron pathway in reaction 4.12. This is considered to be the mechanism on Pt surfaces and the rate determining step is addition of the first electron to O_2 [169]. Production of H_2O_2 is

also unfavourable in fuel cells because it accelerates degradation of the polymer membrane.

During the RRDE experiment, the ring is held at a positive potential, at which hydrogen peroxide is oxidized. In this way, hydrogen peroxide intermediates produced during the ORR at the disc can be detected by monitoring the current of the ring electrode. The Pt ring potential in these experiments was held at +1.1 V, such that the reaction occurring at the ring was entirely diffusion-limited and the ring current was used to investigate the selectivity of the reaction. The RRDE results for the Pt disc are shown in Figure 4.7.

The ORR polarization curves for the Pt disc (Figure 4.7) show a single reduction wave at each rotation speed and limiting current density plateau.

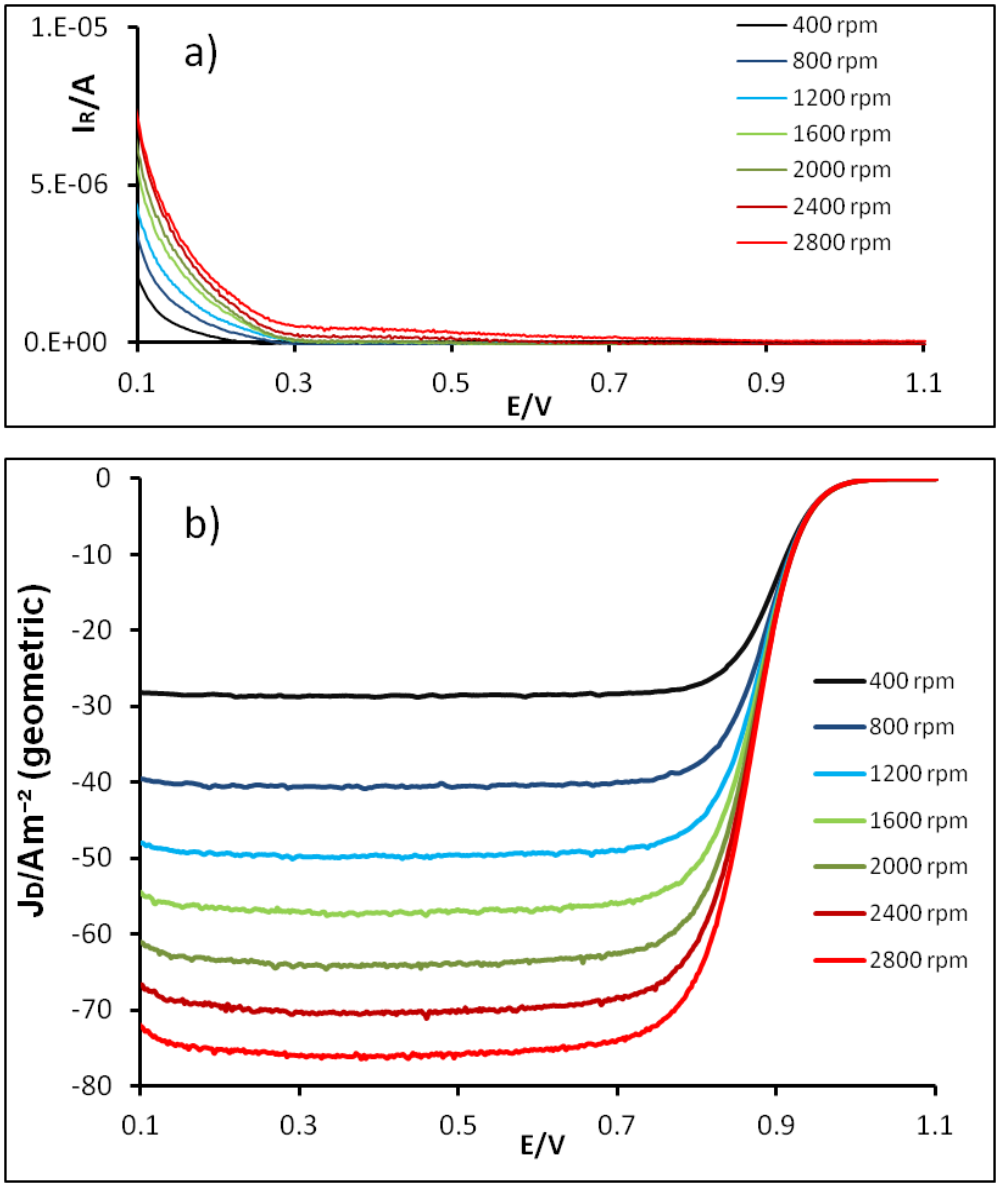

Figure 4-7 *Anodic polarisation curves for 5mm Pt disc electrode in 0.1 M $HClO_4$ at 25 ºC(background and iR corrected) recorded in O_2-saturated electrolyte at 25 mV/s at various rotation rates; a) Ring current (ring potential held at 1.1 V), b) disc current.*

The number of electrons transferred, n, can be quantified from the disc and ring currents using equation (4.18) [170]

$$n = \frac{4I_D}{I_D + (I_R/N)} \qquad (4.18)$$

where I_D is modulus of the total disc current $|I_D(H_2O)+I_D(H_2O_2|$, I_R is the ring current (corresponding to the oxidation of H_2O_2) and N is the collection efficiency (determined as 0.21 in a separate experiment using the ferro/ferricyanide couple [144].). If the reaction has 100 % selectivity toward water, I_R=0 and n=4, whereas if the reaction has 100 % selectivity toward hydrogen peroxide, $I_R/N=I_D$ and n=2. Figure 4.8b presents a plot of n as a function of potential calculated, using equation 4.18, from the RRDE data acquired at 1600 rpm for the Pt RRDE. This compares well with the data (Figure 4.8a), calculated using the gradients of the Koutecky-Levich plots (equation 4.20). The data shows that n is close to 4 for the Pt disc at potentials positive of ca +0.3 V, indicating that water is the main product of the ORR.

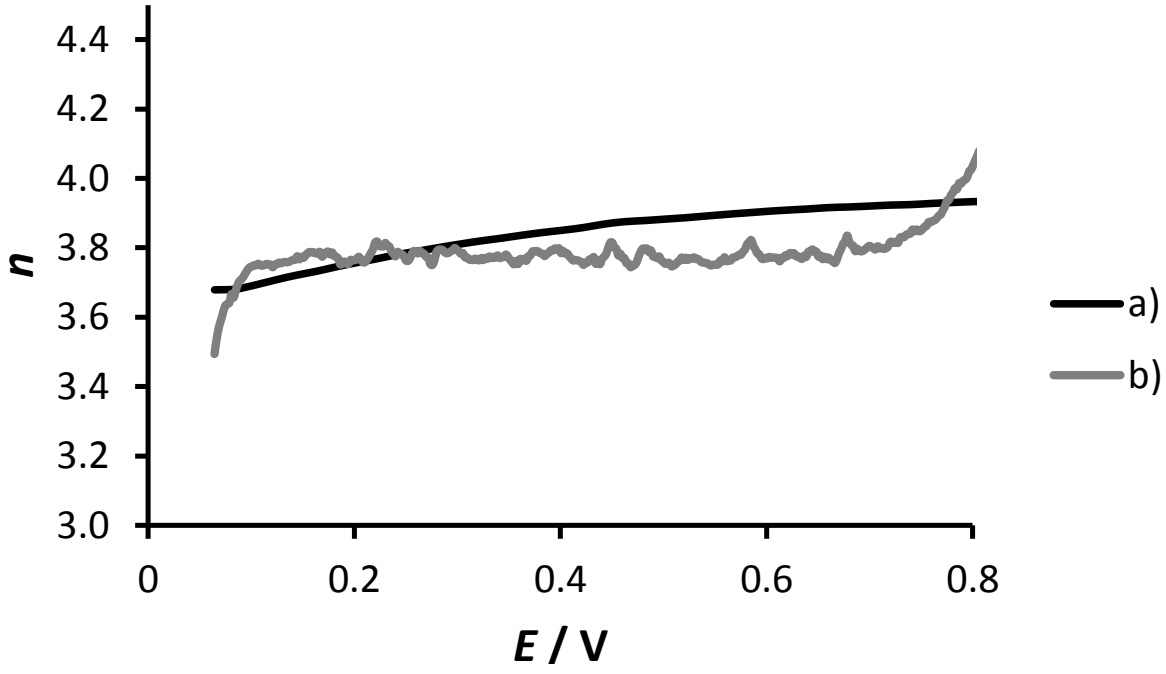

Figure 4-8 n *as a function of potential for the Pt disc, a) calculated from the RRDE data acquired at 1600 rpm, using equation (4.18), b) calculated from gradients of Koutecky-Levich plots (Figure 4.11)*

The selectivity of the reaction can also be represented by the fraction of H_2O_2 ($X_{H_2O_2}$) produced in the reaction, which can be calculated from equation (4.19) [145]

$$X_{H_2O_2} = \frac{2(I_R/N)}{I_D + (I_R/N)} \quad (4.19)$$

Values of $X_{H_2O_2}$ are plotted as a function of potential in Figure 4.9. A significant increase in $X_{H_2O_2}$ is observed in the H_{upd} region (E < 0.2 V). This observation has previously been attributed to competitive adsorption of hydrogen, below 0.2 V, which results in blocking of active sites, hindering the dissociative adsorption of oxygen molecules [171].

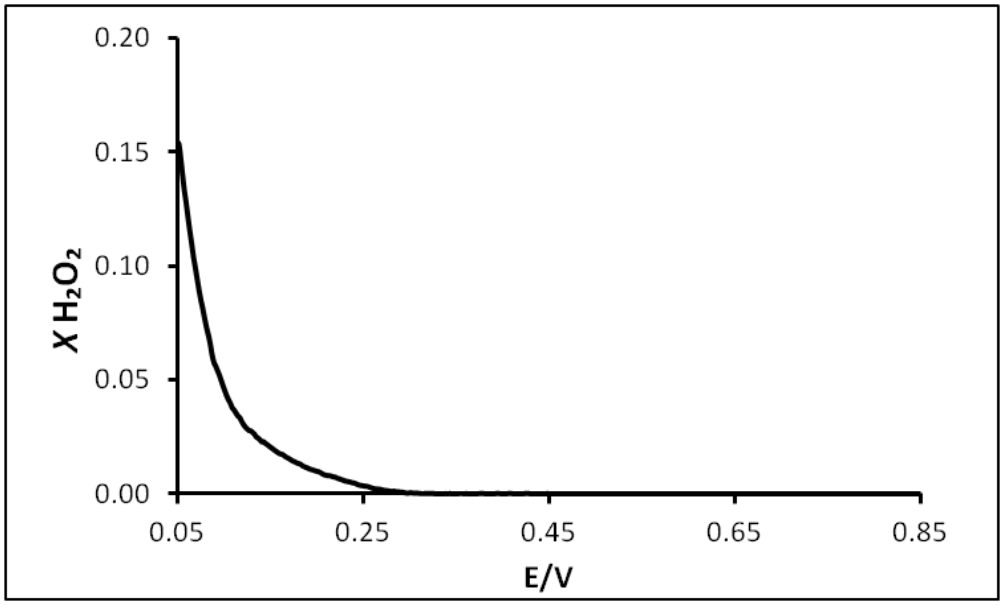

Figure 4-9 *Fraction of H_2O_2 formation during O_2 reduction on Pt disc at 25 ºC in 0.1 M $HClO_4$ saturated with O_2. Calculated from the data in Figure 4.7 (at 1600 rpm) using Equation (4.19) with N = 0.21*

Kinetics of the ORR

It is of interest to evaluate the kinetics of the overall reaction, from the point of view of performance of the fuel cell. The **Koutecky-Levich** equation (4.20) relates the

measured current density J to the diffusion-limited current density J_L and the kinetically controlled component of current density, J_K

$$\frac{1}{J} = \frac{1}{J_k} + \frac{1}{J_L} \quad (4.20)$$

where J is the current density, J_K is the kinetic current density and. J_L is the mass transport-limited current density, given by the Levich equation (4.21):

$$J_L = 0.2006nFCD^{2/3}v^{-1/6}\omega^{1/2} \quad (4.21)$$

where n is the number of electrons transferred, F is the Faraday constant, C is the bulk concentration of electroactive species in solution (1.26 x 10^{-6} mol cm^{-3} [147, 148], at 25 ºC), D is its diffusion coefficient (1.93x10^{-5} cm^2 s^{-1}) [148] [171], v is the kinematic viscosity of the solution (1.009x10^{-2} cm^2 s^{-1} [171]) and ω is the rotation rate of the electrode (in rpm).

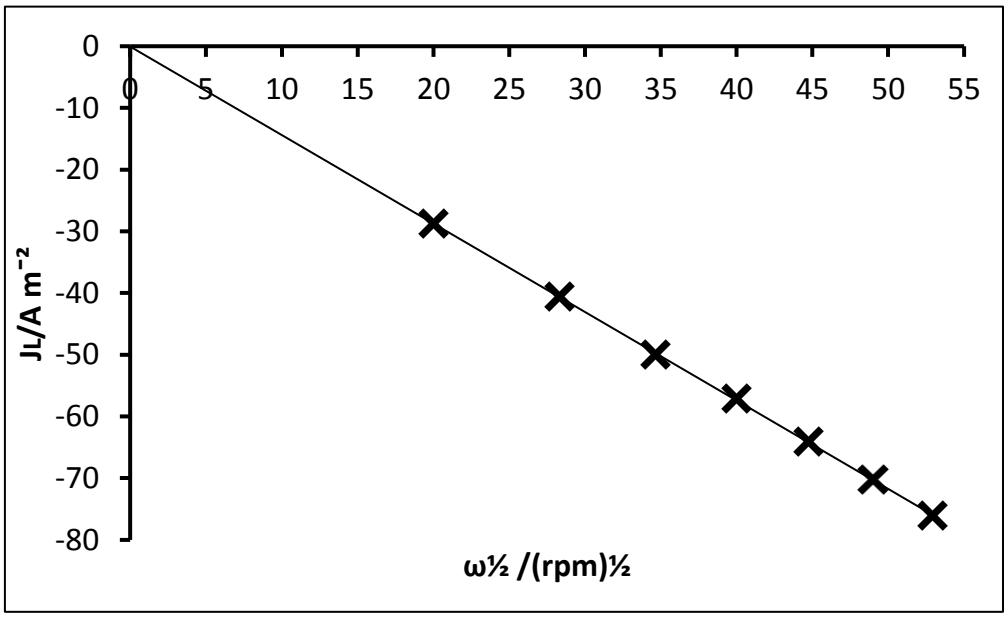

Figure 4-10 *Levich plot for Pt disc*

A plot of J_L against $\omega^{1/2}$, for the Pt disc is shown in Figure 4.10. As predicted by equation 4.21, the graph shows a linear relationship between J_L and $\omega^{1/2}$. The

gradient of this graph can be used to calculate the number of electrons transferred per mole of O_2 (n). The values of *C,D* and *v* (above) are commonly accepted and used by other workers in the field, when these were used, the number of electrons transferred per mole of O_2 was calculated to be 3.8.

There is some uncertainty about the oxygen concentration, other values are given in the literature (Table 4.1). The accuracy of the value measured using the Clark cell was not thought to be high enough. Use of lower values for *C* lead to higher values for n.

Table 4-1 *Accepted values for parameters in the Levich equation*

Parameter	**Value**	**Source**
***C*(O$_2$)**	1.26 x10^{-6} mol cm^{-3}	Watanabe[148] Markovic [171] (Henry's Law)
***C*(O$_2$)**	1.1 x10^{-6} mol cm^{-3}	van Stroe-Blezen[172], Hitchman [173]
***D* (O$_2$)**	1.93 x10^{-5} cm^2 s^{-1}	Watanabe[148] Markovic [171] (Stokes–Einstein eq.)
ν	1.009 x10^{-2} cm^2 s^{-1}	Markovic[171], CRC Handbook of Chemistry and Physics,1986

Equation (4.20) can be rearranged to give

$$J_{\mathrm{K}} = \frac{J_{\mathrm{K}} J}{J_{\mathrm{L}} - J} \qquad (4.22)$$

RRDE results for the oxygen reduction reaction (ORR) on Pt are shown in Figure 4.7 These results can be analysed in two ways. The first is called the Koutecky-Levich analysis. Several potentials in the mixed kinetic/diffusion region (the steeper part of each curve) are chosen. A plot of J^{-1} against $\omega^{-1/2}$ gives an intercept at

$\omega^{1/2}$ =0 which corresponds to, J_K, the kinetic current density, at an infinite mass transport rate. Koutecky-Levich plots ($1/J$ *vs* $\omega^{-1/2}$) are presented in Figure 4.11. The plots are linear, as predicted by equations (4.20) and (4.21).

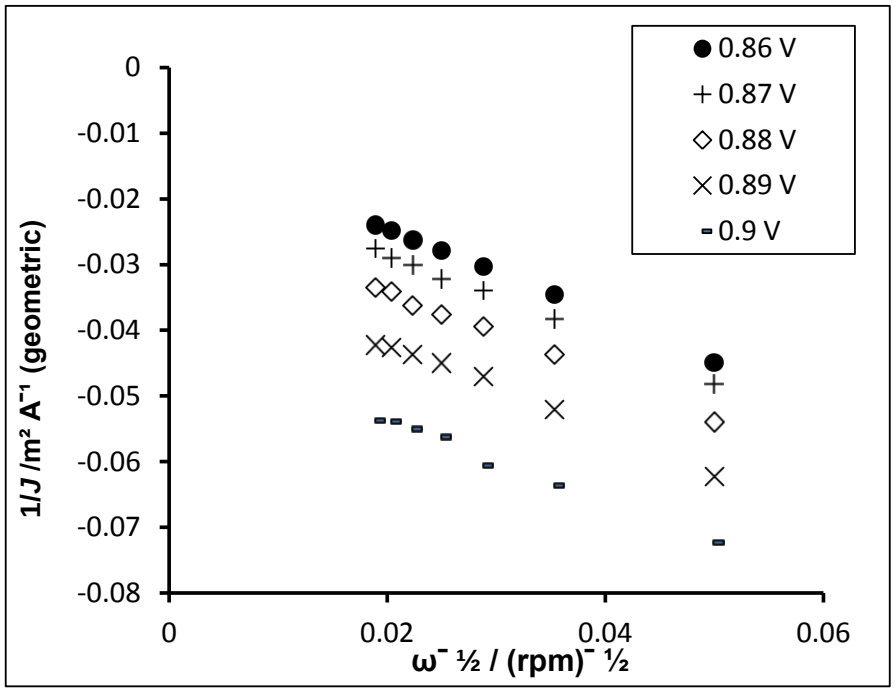

Figure 4-11 *Koutecky-Levich plots calculated from data in Figure 4.7*

LogJ_K is then plotted against potential to create a Tafel plot. Alternatively, one rotation speed e.g. 1600 rpm is chosen and J_K can be calculated from equation 4.22. This method can be more accurate because it does not rely on extensive extrapolation which can introduce errors.

The kinetic currents for the mixed kinetic-diffusion control of the ORR were determined from the Koutecky-Levich plots and used to construct Tafel plots, presented in Figure 4.12a. Kinetic currents were also extracted from the ORR disc

currents at 1600 rpm using equation 4.22 and used to construct the Tafel plots, shown in Figure 4.12b.

The plots in Figures 4.12 a) and b) are normalized with respect to ECSA and show good agreement with one another. From the curvature of the Tafel plots it is clear that there is no single Tafel slope for the reaction in the potential range 0.9-0.78 V. The slope is around –60 mV dec^{-1}, at $E > 0.85$ V, but doubles to –120 mV dec^{-1}, for $E < 0.8$ V. This finding is in good agreement with previous work [174, 175]. The change in slope has been attributed either to a change from Temkin to Langmuir adsorption of reaction intermediates or to an increase in coverage by surface oxides [151].

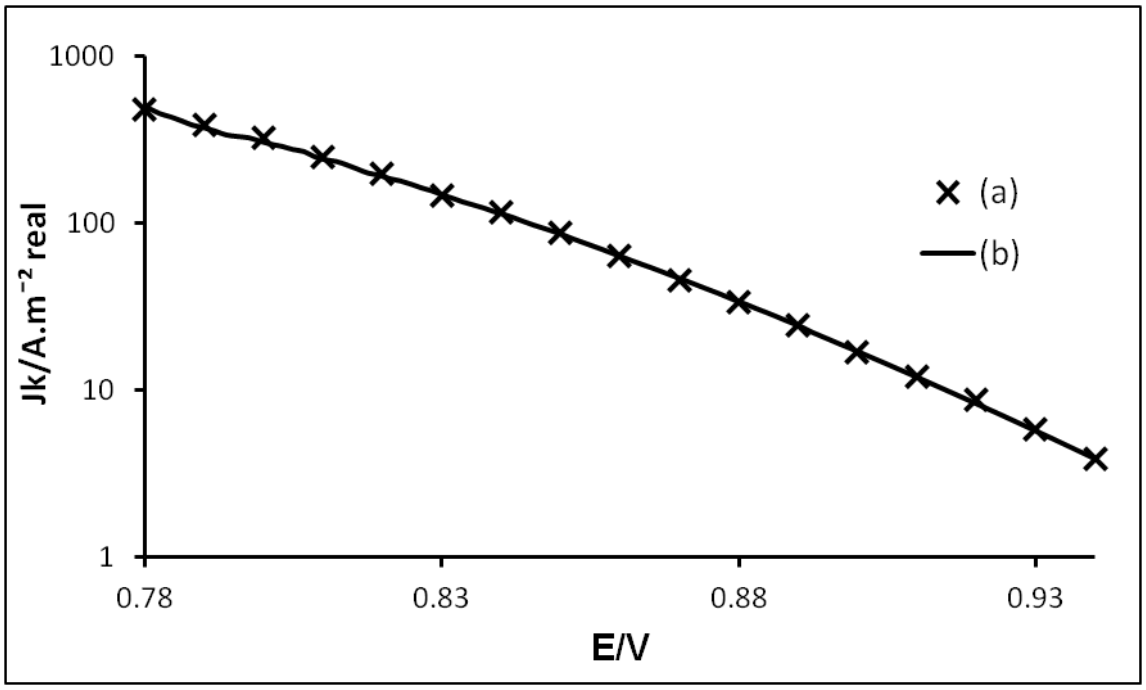

Figure 4-12 *Mass transport corrected current densities for the ORR on a 0.196 cm^2 Pt disc obtained from positive sweeps (25 mV s^{-1}, in 0.1 M $HClO_4$ saturated with O_2 at 25 °C. a) surface area specific current densities (calculated from KL*

4.4 Conclusion

The data obtained for here for Pt disc agree well with theoretical predictions and previous work. Great care is required to achieve reproducible results for the ORR on the Pt disc. The results presented here for the Pt disc were repeated at least ten times and were found to be highly reproducible, with variation of less than 2 % for ORR limiting currents. Cleanliness of glassware was of utmost importance.

Chapter 5 Thin Film RRDE Experiments on Catalyst Inks

In this chapter the electrochemical performance of two types of catalyst nanoparticles is reported and compared with the commercial catalyst TKK (TEC10E50E, 45.9 wt % Pt). Rotating ring disc experimental methods, reported and validated in the previous chapter were used. The nanoparticles tested were JN 42, for clarity now labelled Pt+TTAB and JN 47, now labelled Pt+NP9. These were chosen because the preparation procedures were found to be reliable and reproducible. The TKK catalyst was chosen because at the start of this work it was generally accepted [159, 176] to be one of the most active Pt/C catalysts available. As far as possible the practical procedure described by Garsany [146] was followed for the electrochemical evaluations in this work.

The evaluation of electrocatalytic activity of high surface area catalysts using thin-film rotating disc electrode (RDE) measurements has been reported by Schmidt [158] and developed by others [146, 159, 176]. The studies show that a three-electrode electrochemical cell, as described in chapter 4, can be used to predict performance trends of catalysts in membrane electrode assemblies of PEMFCs. The method uses less catalyst than would be required for single cell MEA testing and is not limited by the problems of mass-transport resistance and incomplete wetting of the electrode structure. Using the RDE technique it is possible to gain a more detailed understanding of the factors affecting catalytic activity.

Briefly, a thin film of catalyst was prepared on a glassy carbon RDE. CVs of the catalysts in an O_2-free electrolyte were used to measure the Pt electrochemical surface area. Thin-film RDE measurements of the ORR in O_2-saturated electrolyte were performed at different rotation speeds. Kinetic currents were calculated from the data and Tafel plots constructed which were normalized to the mass of Pt on the electrode and the Pt electrochemical surface area. Mayrhofer et al. [66] reported on methods to analyse CV and RDE data to determine whether the data are viable. In thin-film RDE measurements of high surface area catalysts it is important to use the appropriate catalyst loading. Mayrhofer et al. [66] reported that three criteria should be met. 'First, the theoretical diffusion limited current density has to be obtained, secondly the normalized catalytic activity has to be independent of the catalyst loading, and thirdly the catalytic activity should be calculated at currents approximately half that of the diffusion limited current, which should be determined at a relevant potential, i.e., 0.9 V or 0.85 V for the oxygen reduction.' The first requirement is due to the fact that the theory developed for the RDE assumes a flat disc centred on the axis of rotation. In thin-film RDE measurements it is therefore important that the active material uniformly covers the glassy carbon disc, otherwise the behaviour may depend on the distribution of the catalyst on the electrode, making mathematical treatment impossible. As a guideline, they suggested that 'the diffusion limited current obtained in an experiment should be within 10 % of the theoretical value'.

5.1 Preparation of Catalyst Inks

PEMFC electrodes consist of Pt catalyst nanoparticles deposited on larger carbon particles, as shown in Figure 1.1. The carbon support provides electrical conductivity and a porous structure for the electrode, so that water and gases can diffuse through the pores. The active catalyst particles should be evenly dispersed over the carbon support. It is common practice to evaluate new nanoparticle catalysts on a carbon support. This is done by first preparing an ink containing the Pt nanoparticles, carbon black and Nafion®. Nafion® is added to provide adhesion to the electrode and in the PEMFC it provides proton conductivity.

The particles should be well dispersed so that an even film can be produced. In this work Milli-Q water was used as the dispersion medium to minimise introduction of impurities. The method closely matched that of Garsany [146]. The nanoparticle dispersions were used after 2x centrifugation, as described in section 3.4.1. No further attempt was made to remove excess surfactant.

5.1.1 Thermogravimetric Analysis

Well-defined Pt and surfactant loadings were required for the preparation of catalyst inks. TGA involves the measurement of mass change of a sample due to thermal oxidation or decomposition as it is heated. A predetermined temperature programme is used. Known volumes of Pt nanoparticle dispersion (prepared as described in Chapter 3) were added to aluminium oxide crucibles and weighed,

then dried in a vacuum oven overnight at 40 ºC, -900 mbar g. After drying the crucibles were reweighed to determine the solid content of the dispersion. This will consist of surfactant and platinum. During thermogravimetric analysis the surfactant is oxidised leaving the platinum. The crucible is weighed, allowing calculation of both the surfactant and platinum content of the dispersion.

Results

Figure 5.1 shows the thermogravimetric mass loss profiles for the Pt nanoparticle dispersions. The Pt and surfactant contents, calculated from the data, are shown in Table 5.1. The initial dispersions, on preparation, contained about 50 mg/mL surfactant and > 0.5 mg/mL Pt. The two centrifuge steps increase the Pt concentration because excess water is removed. Most of the surfactant is removed with the excess water but it is clear from Table 5.1 that the 'clean' dispersions still contain a significant amount of surfactant.

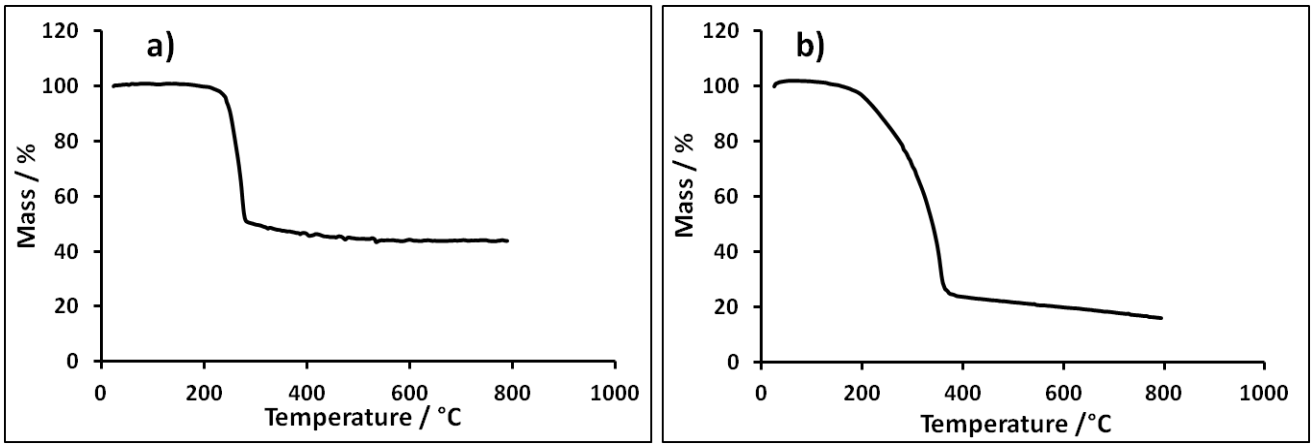

Figure 5-1 *Thermogravimetric mass loss profiles obtained in air with a 50 K min^{-1} thermal ramp: a) Pt+TTAB, b) Pt+NP9.*

Table 5-1 *Pt and surfactant concentrations in dispersions determined from dry weight analysis and TGA*

	Concentration Pt /mg mL^{-1}	Concentration surfactant /mg mL^{-1}
Pt+TTAB	3.85	4.93
Pt+NP9	2.54	8.64

5.1.2 Ink Preparation Method

Vulcan XC-72R carbon black (Fuel Cell Store) was dispersed in Milli-Q water at a concentration of 2 mg mL^{-1}. Nafion® (10% dispersion) was added to give a weight ratio of Nafion®:Carbon black of 1:2.4 in the dry catalyst layer. The mixture was sonicated in an ultrasonic bath for 30 minutes to produce a uniform, stable dispersion free from coarse agglomerates. The Pt and surfactant content of the purified colloidal Pt was determined by TGA as described in the previous section. A measured amount of purified colloidal Pt was added to the Vulcan XC-72R dispersion to give a ratio of 45.9 % Pt on C and sonicated for a futher 30 minutes. The electrochemical activity of the surfactant stabilized Pt/C was compared with the commercial catalyst TKK. The TKK catalyst ink was prepared using a standard method by mixing TKK (45.9 wt. % Pt) commercial catalyst with a quantity of Nafion® dispersion required to form a weight ratio of Nafion®:Carbon black of 1:2.4 in the dry catalyst layer.

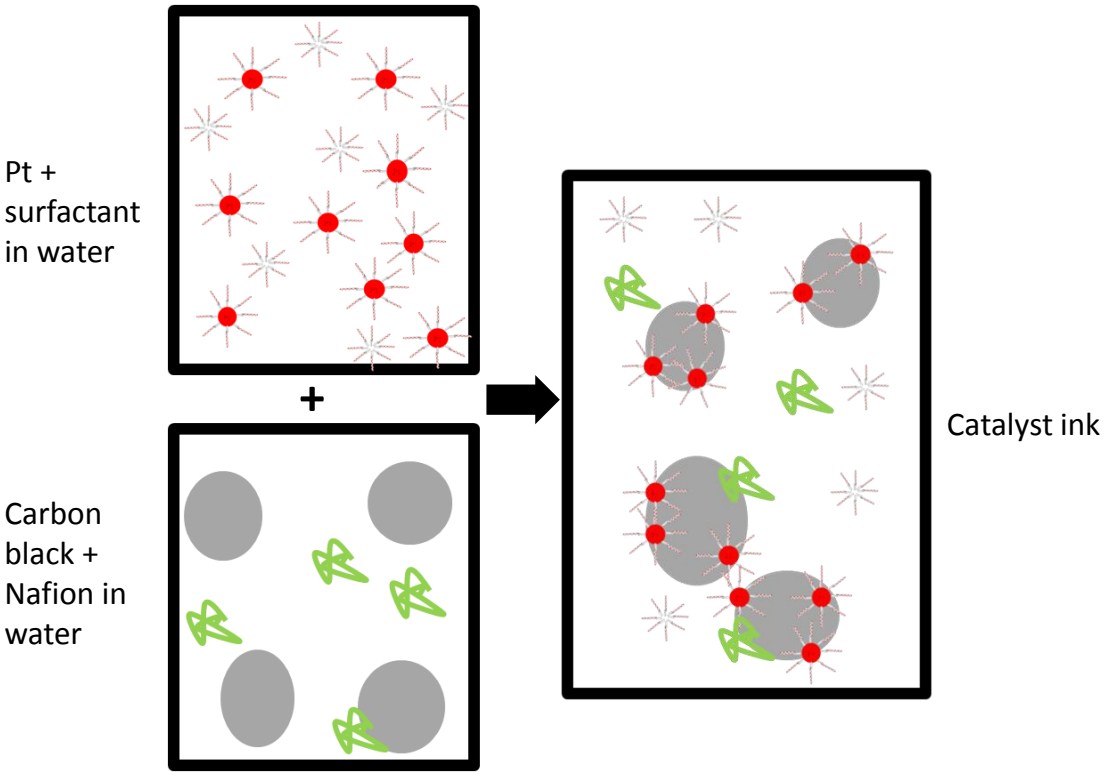

Figure 5-2 *Schematic diagram showing preparation of catalyst ink*

5.2 Transmission Electron Microscopy on catalyst inks

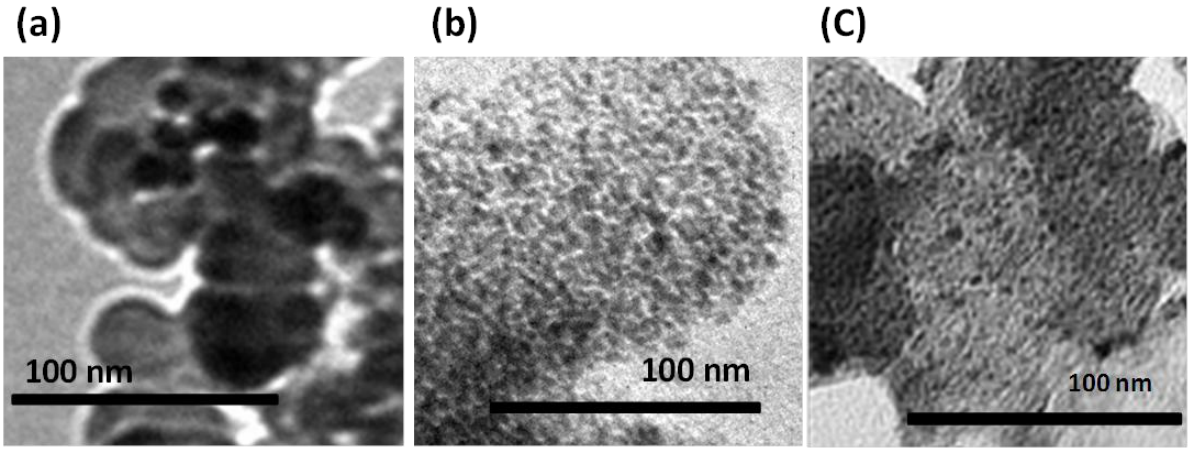

Figure 5-3 *TEM images of carbon supported Pt nanoparticles (a) (Pt+TTAB/C)(JN42C) (b) (Pt+ NP9/C)(JN47C) (c) TKK commercial catalyst.*

.

Figure 5.3 shows representative TEM images of the catalysts loaded on carbon black (Vulcan XC-72). The nanoparticles synthesized with TTAB and NP9 are compared to the commercial catalyst TKK. The Pt+NP9 catalyst has Pt particles of similar size to the TKK catalyst (2.8 nm). Both images show Pt nanoparticles evenly dispersed over the carbon support. The Pt+TTAB particles are larger >10 nm and are not as evenly dispersed over the carbon support.

5.3 Preparation of Working Electrodes

Rotating ring disc electrodes (RRDE) with removable 5 mm diameter glassy carbon enclosed in PTFE with Pt ring were purchased from Pine Instruments (USA). The glassy carbon disc and Pt ring electrodes were polished separately, on Microcloth™ (Buehler) using 1 µm, 0.3 µm and 0.05 µm alumina slurries in sequence. The polished electrodes were rinsed well with Milli-Q water and then sonicated (40 kHz

bath) for 1 minute in Milli-Q water to remove any residual alumina before assembling the RRDE.

For electrochemical characterisation, working electrodes were prepared by pipetting an 11.5 µL aliquot of Pt/C catalyst dispersion onto a 5 mm glassy carbon disc electrode to achieve a Pt loading of 20 µg cm^{-2} and dried at room temperature overnight.

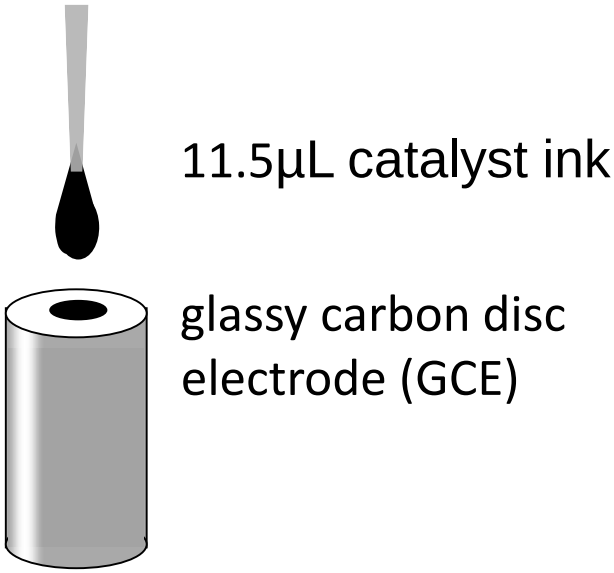

Figure 5-4 *Schematic diagram showing preparation of electrodes*

In the experiments designed to determine optimal loading a known volume of catalyst ink was deposited on the glassy carbon (GC) disc to produce a Pt loading between 20 – 100 µg Pt cm^{-2} as required, and dried at room temperature.

5.4 Cyclic Voltammetry Results

Figure 5.5a shows the cyclic voltammograms (CVs) of three platinum nanoparticle films (Pt+TTAB/C, Pt+NP9/C and TKK) compared with that of the 5 mm Pt disc

electrode. The voltammogram for the TKK catalyst has the characteristic H desorption peaks [177] at 0.14 and 0.21 V, along with the corresponding cathodic adsorption peaks. These peaks are similar those at 0.12 and 0.22 V for the Pt disc, except that the peak at 0.22 for the Pt disc is broader and extends to 0.3 V. The peak at 0.12 V is thought to result from hydrogen underpotential deposition (H_{upd}) on Pt (110) sites, while the peak at 0.22 V corresponds to Pt (100) terraces and high co-ordination edge and corner Pt sites [43, 47, 156-158, 178]. In the Pt+NP9/C electrochemistry they are mostly lost. It is possible that the surfactant molecules may be preferentially adsorbing onto the Pt crystal sites usually responsible for the more distinct H_{upd} features [154, 177]. The other important difference in the voltammetry between the TKK catalyst and Pt+NP9/C films is the greatly reduced magnitude of the peaks for adsorption and desorption of oxygen species on Pt. For the TKK catalyst this peak occurs at ca 60 mV negative compared to that on the polycrystalline Pt disc. These results are in agreement with those of Gasteiger et al. [159], who attribute the negative shift to increased binding strength of OH_{ads} species on the TKK catalyst than on Pt (poly). They comment further that these species have an adverse effect on the O_2-reduction reaction. The corresponding peak for the Pt+NP9/C catalyst is very small but occurs at a similar negative potential to that of the polycrystalline Pt disc, indicating substantially reduced binding of OH_{ads} species on the Pt+NP9/C catalyst. The voltammogram for the Pt+TTAB/C shows almost undetectable peaks for H and OH desorption.

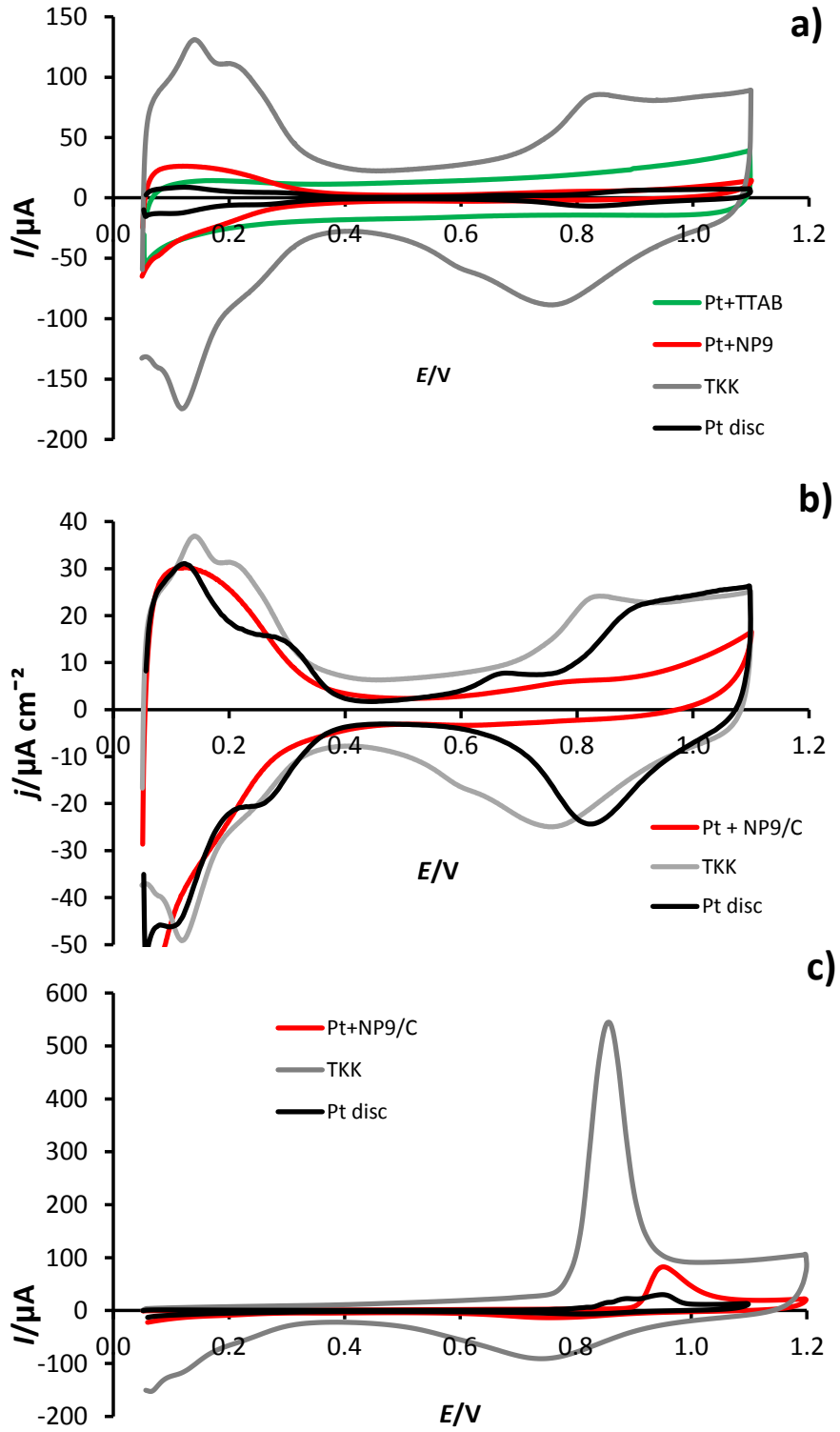

Figure 5-5 *Cyclic voltammograms of Pt/C catalysts 20 µg Pt/cm² geometric on 0.196 cm² GC electrodes in N_2-saturated 0.1 M HClO4 at 25°C. Scan rate 25 mV/s. Compared to that of 0.196 cm² Pt disc electrode, a.)Current (I/A) Vs voltage, b) Pt-surface area normalized current densities (J/(mA cm^{-2}) vs voltage, c) CO stripping voltammogram*

5.4.1 Electrochemical Surface Area (ECSA) Measurements

Electrochemical surface areas for catalyst thin films were measured using the H_{upd} method as described in chapter 5. For the thin-film catalyst layers on GC electrodes with Pt loading 20 µg cm^{-2}, the total electrochemically-active surface area was typically 10-20 times higher than the geometric area of the electrode. A typical CV for TKK catalyst is shown in Figure 5.6.

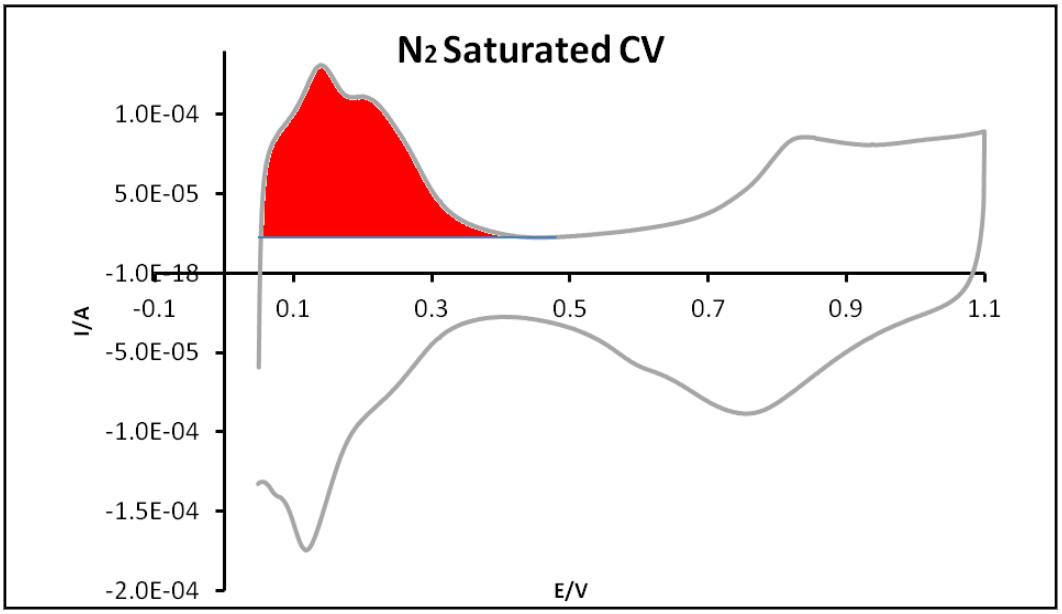

Figure 5-6 *Cyclic voltammogram of TKK catalyst 20 µg Pt/cm² geometric on 0.196 cm^2 GC electrodes in N_2-saturated 0.1 M $HClO_4$ at 25 ºC. Scan rate 25 mV/s. Showing shaded region due to H_{upd} desorption.*

A baseline was set to correct for capacitive current as shown in Figure 5.6. ECSAs for the films were measured by integrating the desorption waves for underpotentially deposited hydrogen and assuming a charge passed per unit area of Pt of 210 µC cm^{-2} [159]. These values are given in Table 5.2, along with an estimate of the theoretical area obtained from the loading used, assuming spherical particles of the mean diameter measured from TEM results. The ECSA mesasured

for the TKK catalyst compares well with previously reported values of *ca.* 90 m^2 g^{-1} [176]. The Pt+NP9/C particles have an electrochemical surface area that is < 25 % of that for the TKK catalyst, despite equal platinum loadings and particle sizes, suggesting that the NP9 blocks 75 % of the surface Pt atoms to H adsorption. The shape of the CV in the H_{upd} region suggests that the NP9 surfactant is adsorbing on edge and corner sites. Calculations [53] suggest that 2.5 nm nanoparticles consist of approximately 75% edge and corner sites and 20 % Pt (111). The Pt loading is the same in both cases and mean particle size is 2.8 nm. In Figure 5.5 b) the CVs are normalised for electrochemical surface area which highlights the suppression of Pt oxide formation and reduction on Pt+NP9/C. The CV for the Pt+TTAB/C nanoparticles shows very small H desorption and adsorption peaks and so the error in measurement is large.

The CO-stripping curves shown in Figure 5.5 c) were recorded in CO-free solution after adsorbing CO at 0.05 V for 30 minutes in CO saturated solution. The total voltammetric charge was calculated from the background corrected area under the CO stripping peak [66, 179, 180]. The charge calculated for Pt+NP9/C is < 20 % that for the TKK catalyst. This is in agreement with the H adsorption results, suggesting that the NP9 surfactant is blocking 80% of the Pt sites. The CO oxidation peak for Pt+NP9/C occurs at 0.95 V, compared with 0.85 V for the TKK catalyst. This is likely to result from the low coverage of OH_{ads}, on Pt+NP9/C, which is required for CO oxidation [181].

5.5 Determination of Optimum Catalyst Loading on RDE

It is important to use the correct Pt loading in RDE experiments [66]. If the catalyst loading is too high, and catalyst films are thicker than 0.1 μm, the mass-transport characteristics of the RDE are no longer satisfied [182, 183]. Factors, such as agglomerate structure, particle contact and diffusion properties of oxygen in the ionomer film start to influence specific activity. Also, the net activity becomes so high that the kinetic region becomes very small, and the polarization curve very steep, leading to the problems with precision of the potential reading. If the catalyst loading is too low the supported catalyst cannot spread completely over the surface of the glassy carbon electrode. The optimum loading depends on the dispersion of each catalyst and may differ considerably. Therefore, it has to be determined for each catalyst individually.

Figure 5.7 shows the effect of the RDE Pt loading of Pt+NP9/C (JN47) on ECSA (a) and diffusion limiting current (b). The ECSA reaches a maximum at about 17 $\mu g/cm^2$ The diffusion limiting current begins to level out at 20 $\mu g/cm^2$. The loading of 20 $\mu g /cm^2$ was taken as the optimum loading, for which the catalyst is spread completely over the surface of the glassy carbon support and the film is not too thick. This loading had previously [184] been reported as the optimum loading for TKK catalyst.

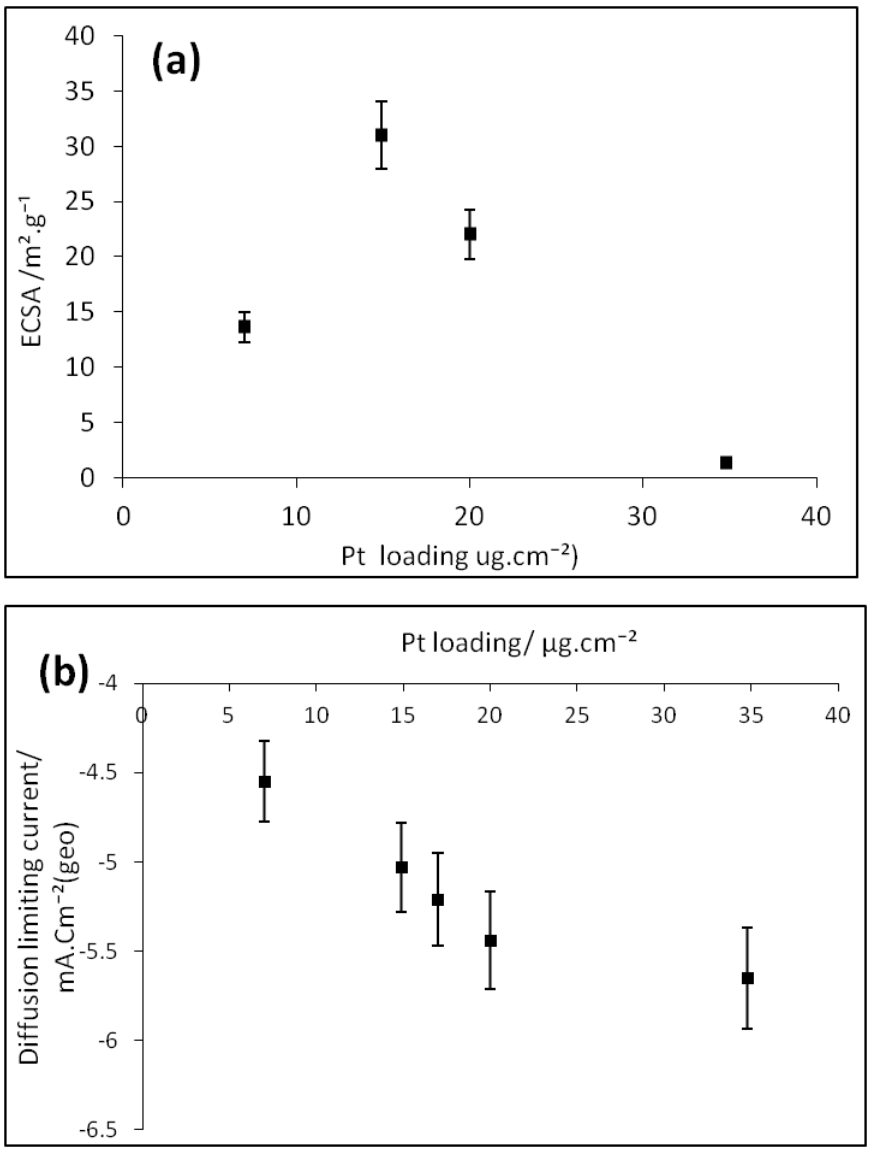

Figure 5-7 *The effect of Pt loading for Pt+NP9/C (JN47C); (a) on ECSA , (b) on diffusion limiting current.*

5.5 ORR Results

Figure 5.8 compares the ORR RRDE data of Pt+NP9/C, Pt+TTAB/C, TKK catalyst and the Pt disc. Panel (a) shows the ring current and panel (b) shows the disc current at various electrode rotation rates.

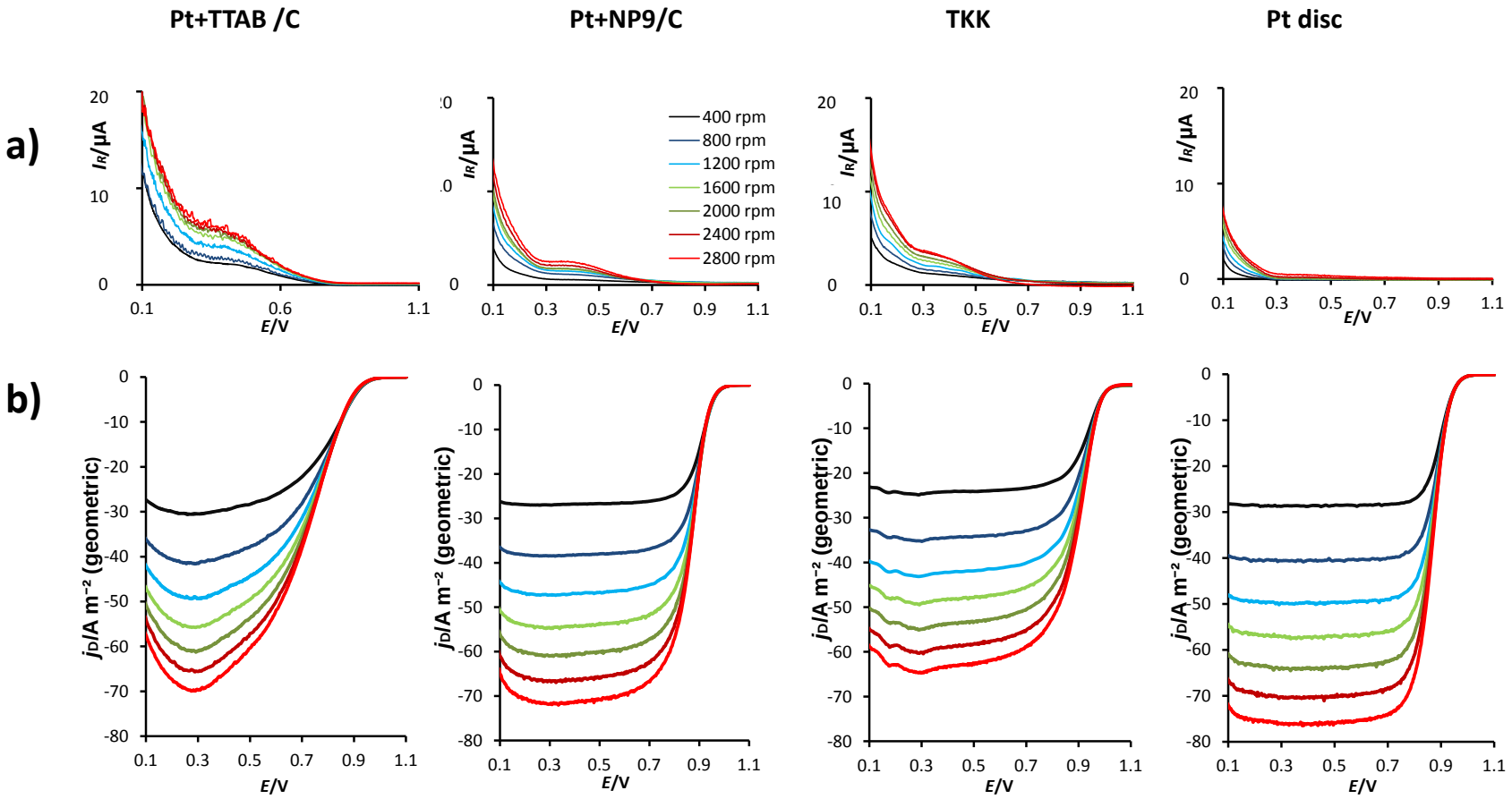

Figure 5-8 *iR-corrected, background-subtracted RRDE data at various rotation rates; for Pt/C catalysts 20 µg Pt/cm² geometric on 0.196 cm² GC electrodes in O_2-saturated 0.1 M HClO4 at 25 ºC. a) Ring current (ring potential held at 1.1 V), b) disc current. (left) Pt +TTAB/C, (centre) Pt +NP9/C TKK, (centre) TKK, (right) Pt disc*

The ORR polarization curves, in Figure 5,8 each show a single reduction wave at each rotation speed and limiting current density plateaux are observed for all samples except for the Pt+TTAB/C electrode, whose shape is indicative of slow kinetics coupled with complex adsorption/desorption processes; the shape is similar to that found when bromide is adsorbed on Pt [185]. The catalyst activity toward the ORR can be visually benchmarked from the polarization curves: the more positive the onset of current or the half wave potential, the more active the catalyst. The half-wave potentials (taken from the curves measured at 1600 rpm) of the Pt+NP9/C, TKK catalyst and Pt disc electrodes are 0.88 ± 0.02 V, whereas that of the Pt+TTAB/C electrode is more negative, at 0.74 V.

Figure 5.9a presents plots of *n*, the number of electons transferred (equation 4.18) as a function of potential, calculated from the RRDE data acquired at 1600 rpm for each catalyst. Figure 5.9 a shows that *n* is close to 4 for each catalyst at potentials positive of ca +0.3 V, indicating that water is the main product of the ORR. It is also evident that the Pt+TTAB/C catalyst is least selective toward the 4-electron reduction to water, across the whole potential range studied. The selectivity of the reaction can also be represented by the fraction of H_2O_2 ($X_{H_2O_2}$), equation (4.19). Values of $X_{H_2O_2}$ are plotted as a function of potential in Figure 5.9b. For each electrode, a significant increase in $X_{H_2O_2}$ is observed in the H_{upd} region (E < 0.2 V). This observation has previously been attributed to competitive adsorption of hydrogen, which results in blocking of active sites, hindering the dissociative adsorption of oxygen molecules[171].

The values obtained for the TKK and NP9 catalysts are in good agreement with the work of Inaba et al. [142], who found that for similar catalyst loadings, $X_{H_2O_2}$ drops from 0.18 at +0.1 V to values less than 0.05 at voltages more positive than 0.4 V. Previous studies have shown that the fraction of H_2O_2 production in the H_{upd} region is higher for Pt particles supported on carbon [142] and for Pt surfaces in contact with a layer of adsorbed Nafion® [143, 186]. The fraction of H_2O_2 has also been shown to be dependent on the Pt particle size and the Pt/C ratio [186]. Figure 5.9 shows that negative of +0.3 V, the extent of peroxide formation is significantly higher on the Pt+NP9/C and TKK catalysts than on the Pt disc. The tendency towards the 2-electron pathway may arise from a combination of particle size effects and modifications to the Pt surface by adsorbed Nafion®. The amount of peroxide production is negligible over the range of typical operating potentials of the PEMFC cathode (+0.6V to +1.0 V). The large excess of NP9 surfactant, present in the Pt+NP9/C catalyst, did not significantly affect the proportion of H_2O_2 produced. The reason for this could be that the NP9 surfactant adsorbs preferentially on edge and corner sites of the nanoparticles which tend to be blocked by OH_{ads} in the potential range of interest. Terrace sites may be left free of surfactant allowing O_2 adsorption and reduction to occur without the mechanism being affected.

The amount of hydrogen peroxide produced is significantly higher on the Pt+TTAB/C catalysts, which is likely to result from blocking of sites by bromide counterions from the TTAB surfactant. Bromide ions adsorbed on Pt are known to increase H_2O_2 oxidation currents on the ring electrode, implying that in the

presence of bromide ions the ORR does not proceed entirely through the 4-electron pathway [59]. This has been attributed to site blocking, such that pairs of adjacent Pt sites, required for the splitting of the O-O bond, are less abundant.

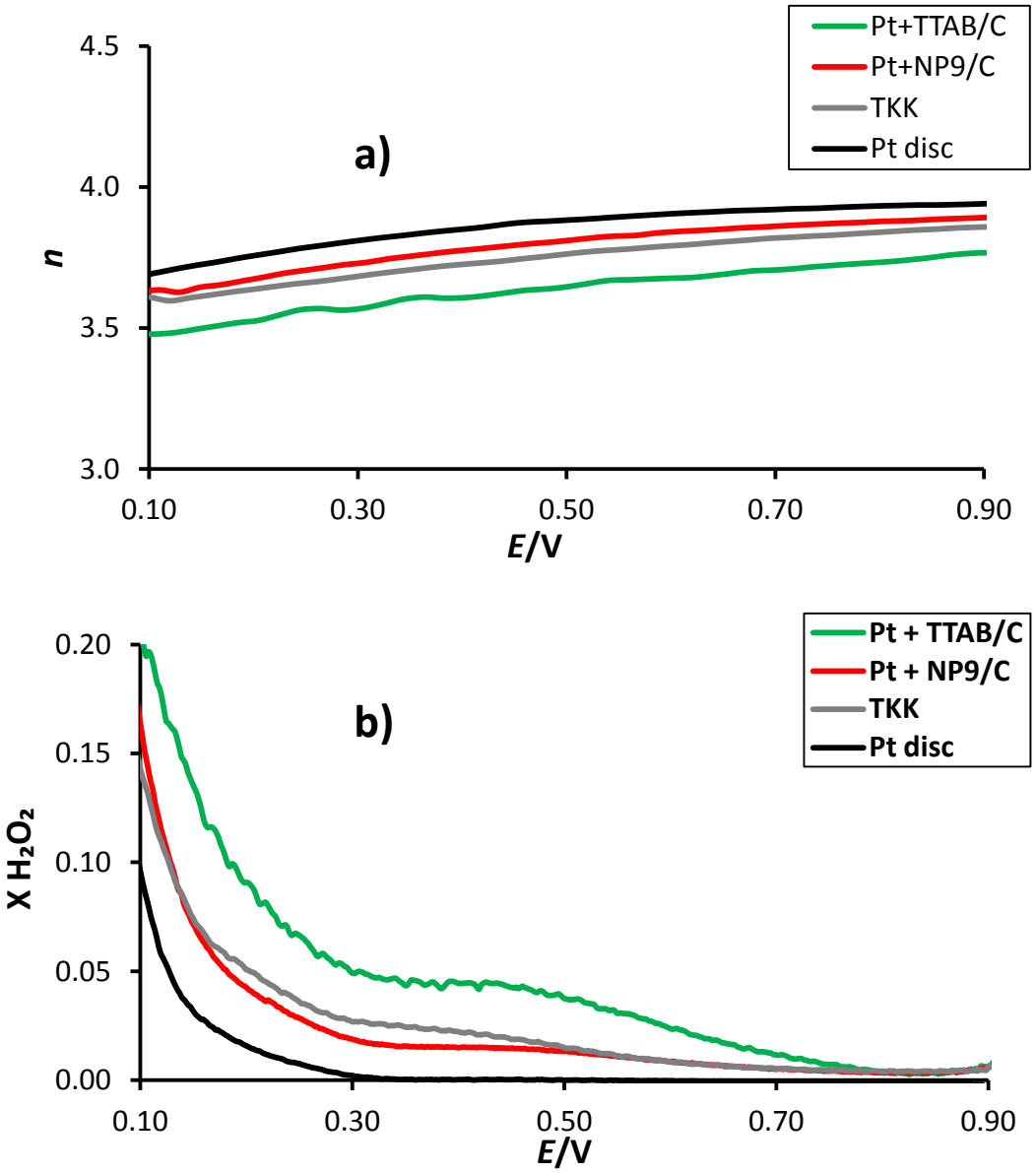

Figure 5-9 *a) n as a function of potential, calculated from the RRDE data acquired at 1600 rpm for each catalyst, using equation 4.18, b) Fraction of H_2O_2 formation during O_2 reduction on Pt+NP9/C, TKK and Pt disc and Pt+TTAB/C at 25°C in 0.1 M $HClO_4$ saturated with O_2. Calculated from the data in Figure 5.8 (at 1600 rpm) using equation 4.19 with N = 0.21*

Kinetics of the ORR

It is of interest to evaluate the kinetics of the overall reaction, from the point of view of performance of the fuel cell. The kinetic currents for the mixed kinetic-diffusion control of the ORR were determined from the Koutecky-Levich plots (Figure 5.10) and used to construct Tafel plots, presented in Figure 5.11a. Kinetic currents were also extracted from the ORR disc currents at 1600 rpm using the rearrangement of the Koutecky-Levich equation 4.22 and used to construct mass transfer-corrected Tafel plots, shown in Figure 5.11b. The data for Pt+TTAB/C are not plotted because of the large error in calculation of the ECSA.

The plots in Figures 5.11a and b are normalized with respect to ECSA and show good agreement with one another. From the curvature of the Tafel plots it is clear that there is no single Tafel slope for the reaction in the potential range 0.9 – 0.78 V. The slope is around –60 mV dec^{-1} at $E > 0.85$ V but doubles to –120 mV dec^{-1} for $E < 0.8$ V. This finding is in good agreement with previous work [174, 175], who found similar shape Tafel plot . The change in slope has been attributed either to a change from Temkin to Langmuir adsorption of reaction intermediates or to an increase in coverage by surface oxides [151].

The results show that in the kinetically controlled potential region the area specific activity is highest for the Pt disc. This is in agreement with the work of Mayrhofer et al. [62], who found that for the ORR the increase in oxophilicity with smaller particles leads to a decrease in specific activity because OH can

effectively block the active sites required for the adsorption of O_2 and the splitting of the O-O bond. The specific activity of the TKK catalyst at 0.9 V (3.1 A m^{-2}) compares well with values previously reported for this catalyst (2.92 A m^{-2} in the same electrolyte at 25 °C and a sweep rate of 10 mV s^{-1} reported by Takahashi and Kocha [176], 2.9 A m^{-2} in the same electrolyte at 60 °C ,*N.B.* the solubility of oxygen is lower at this temperature, and a sweep rate of 20 mV s^{-1} reported by Gasteiger *et al*. [159] . The area specific activity for Pt+NP9/C is higher than that for the TKK catalyst, which suggests less blocking of active sites with OH species. It appears, from the CV (Figure 5.5b), that the NP9 surfactant inhibits strongly OH adsorption on the Pt surface, which, interestingly, may explain the higher specific activity observed. The results in Figures 5.8 and 5.11 show that the ORR is not completely blocked by the NP9 surfactant molecules.

To allow for comparison with the Pt+TTAB/C catalyst, the kinetic currents obtained using equation (4.22) were also normalized per mass Pt and these data are presented in Figure 5.11c. This quantity is also highly relevant in terms of cost of catalyst required for a fuel cell. The mass activity of the TKK catalyst at 0.9 V (277 A g^{-1}) compares well with literature values (266 A g^{-1} at 25 °C reported by Takahashi and Kocha [176] and 220 A g^{-1} at 60°C ,N.B. the oxygen solubility is lower at this temperature, reported by Gasteiger *et al*. [159]). The mass activity-potential plot in Figure 5.11c shows that the Pt+NP9/C catalyst has similar mass activity to the TKK catalyst, despite the presence of excess NP9 surfactant. The Pt+TTAB/C catalyst shows considerably worse mass activity.

This effect could be caused by several factors. The larger size of the Pt+TTAB/C particles means that they have a smaller surface area per unit mass than the Pt+NP9/C and TKK. Also, the activity will be reduced by the site blocking effect of the bromide counterions in the cationic surfactant; bromide has been shown previously to have a detrimental effect on ORR activity [59, 185]. The Pt+TTAB/C particles are mostly cubic and will mainly have Pt(100) crystal faces, which are known to be less active toward the ORR in perchloric acid solution than Pt(110) and Pt(111) faces [50-52]. It is also possible that the presence of the surfactant inhibits electron transfer between the catalyst and the carbon support, although this effect was not seen for the NP9-stabilized catalysts. It is not possible to separate the effect of bromide ions from that of the organic cation without substantial additional work, so we defer this investigation to a future paper. The similarity of the RDE curves with those published for bromide-containing solutions are strong evidence that bromide is at least partially responsible for the lower activity of the Pt+TTAB/C catalyst.

Values of surface area specific activity (SA) and mass activity (MA) at 0.8 V or 0.9 V are often quoted in the literature [159, 176]. It is not necessarily helpful to compare values as they change rapidly with voltage and so depend on accurate voltage measurement. For ease of comparison the values are shown in Table 5.2.

Table 5-2 *Summary of catalyst properties*

Catalyst	ECSA/ $m^2 g^{-1}$	d/nm	Surface area / $m^2 g^{-1}$ (calculated)	MA/ A g^{-1} @ 0.8 V	MA/ A g^{-1} @ 0.9 V	SA/ A m^{-2} @ 0.8 V	SA /A m^{-2} @ 0.9 V
TKK	91	2.8	98	1239	277	13.9	3.06
TKK [176]	90				266		2.92
Pt+NP9/C	22	2.8	98	1488	139	67.7	6.3
Pt+TTAB/C	1.7	12	23	136	20.8	-	-
Pt disc	(0.28 cm^2)	-	-	-	-	313	17

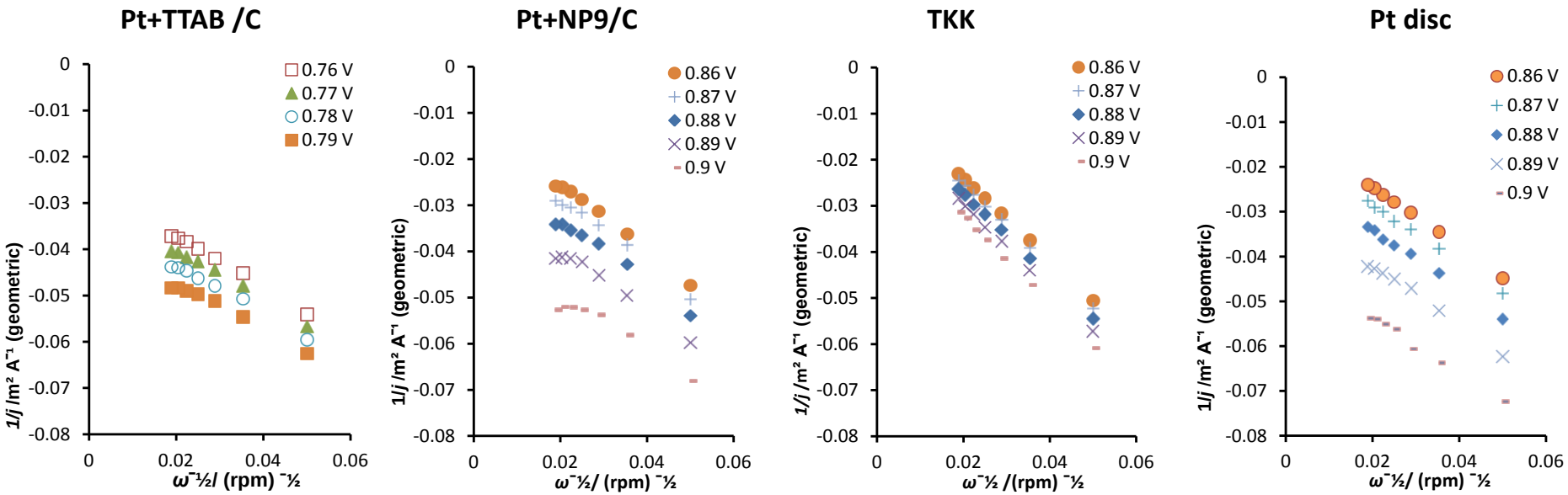

Figure 5-10 *iR-corrected, background-subtracted RRDE data at various rotation rates; for Pt/C catalysts 20 µg Pt/cm² geometric on 0.196 cm² GC electrodes in O_2-saturated 0.1 M $HClO_4$ at 25 ºC.* ***a)*** *Ring current (ring potential held at 1.1 V),* ***b)*** *disc current,* ***c)*** *Koutecky-Levich plots.*
(left) Pt +TTAB/C, (centre) Pt +NP9/C TKK, (centre) TKK, (right) Pt disc

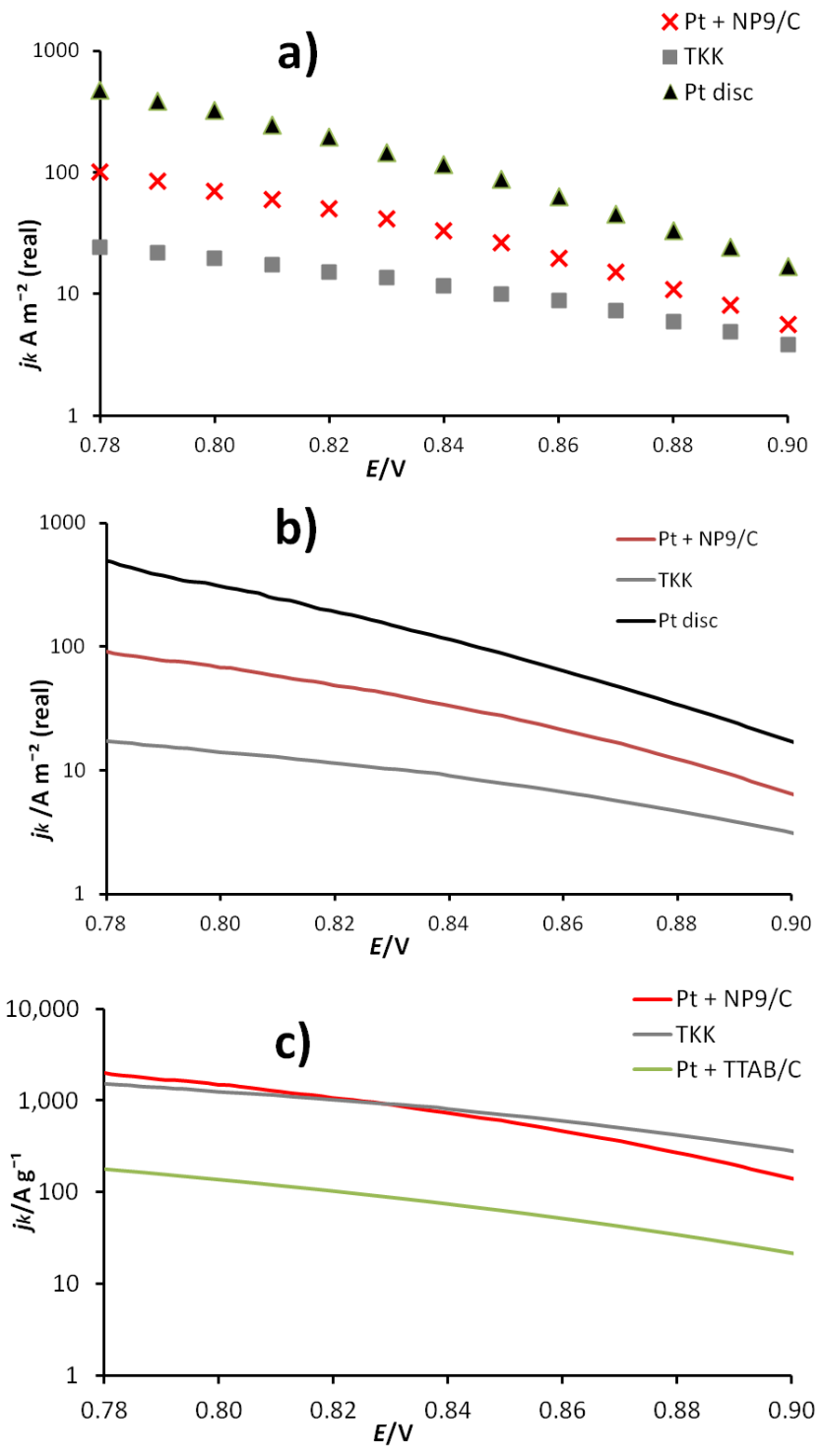

Figure 5-11 *Mass transport corrected current densities for the ORR on a Pt+NP9/C thin-film RRDE and TKK (20 µg Pt cm^2), obtained from positive sweeps (25 mV s$^{-1,}$ 1600 rpm) in 0.1 M $HClO_4$ saturated with O_2 at 25 °C. a) surface area specific current densities (calculated from KL plot), b) surface area specific current densities calculated from results at 1600 rpm),and c) mass-specific current densities.*

A kinetic analysis of the ring and disc currents was employed to provide more detail on the differences in selectivity between the catalysts studied.

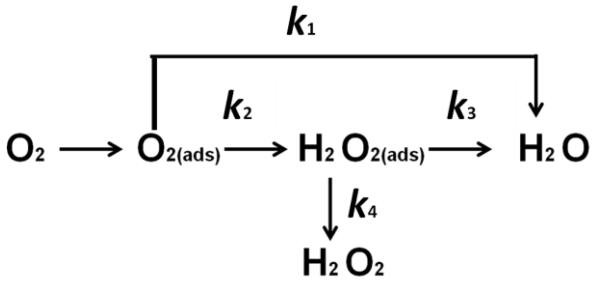

Scheme 1

Using Scheme 1, a comparison of the rate constants k_1 (representing 4-electron reduction to water) and k_2 (representing 2-electron reduction to hydrogen peroxide) can be carried out, if it is assumed that the chemical decomposition and electrochemical oxidation of hydrogen peroxide are minimal and the adsorption and desorption of hydrogen peroxide are rapid and in equilibrium. Diagnostic plots of I_D/I_R vs $\boldsymbol{\omega}^{-1/2}$ and are presented for each catalyst in Figure 5.12. The intercepts of these plots are not equal, which indicates that a parallel reaction pathway operates (in agreement with the conclusions drawn from Figure 5.9). Hsueh and Chin [187] developed the model further to determine the rate constants from the plots in Figure 12 and plots of $I_{DL}/(I_{DL} - I_D)$ vs $\boldsymbol{\omega}^{-1/2}$:

$$\frac{I_D}{I_R} = \frac{1}{N}\left[1 + 2\frac{k_1}{k_2}\right] + \left[\frac{2\left((k_1/k_2)+1\right)}{NZ_2}k_3\right]\omega^{-1/2} \qquad (5.1)$$

$$\frac{I_D}{(I_{DL}-I_D)} = 1 + \frac{k_1+k_2}{Z_1}\omega^{-1/2} \qquad (5.2)$$

where I_{DL} is the limiting disc current, Z_2=0.620$D(H_2O_2)^{2/3}v^{-1/6}$ and Z_1=0.62$D(O_2)^{2/3}v^{-1/6}$. Equation (5.1) corresponds to the plot in Figure 5.12 and plots corresponding to equation (5.2) are given in Figure 5.13. If the slope of a plot in Figure 5.12 is S_1 and the intercept is I_1 and a plot in Figure 5.13 has slope S_2 and intercept 1, equations (5.3) - (5.5) can be used to evaluate the rate constants k_1, k_2 and k_3:

$$k_1 = S_2 Z_1 \frac{I_1 N - 1}{I_1 N + 1} \quad (5.3)$$

$$k_2 = \frac{2 Z_1 S_2}{I_1 N + 1} \quad (5.4)$$

$$k_3 = \frac{Z_2 N S_1}{I_1 N + 1} \quad (5.5)$$

The rate constants are usually normalized for ECSA for comparison of the catalysts investigated. Since the ECSA for the Pt+TTAB/C catalyst is so small and thus the error associated with its calculation so large, we decided to compare instead the ratio of the rate constants k_1 and k_2. Figure 5.14 presents plots of k_1/k_2 as a function of potential for each catalyst studied. The plot indicates a steady fall in the ratio as the potential is made more negative, which reflects the tendency for the fraction of hydrogen peroxide to increase at more negative potentials. Significantly, the ratio is smallest for the Pt+TTAB/C

catalyst, which shows that the rate of production of hydrogen peroxide is highest for this catalyst. This is likely to be a result of a number of factors, particularly blocking of active sites by bromide ions, which reduces the availability of adjacent sites for oxygen to adsorb and so reduces the extent of dissociative adsorption, essential for the full reduction to water. The lower ratio may also be a reflection of different facets exposed: since the Pt+TTAB/C particles are cubic, it is likely that facets are predominantly 100 and 100 single crystals exhibit lower activity than 111 or 110 faces of Pt [47]. Interestingly, the k_1/k_2 ratio is higher for Pt+NP9/C catalysts than for theTKK catalyst. This may be a result of the inhibition of OH adsorption observed in Figure 5.5b.

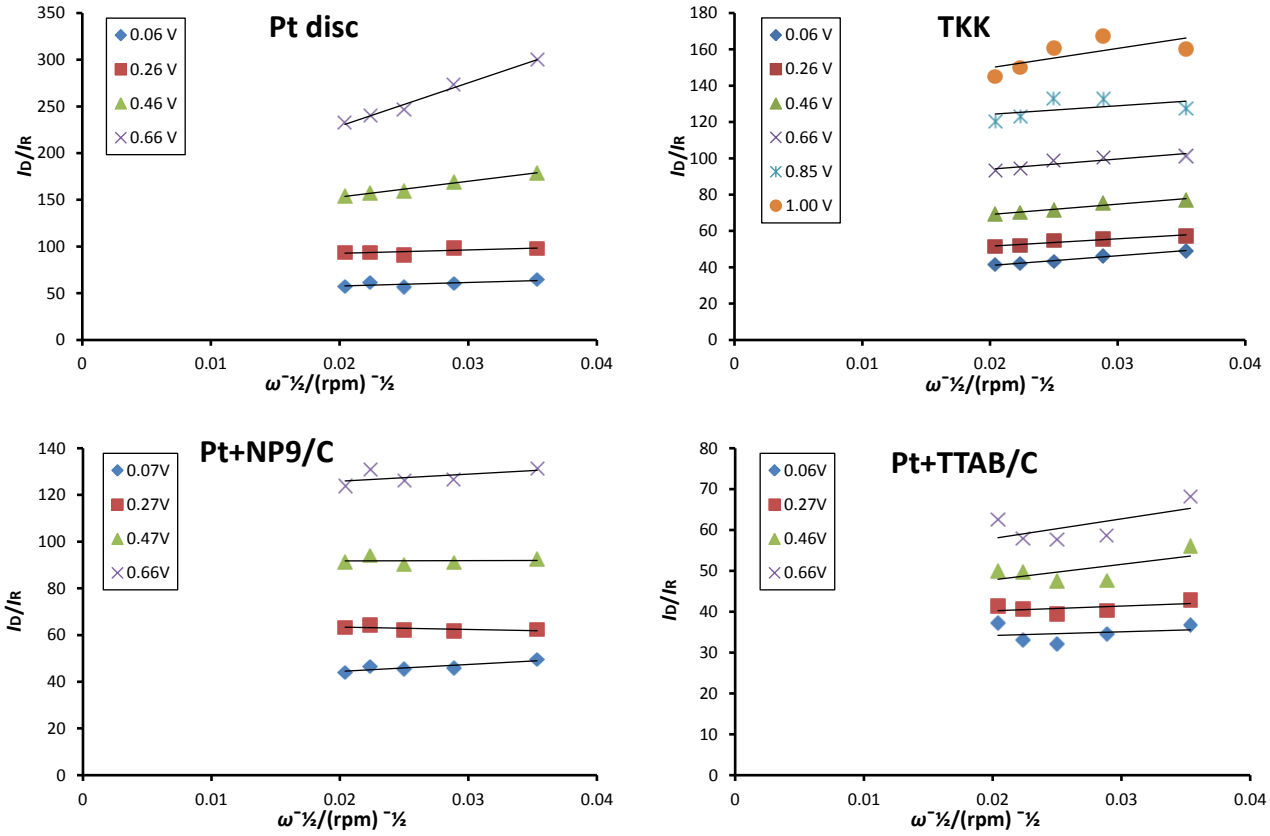

Figure 5-12 plots of I_D/I_R vs $\omega^{-1/2}$calculated from data presented in Figure 5.8

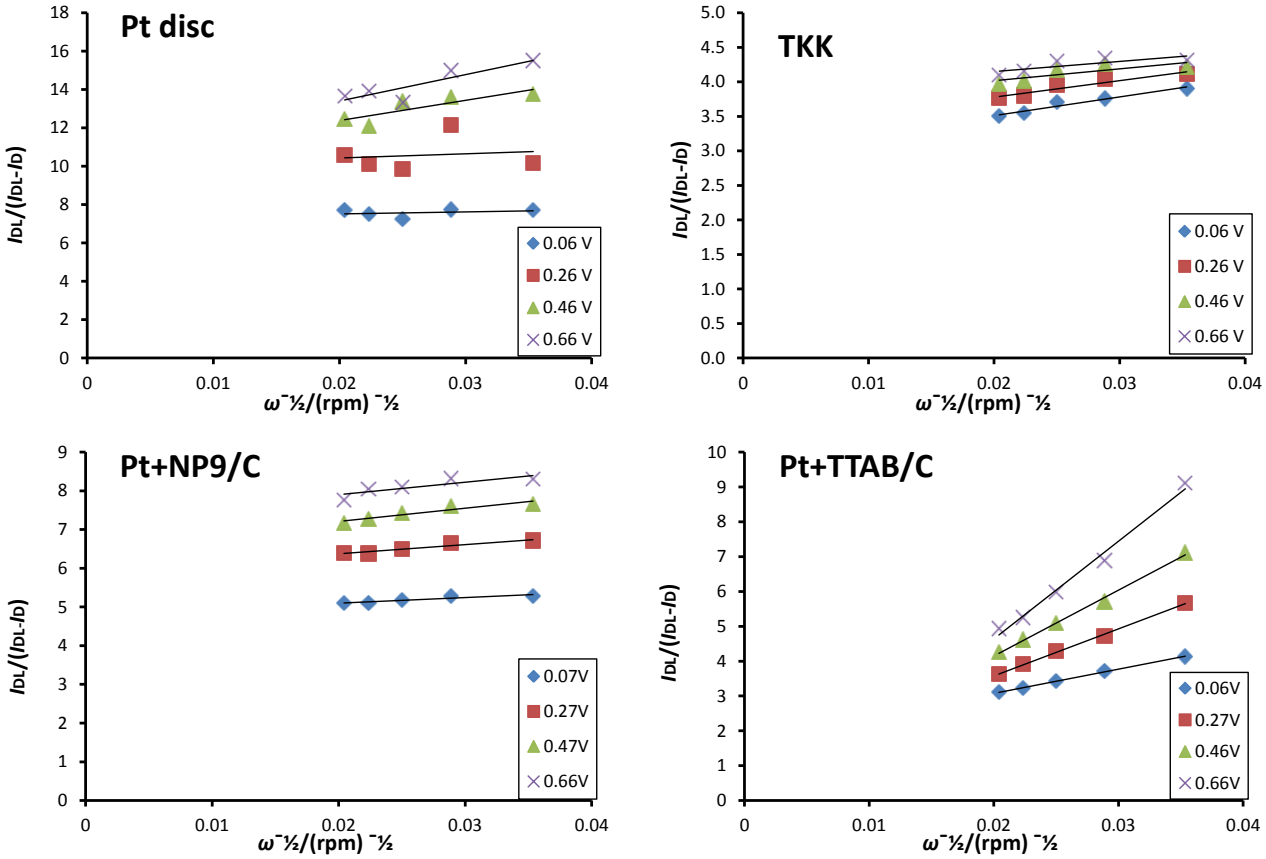

Figure 5-13 plots of $I_{DL}/(I_{DL} - I_D)$ vs $\omega^{-1/2}$ calculated from data presented in Figure 5.8

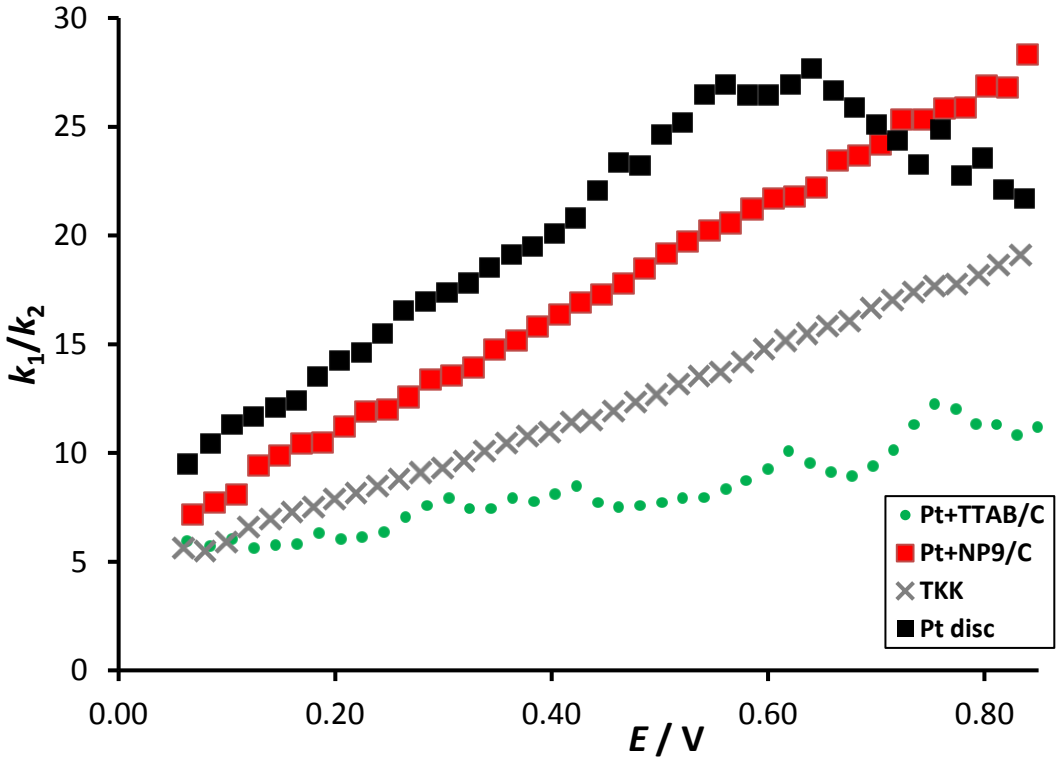

Figure 5-14 *k_1 /k_2 as a function of potential*

5.6 Catalyst Durability

The long-term durability of PEM fuel cell systems is very important especially in applications, such as automotive which demand repeated start/stop cycles. During repeated electrochemical cycling the electrocatalyst particles degrade by the following mechanisms [188], which all cause lowering of catalyst surface area;

1. Pt dissolution, smaller Pt particles dissolve and the Pt precipitates onto larger particles causing particle growth, this is known as Ostwald ripening.
2. Migration of catalyst nanoparticles on the carbon support, leading to aggregation and sintering.

3. Carbon corrosion, the carbon support can oxidise during electrochemical cycling, causing loss of the supported nanoparticles.

   It is possible that the surfactants used to prevent aggregation during nanoparticle synthesis will prevent aggregation during electrochemical cycling, and so improve durability. Ideally, testing of the long-term durability of PEMFC catalysts should be carried out within the PEMFC system, using realistic duty cycles for several thousand hours, followed by ex-situ post-mortem analysis of the catalyst. This is expensive and impractical for screening of new catalysts. In this work an accelerated stress-testing protocol using the rotating-disc electrode was employed [176].

Method

Catalyst thin-film working electrodes were prepared as described in section 5.2. Experiments were conducted in 0.1 M $HClO_4$ at 25 ºC, using the electrochemical set up described in section 5.2. ECSA was measured from cyclic voltammograms recorded at 25 mV s^{-1} in N_2 saturated 0.1 M $HClO_4$, using the H_{upd} method. The ORR performance was measured in O_2 saturated 0.1 M $HClO_4$. The working electrode potential was then cycled between 0.05 and + 1.1 V *vs*. RHE at a scan rate of 250 mV s^{-1}. ECSA measurement was repeated after every 1200 cycles, up to a total of 9600 cycles. The electrolyte solution was then re-saturated with O_2 and the ORR performance measured. The catalysts were benchmarked against Pt/C catalysts TKK (TEC10E50E 45.9 wt. % Pt).

Results

The cyclic voltammograms recorded after repeated electrochemical cycles show reductions in the H_{upd} current with successive cycles, this indicates loss of Pt ECSA. The loss of ECSA with increasing number of cycles is shown for each catalyst in Figure 5.15. The Pt+NP9/C catalyst has a much lower ECSA before degradation than the TKK, this is clear from Figure 5.15a. However, it is clear from Figure 5.15b, which shows ECSA as a percentage of the original ECSA, that the rate of ECSA loss for Pt+NP9/C and TKK are similar.

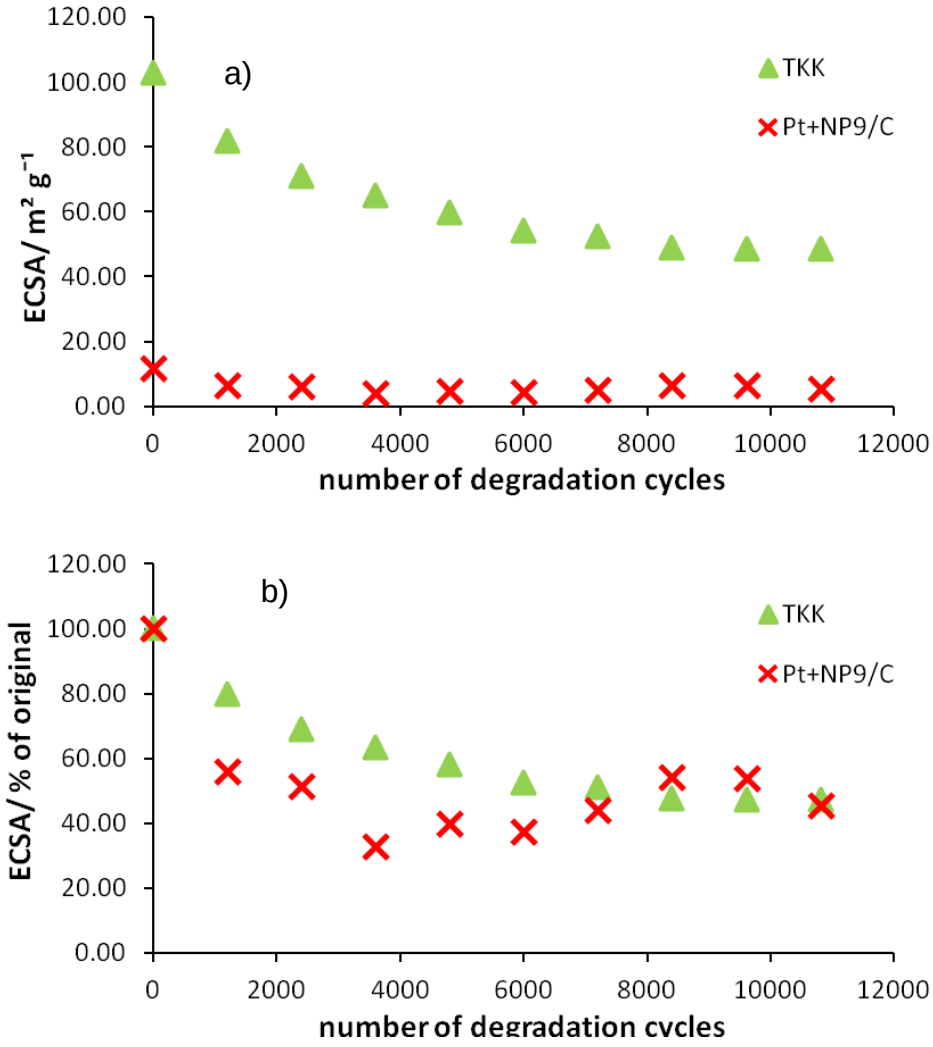

Figure 5-15 *Comparison of catalyst durability during electrochemical cycling in 0.1M $HClO_4$ at 25 ^{o}C.*

Figure 5.16 shows the RRDE data in O_2 saturated $HClO_4$ for both, TKK and Pt+NP9/C, before and after degradation. As seen in the figure, there is no obvious change in ORR performance for the TKK catalyst before and after degradation. In contrast, the Pt+NP9/C catalyst shows a dramatic increase in the ring current after degradation coupled by a more modest decrease in the disc current. The onset of activity has also moved, with $E_{½}$ = 0.87 V before and $E_{½}$ = 0.67 V after degradation (measured at 1600 rpm). All this suggests that the Pt+NP9/C shows a reduction in ORR performance after electrochemical cycling. The TKK shows very little change in ORR performance after electrochemical cycling. This could be due to a number of factors, including change in size and shape of the Pt particles, as well as carbon corrosion. As we did not know the exact carbon support or pre treatment used in the TKK catalyst, the comparison was not necessarily a fair one.

Mayrhofer et al. [189] have developed a method to perform the electrochemical cycling of the catalyst on a TEM grid, so that the exact region can be observed before and after degradation. Using HRTEM, it should be possible to ascertain any changes in catalyst morphology after electrochemical cycling. This line of investigation was not continued due to lack of TEM facilities.

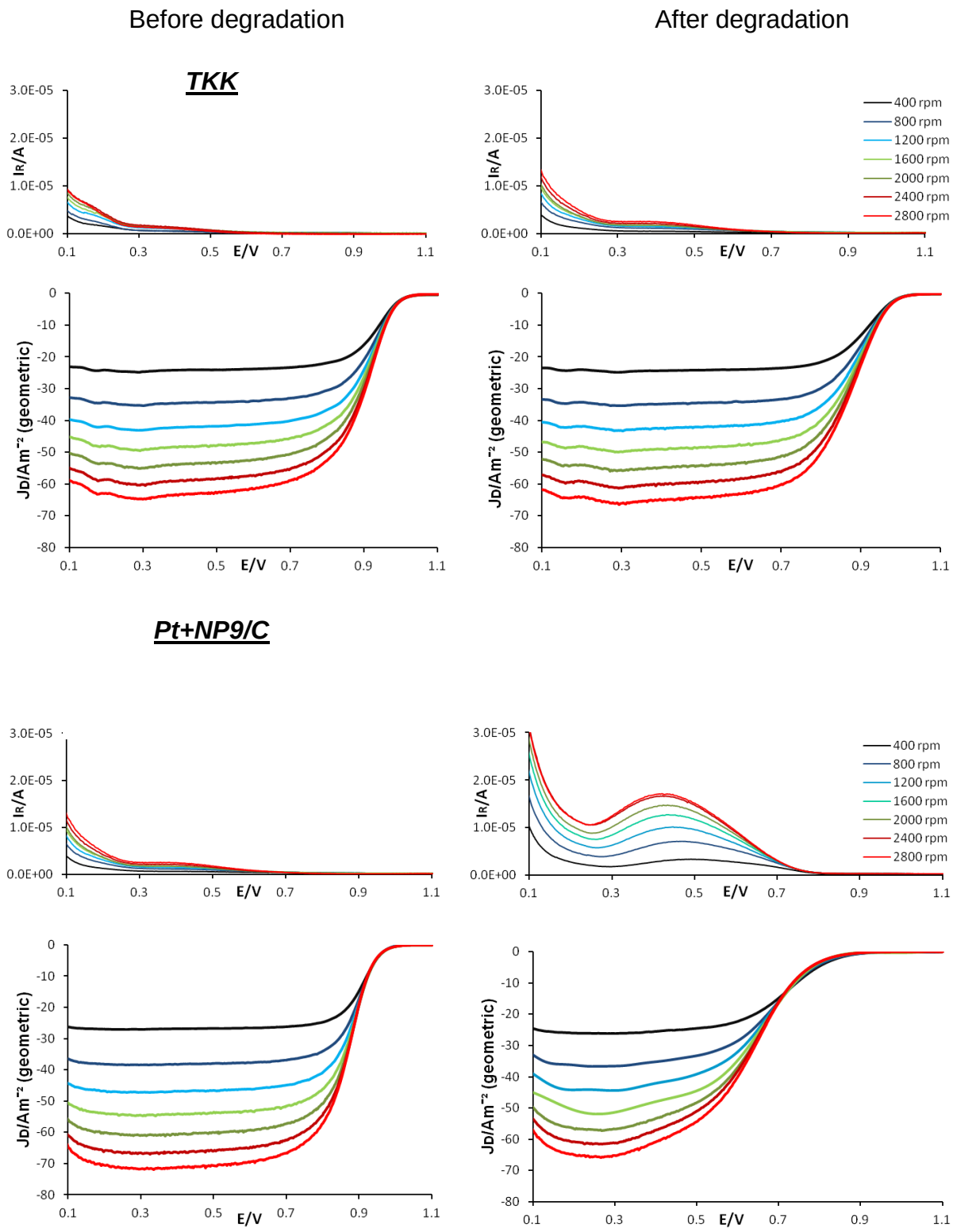

Figure 5-16. *iR-corrected, background-subtracted RRDE data at various rotation rates (ring potential held at 1.1V) ; for Pt/C catalysts 20 µg Pt/cm² geometric on 0.196 cm² GC electrodes in O_2-saturated 0.1 M $HClO_4$ at 25 ºC, before (left) and after (right), degradation. a) TKK b) Pt +TTAB/C.*

5.7 Conclusion

Here, well-dispersed Pt nanoparticles were prepared using the non-ionic surfactant NP9. These particles show good catalytic activity towards the ORR without extensive removal of surfactant. The results presented show that adsorbed surfactant NP9 on Pt nanoparticle surfaces reduces the measured ECSA but does not adversely affect the ORR performance.

The Pt nanoparticles prepared with the cationic surfactant TTAB displayed RRDE voltammetry similar to that observed for Pt in bromide-containing solutions and a greater tendency towards a 2 electron reduction of oxygen, suggesting that bromide ions are blocking active sites. Kinetic analysis showed that reduced mass activity was partly a result of this site-blocking and possibly shape effects, not simply a lower surface area resulting from larger particle size. In summary, by careful choice of surfactant used in the synthesis of Pt nanoparticles, it is possible to generate catalysts that perform well in terms of activity and selectivity towards the 4 electron pathway, without the need for extensive surfactant removal processes.

Chapter 6 The Effect of Adsorbed Surfactants on Pt

In this chapter the effect of adsorbed surfactants on the electrochemistry of the Pt disc and on thin-film RDEs was investigated. The thin film RDEs were prepared, using the commercial catalyst TKK, as described in chapter 5. In chapter 5 the electrochemical behaviour of Pt nanoparticles, prepared using different surfactants, was studied. These results are affected by variations in particle size, shape and degree of dispersion as well as any specific blocking effects of the surfactants. As it is difficult to separate the different factors, it is of interest to first study the effect of adsorbed surfactants on the Pt disc and on nanoparticles of known activity.

Surfactant Adsorption at Interfaces

In aqueous solution surfactants self associate to form micelles, above the critical micelle concentration (cmc). This concentration is dependent on the nature of the surfactant, the temperature and electrolyte concentration. Above the cmc, surfactant monomers are in equilibrium with micelles in solution.

As described in Chapter 2, surfactant adsorption from aqueous solution onto metal surfaces may be driven by electrostatic interaction, van der Waals interactions and the tendency of the hydrocarbon chain to be expelled from aqueous solution. When a metal surface is introduced into a surfactant solution, there will be equilibrium between the surfactant in solution and surfactant

adsorbed on the metal surface, which is dependent on the strength of adsorption of the surfactant to the metal.

The amount of surfactant adsorbed on the Pt surface may be dependent on the concentration of surfactant in solution. It was of interest to determine the effect of surfactants on Pt electrochemistry in the presence and absence of excess surfactant in solution and so, two different approaches were taken to adsorb surfactants onto the Pt electrodes.

6.1 Method 1 Surfactants Added to Electrolyte Solution

6.1.1 Method

The electrochemical methods and equipment used were the same as described in chapter 4. In the first set of experiments, a range of concentrations of the surfactant NP9 in the electrolyte solution (0.1M $HClO_4$) were prepared. The Pt RRDE was allowed to equilibrate in the solution for 1 hour, to allow adsorption of surfactant onto the Pt electrode surface, before electrochemical measurements were taken. Surfactant concentrations above and below the surfactant critical micelle concentration were chosen. The experiment was repeated using TTAB.

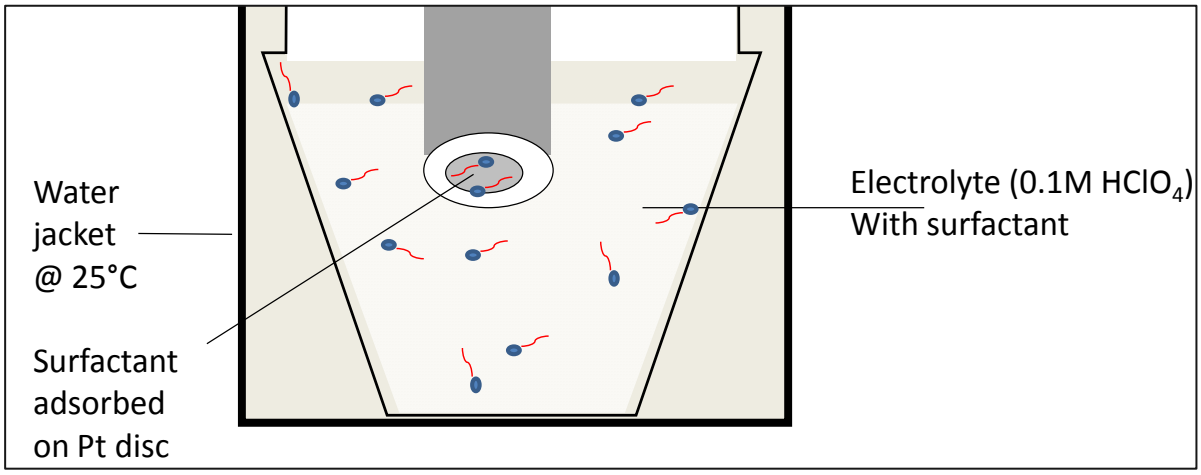

Figure 6-1 *Schematic diagram depicting method 1, electrochemical experiments are conducted in surfactant solutions.*

6.1.2 Results and Discussion

NP9

Figure 6.2a shows the cyclic voltammograms (CVs) of the Pt disc electrode in 0.1 M $HClO_4$ and increasing NP9 concentrations. The Pt disc electrode voltammogram, in 0.1 M $HClO_4$ has the characteristic H desorption peaks [177] at 0.12 and 0.21 V, along with the corresponding cathodic adsorption peaks. The peak at 0.12 V is thought to be due to hydrogen underpotential deposition (H_{upd}) on 110 Pt sites, while the peak at 0.22 V corresponds to 100 terraces and high co-ordination edge and corner Pt sites [47, 157, 158]. As the NP9 concentration is increased these peaks are mostly lost. It is possible that the surfactant molecules may be preferentially adsorbing on to the Pt crystal sites usually responsible for the more distinct H_{upd} features [154, 177]. The ECSA calculated from the area under the H_{upd} peak reduces as surfactant concentration increases, reaching a limit at about 60% of the original ECSA,

suggesting that, on the Pt disc, the NP9 surfactant blocks about 40% of the sites for H adsorption. This is shown graphically in Figure 6.3. Increasing the surfactant concentration above $8x10^{-6}$ M does not increase the surface coverage of surfactant. Figure 6.2b) shows the cyclic voltammograms (CVs) of the TKK RDE in 0.1 M $HClO_4$ at increasing NP9 concentrations. Interestingly surfactant coverage appears to be greater on the TKK film than on the Pt disc. ECSA is reduced to about 20% of the original value suggesting that, on TKK, the NP9 surfactant blocks about 80% of the sites for H adsorption. This could be because NP9 adsorbes mainly on edge sites, of which there are a higher proportion on TKK nanoparticles than on the Pt disc. The other important change in the voltammetry (Figure 6.2), as NP9 concentration is increased, is the greatly reduced magnitude of the peaks for adsorption and desorption of oxygen species on Pt, indicating substantially reduced binding of OH_{ads} species, on both the Pt disc and TKK nanoparticles, as NP9 concentration in solution is increased.

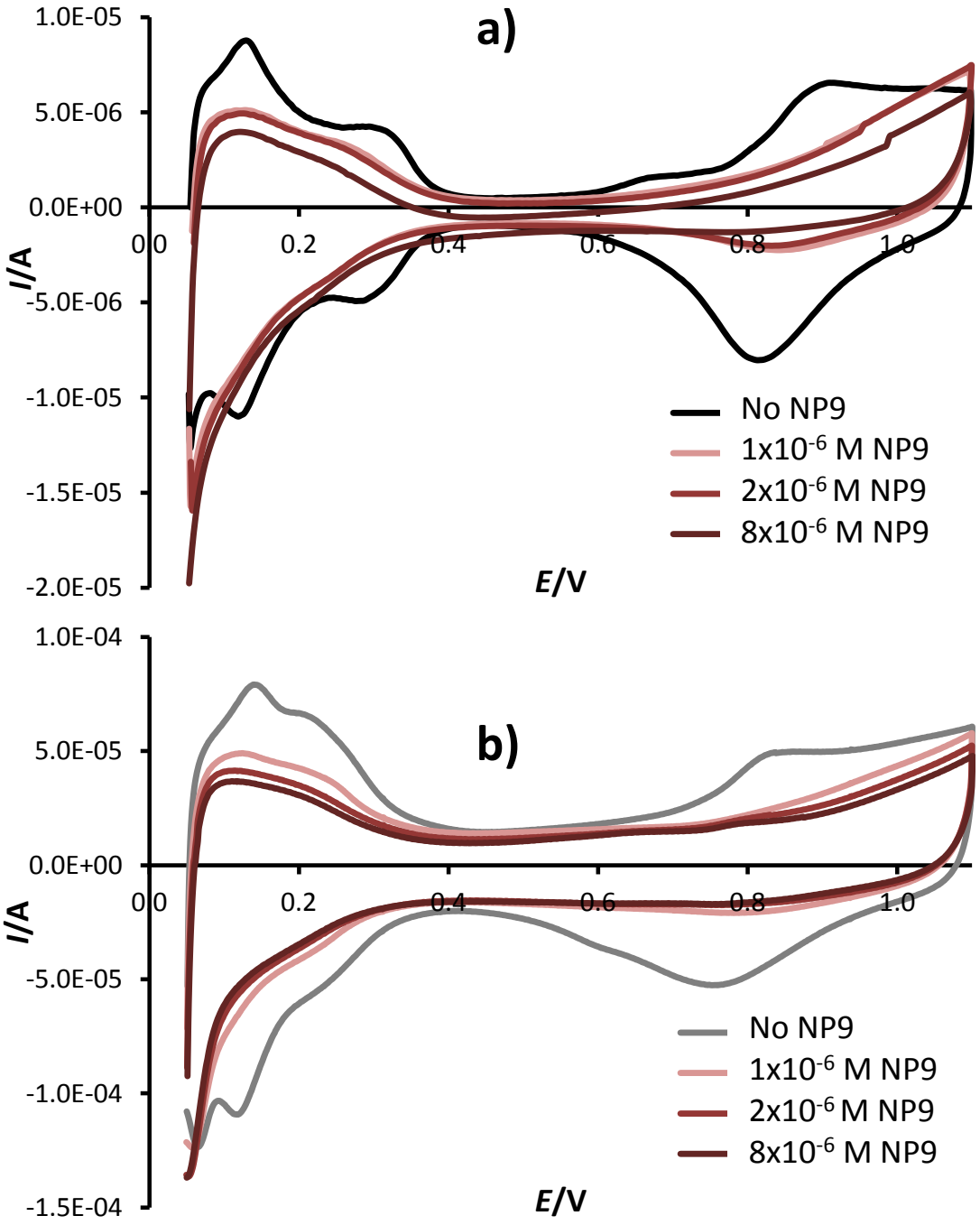

Figure 6-2 *The effect of NP9 concentration on CVs recorded at 25 mV s^{-1} in N_2-saturated in 0.1 M $HClO_4$, a)the 5mm Pt disc at 25 ^oC. b) TKK*

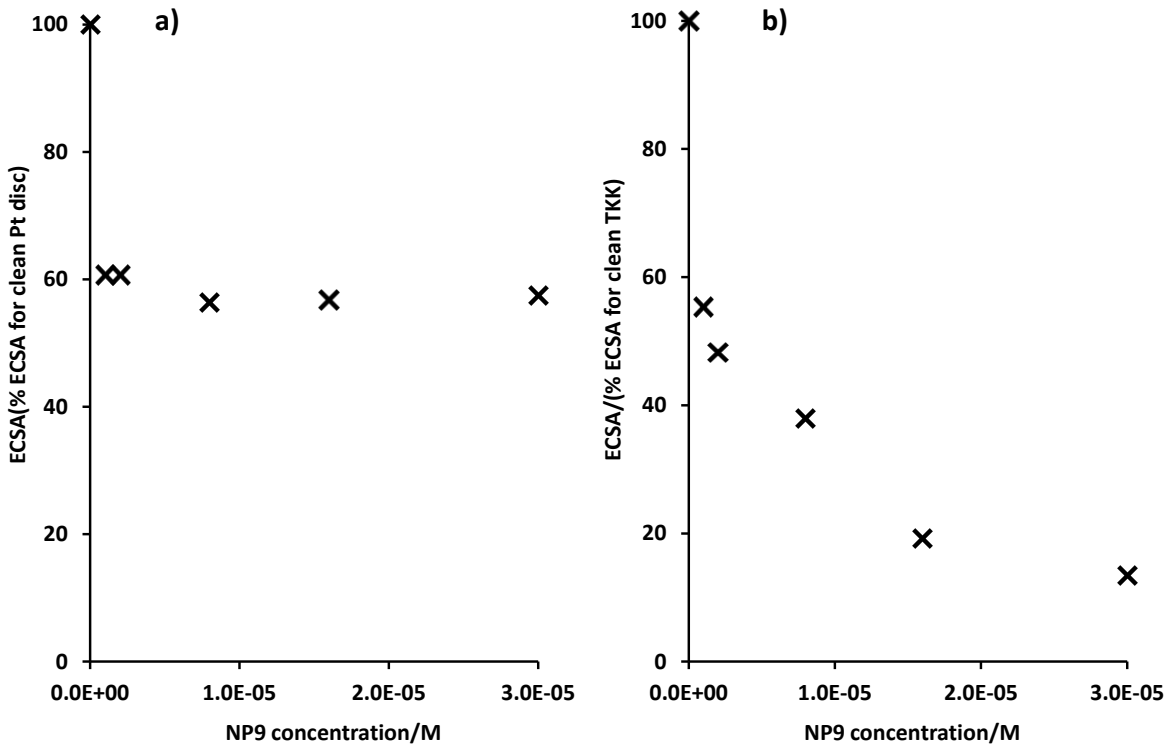

Figure 6-3 *Graphs showing how ECSA varies with NP9 concentration a) for Pt disc, b) for TKK*

Figure 6.4 shows RRDE results for the ORR with Pt ring and disc at increasing concentrations of NP9. Visual observation of the disc currents shows that increasing NP9 concentration leads to a negative shift in $E_{½}$ value. There appears to be no limiting current density plateau, except at the lowest rotation rate for the lower concentrations. The current goes through a maximum before hydrogen desorption then starts to play a role, this maximum decreases with increasing NP9 concentration. This suggests that increasing NP9 concentration has an increasing blocking effect on the ORR.

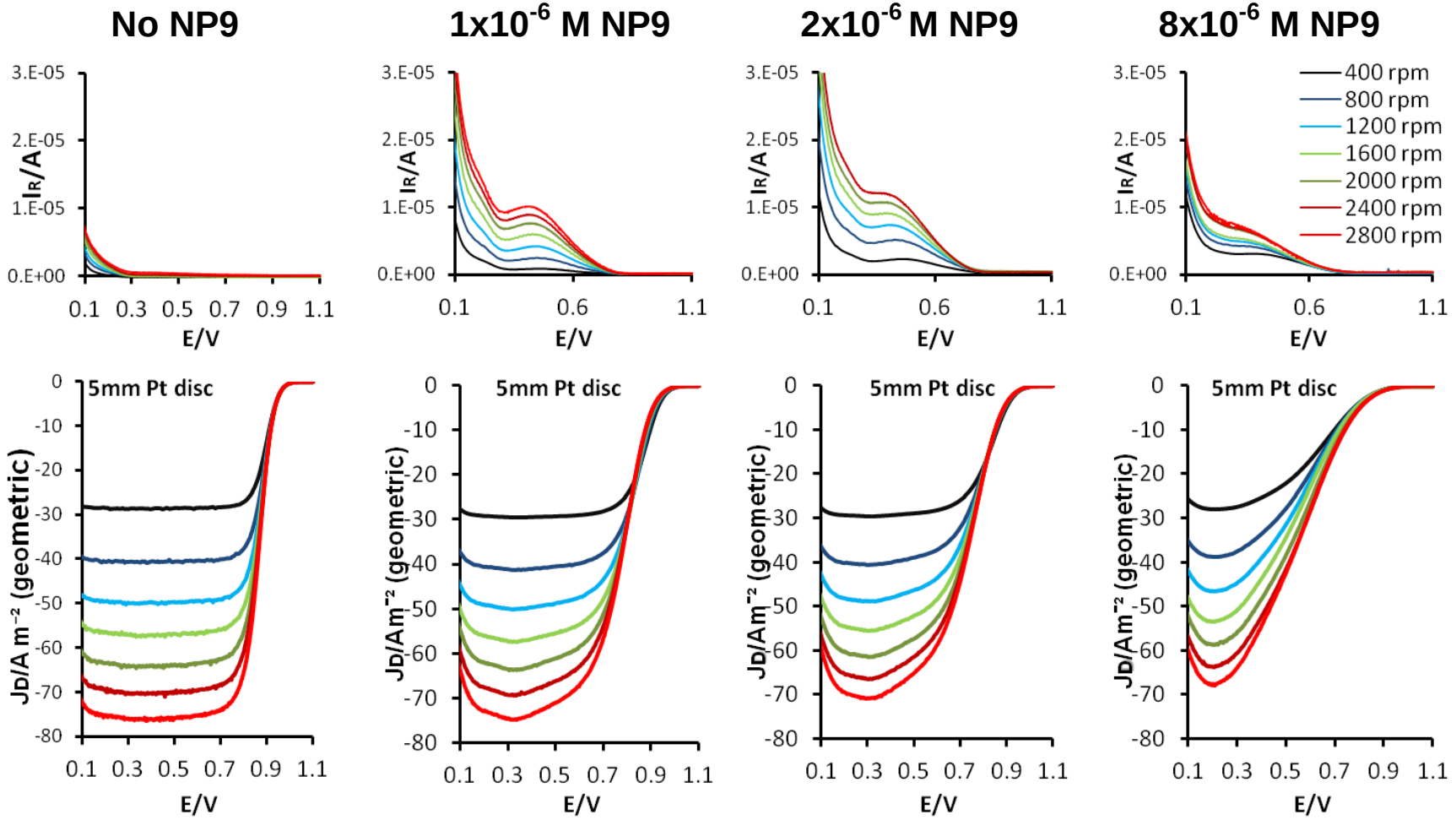

Figure 6-4 *iR-corrected, background-subtracted RRDE data at various rotation rates; for 0.196 cm² Pt disc in O_2-saturated 0.1 M $HClO_4$ at 25 ºC. a) Ring current (ring potential held at 1.1 V), b) disc current.NP9 concentrations increasing from left to right.*

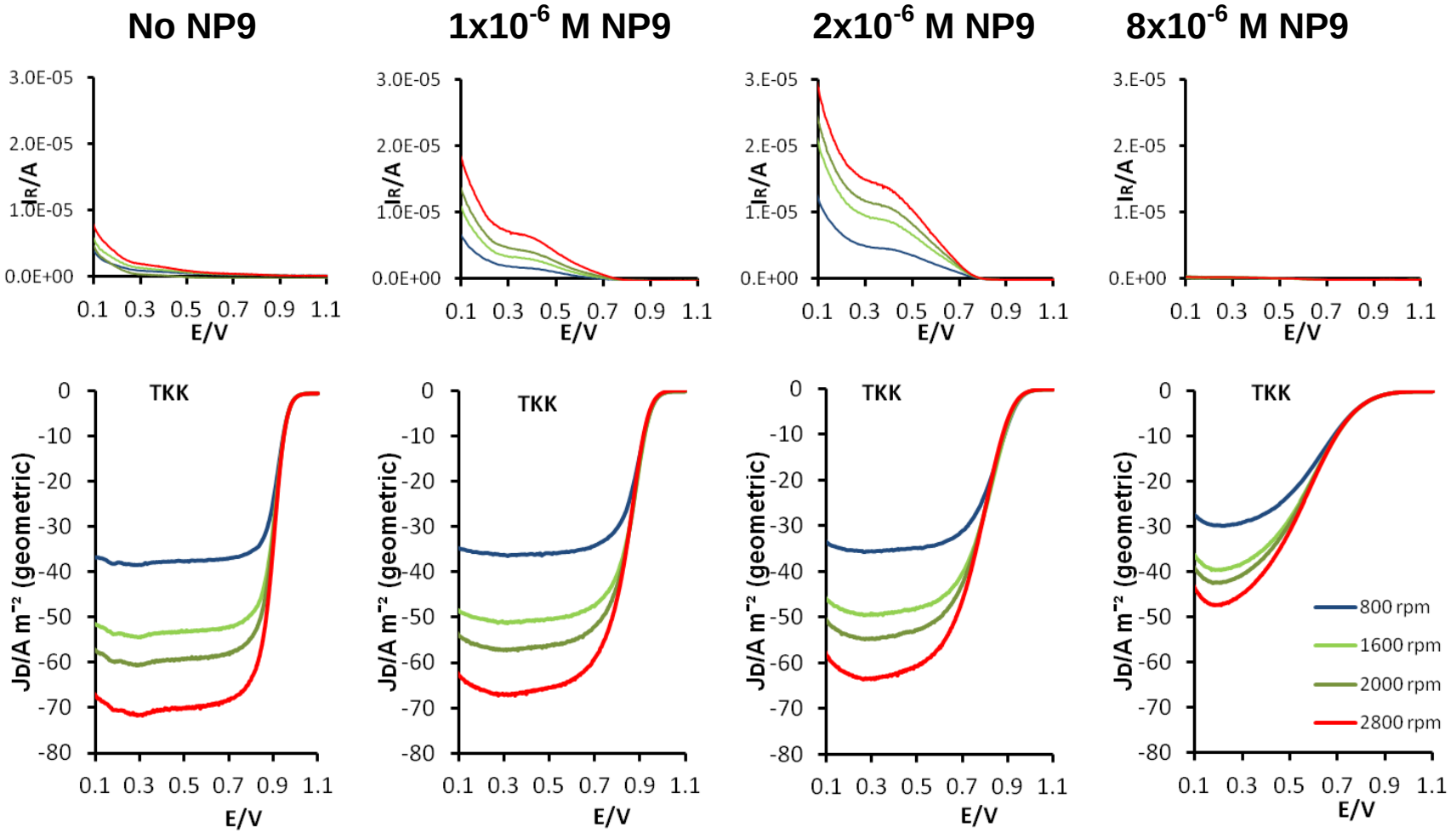

Figure 6-5 *iR-corrected, background-subtracted RRDE data at various rotation rates; for TKK(Pt/C) catalyst 20 µg Pt/cm² geometric on 0.196 cm² GC electrodes in O_2-saturated 0.1 M $HClO_4$ at 25 ºC. a) Ring current (ring potential held at 1.1 V), b) disc current. NP9 concentration increasing from left to right.*

Visual observation of Figure 6.4 shows that ring currents increase as NP9 concentration increases. These results suggest that increasing NP9 concentrations alter the reaction pathway towards the 2 electron production of H_2O_2. This is likely to be a due to blocking of active sites by NP9 molecules, which reduces the availability of adjacent sites for oxygen to adsorb and so reduces the extent of dissociative adsorption, essential for the full reduction to water. As the NP9 concentration increases to $8x10^{-6}$ M the ring currents decrease. This is most likely a result of surfactant adsorption on the Pt ring, which blocks the oxidation of hydrogen peroxide.

Figure 6.5 shows RRDE results for the ORR with Pt ring and TKK thin film disc at increasing concentrations of NP9. Visual observation shows the same trend as for Figure 6.4, using the Pt disc; increasing NP9 concentration leads a negative shift in $E_{½}$ value. There appears to be no limiting current density plateau, except at the lowest rotation rate for the lower concentrations. The current goes through a maximum before hydrogen desorption then starts to play a role, this maximum decreases with increasing NP9 concentration. This suggests that increasing NP9 concentration has an increasing blocking effect on the ORR. This is shown graphically in Figure 6.6. The ring current results suggest that increasing NP9 concentrations alter the reaction pathway towards the 2 electron production of H_2O_2.

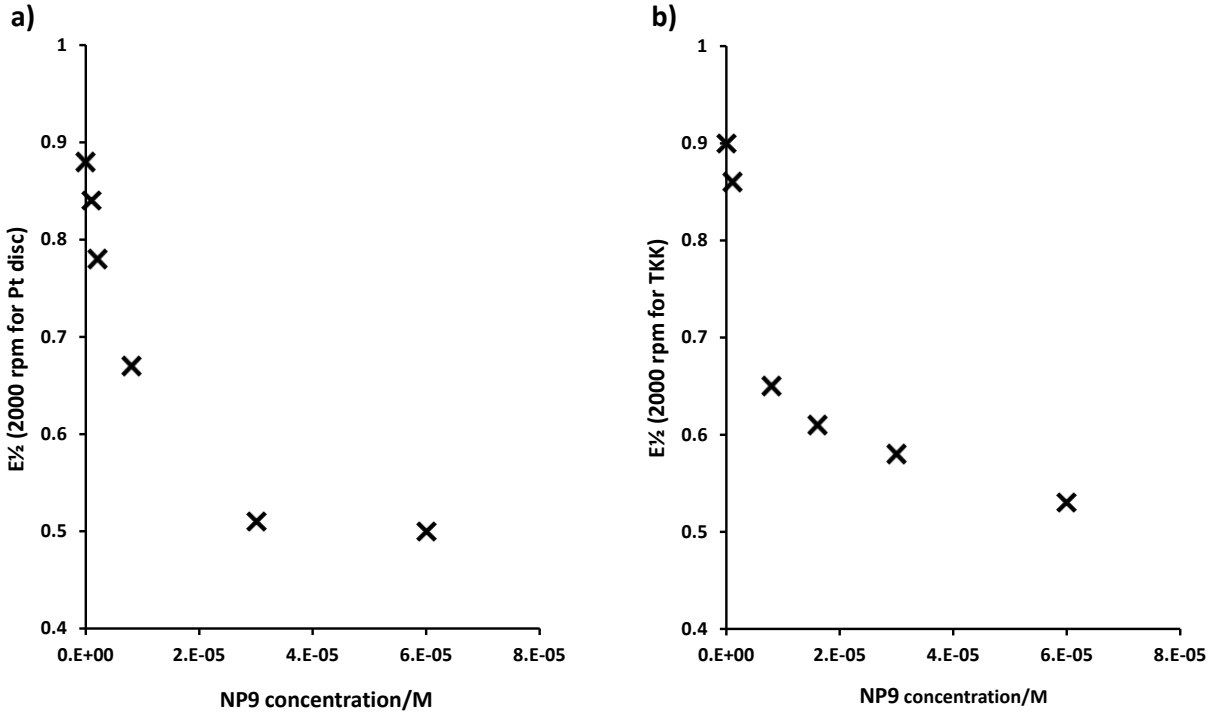

Figure 6-6 *Graphs showing how E½ (2000 rpm) varies with NP9 concentration a) for for Pt disc, b) for TKK*

Figure 6.7 shows the Tafel plots for the Pt disc at increasing NP9 concentrations. From the curvature of the Tafel plots it is clear that there is no single Tafel slope for the reaction in the potential range 0.9 – 0.78 V. For the Pt disc the slope is around –60 mV dec^{-1} at $E > 0.85$ V but doubles to –120 mV dec^{-1} for $E < 0.8$ V. This change in gradient is less marked at increasing surfactant concentrations. In this potential range (0.9 – 0.78 V) kinetic current reduces with increasing surfactant concentration, except at E>0.95 V at the lowest surfactant concentration ($1x10^{-6}$ M).

The results suggest that NP9, at concentrations above $1x10^{-6}$ M, has a detrimental blocking effect on the ORR. It is likely that increasing NP9

concentration in solution will lead to increasing adsorption of NP9 on the Pt surface, for the TKK film and Pt disc. As NP9 concentration is increased beyond the cmc ($7.4x10^{-5}$ M) [190] multilayers may form on the Pt surface. The experiment does not exactly mirror the situation in the fuel cell. In the fuel cell only strongly adsorbed surfactant will remain adsorbed to the nanoparticle surface. Any desorbed NP9 will be quickly washed away.

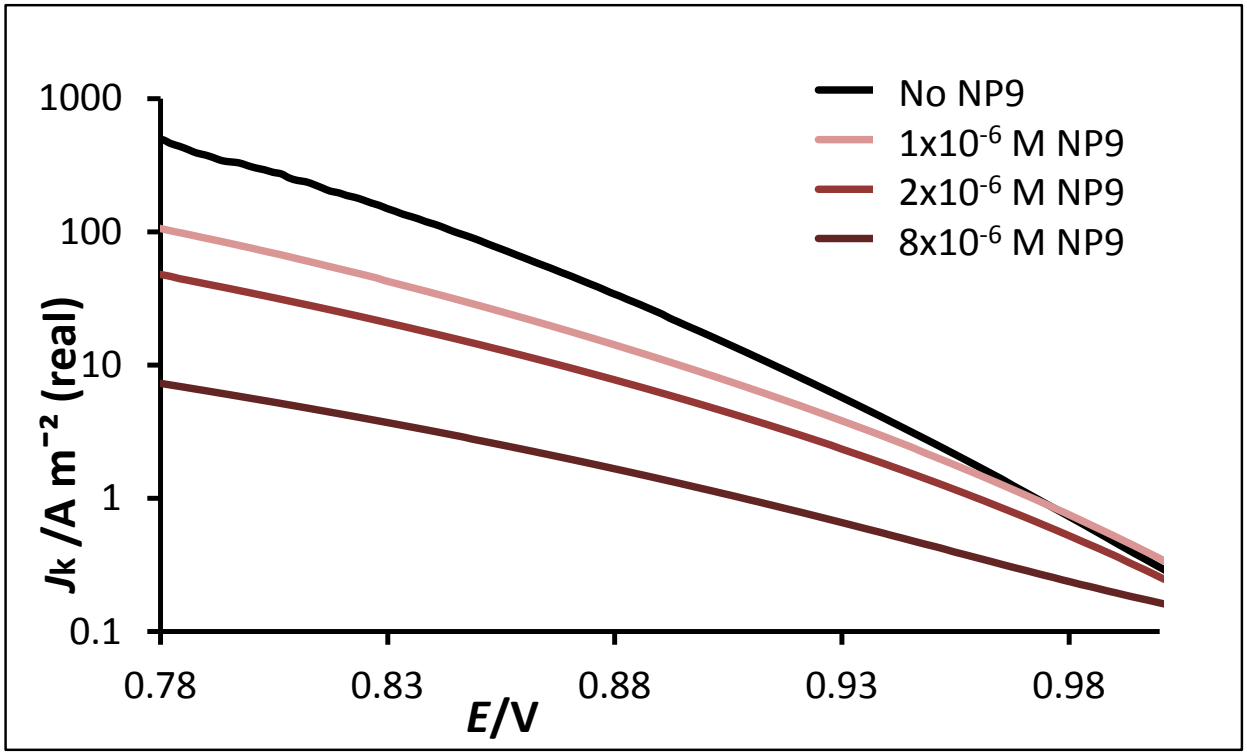

Figure 6-7 *Surface area specific mass transport corrected current densities (calculated from results at 1600rpm) for the ORR on Pt disc at various NP9 concentrations, obtained from positive sweeps (25 mV s^{-1}, 1600 rpm) in 0.1 M $HClO_4$ saturated with O_2 at 25 °C.*

TTAB

The cmc of TTAB ($1.0x10^{-3}$ M) [190] is higher than that for NP9, and therefore a higher TTAB concentration was used. Figure 6.8 shows the cyclic

voltammograms (CVs) of the Pt disc electrode in 0.1 M $HClO_4$ and increasing TTAB concentrations. It is likely that the shape of the curve in the H_{ads} region (below 0.4 V) is affected by adsorption and desorption of TTA^+ ions. The magnitude of the peaks for adsorption and desorption of oxygen species (0.6-1.0 V) on Pt are substantially reduced in the presence of TTAB as for NP9, indicating reduced binding of OH_{ads} species on the Pt disc in the presence of TTAB.

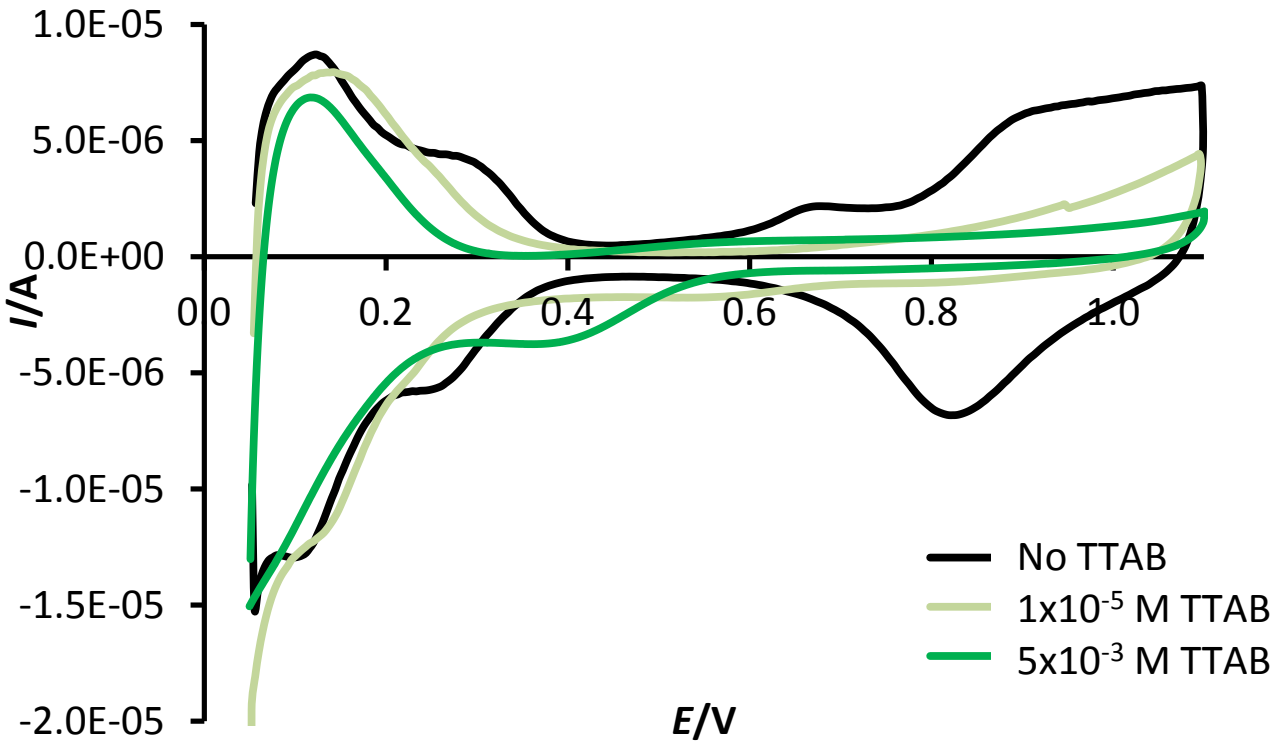

Figure 6-8 *The effect of TTAB on CVs recorded at 25 mV s^{-1} in N_2-saturated in 0.1 M $HClO_4$ for the the 5mm Pt disc at 25 ^oC.*

Figure 6.9 shows RRDE results for the ORR with Pt ring and disc at increasing at TTAB concentrations. At concentrations higher than $1x10^{-5}$ M TTAB, bubbling O_2 caused a high level of foam and this made it difficult to obtain reproducible results. Visual comparison with ORR data for the clean Pt disc (Figure 6.10b) shows that the presence of TTAB leads a negative shift in $E_{½}$ value suggesting that TTAB has a blocking effect on the ORR.

Visual observation (Figure 6.10a) shows that ring currents are higher in the presence of TTAB than on the clean Pt disc. These results suggest that TTAB alters the reaction pathway towards the 2 electron production of H_2O_2, which is likely to result from blocking of sites by bromide counterions from the TTAB surfactant. Bromide ions adsorbed on Pt are known to increase H_2O_2 oxidation currents on the ring electrode, implying that in the presence of bromide ions the ORR does not proceed entirely through the 4-electron pathway [59]. This has been attributed to site blocking, such that pairs of adjacent Pt sites, required for the splitting of the O-O bond, are less abundant.

Figure 6.11 shows the Tafel plots for the Pt disc at increasing NP9 concentrations. It is clear that in the voltage range 0.78-0.9 V kinetic currents are lower in $1x10^{-5}$ M TTAB than on the clean Pt disc.

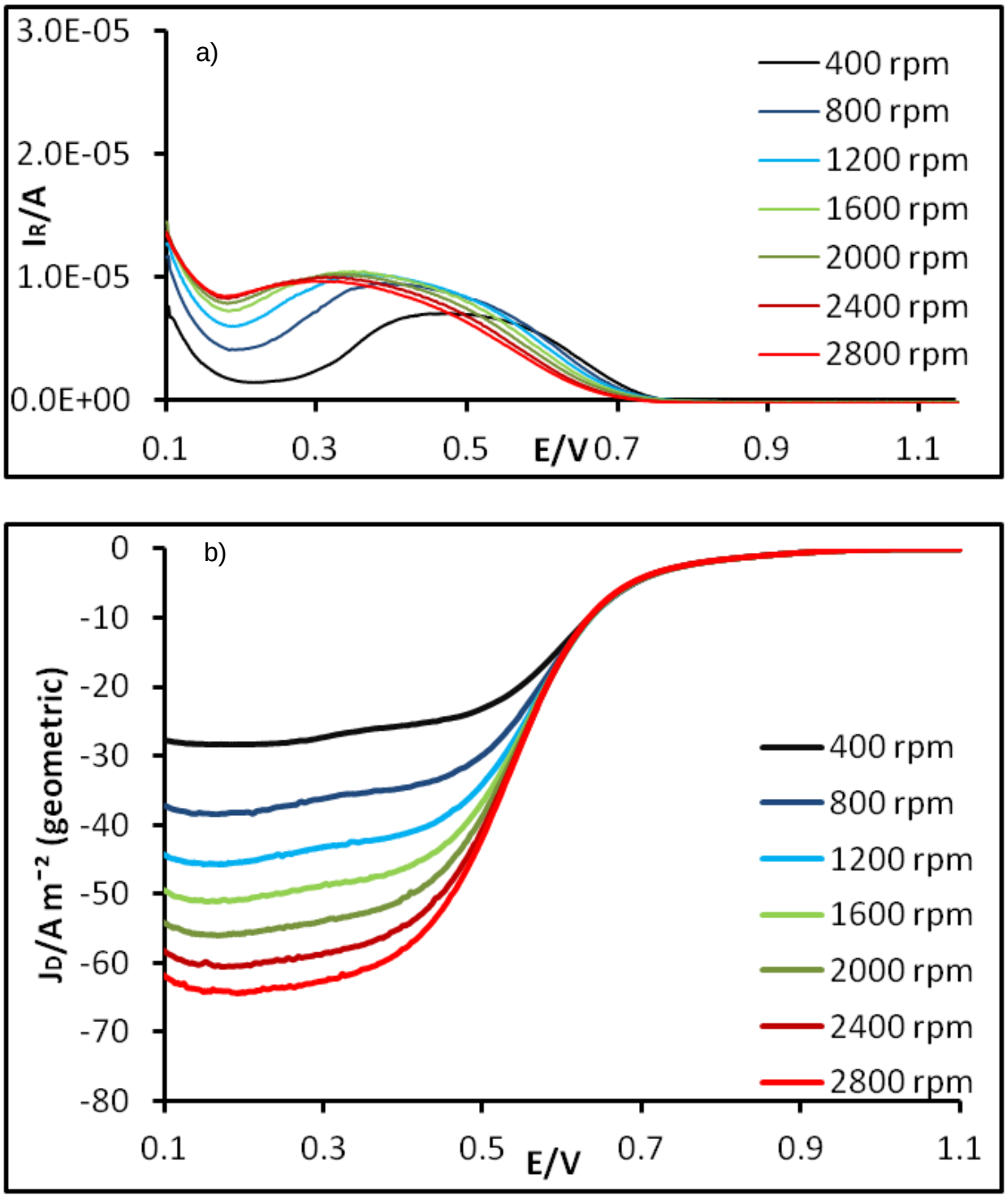

Figure 6-9 *iR-corrected, background-subtracted Pt RRDE data at various rotation rates; in O_2-saturated 0.1 M $HClO_4$ and 1x 10^{-5} M TTAB at 25 ºC. a) Ring current (ring potential held at 1.1 V), b) 0.196 cm² Pt disc current.*

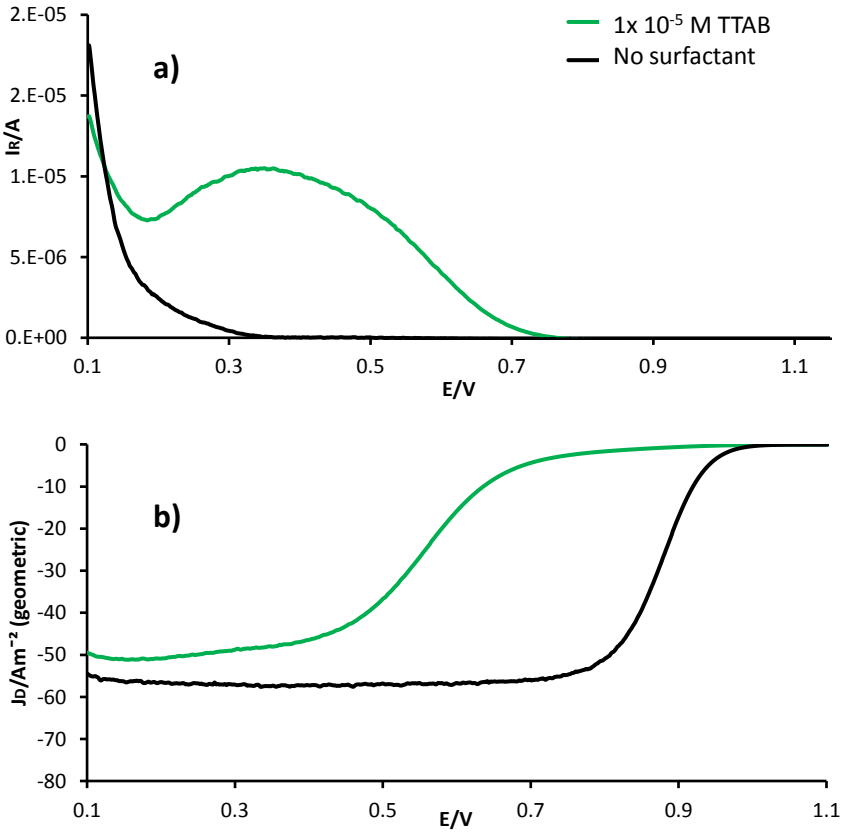

Figure 6-10 *iR-corrected, background-subtracted Pt RRDE data at 1600 rpm; in O_2-saturated 0.1 M $HClO_4$ with and without 1x 10^{-5} M TTAB at 25 ºC. a) Ring current (ring potential held at 1.1 V), b) 0.196 cm² Pt disc current.*

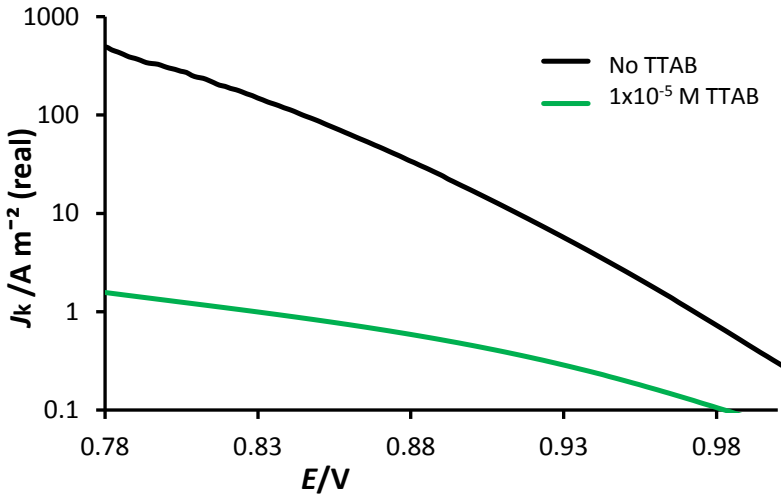

Figure 6-11 *Surface area specific mass transport corrected current densities (calculated from results at 1600rpm) for the ORR on Pt disc with no TTAB and 1x10^{-5} M TTAB concentrations, obtained from positive sweeps (25 mV s^{-1}, 1600 rpm) in 0.1 M $HClO_4$ saturated with O_2 at 25 °C.*

6.2 Method 2, Pre-Adsorption of Surfactant onto the Pt Disc

6.2.1 Method

In the second set of experiments, a range of surfactants and polymers were compared. The Pt RRDE was immersed in 0.01 M surfactant solution, for 1 hour, to allow adsorption of surfactant onto the Pt surface. The electrode was rinsed with Milli-Q water and immersed in freshly prepared 0.1 M $HClO_4$ in the electrochemical cell prior to taking electrochemical measurements, which were carried out according to procedures described in Chapter 5.

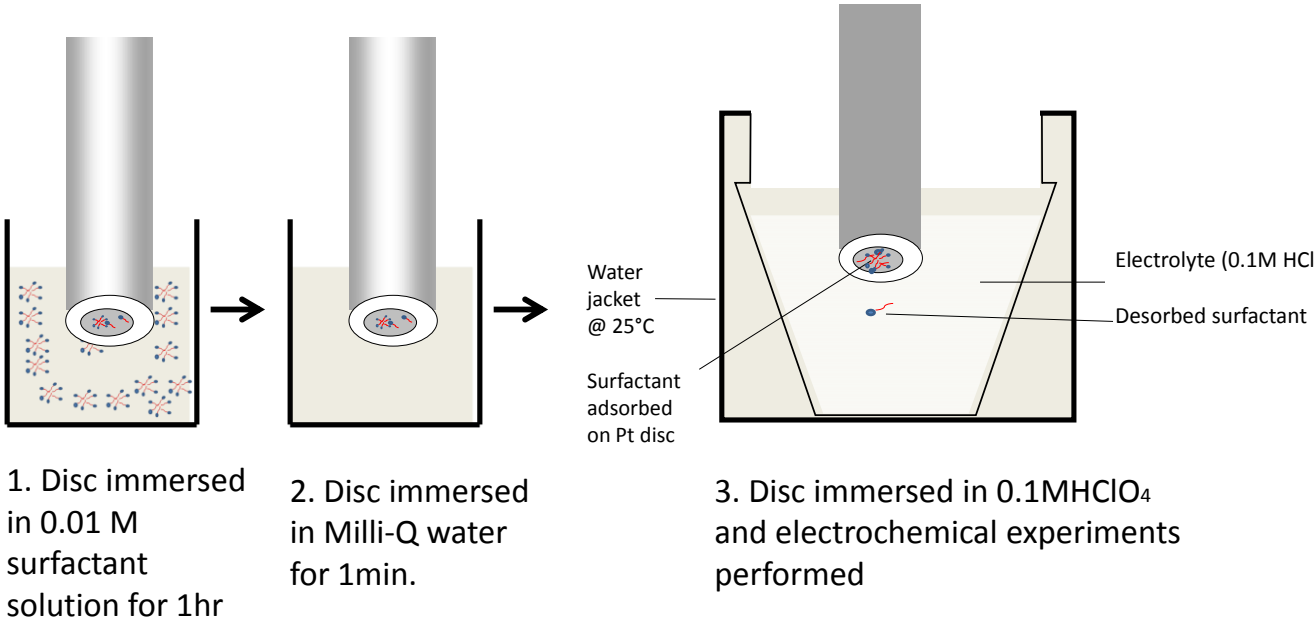

Figure 6-12 *Schematic diagram depicting method 2, electrodes are immersed in surfactant solution and rinsed prior to electrochemical experiments.*

6.2.2 Results and Discussion

These pre-adsorption experiments (method 2) were thought to be most relevant to the situation in the PEM fuel cell. We are interested in the effect of pre-adsorbed surfactant on electrocatalysis. The surfactant adsorbed during nanoparticle synthesis may wash off during electrochemical cycling in the fuel cell and be washed away with the water produced in the reaction. The liquid in the fuel cell does not contain a continuous supply of surfactant.

The structures of the non-ionic surfactants used in these experiments are shown in Figure 6.13. These are all commercially available materials. The purpose was to investigate the effect of changes in the hydrophobic head group. It is well known[190, 191] that the shape of the hydrophobic head group affects the packing arrangement of surfactants on surfaces. The materials were chosen with water solubilities as close as possible to NP9. It was not possible to purchase materials all with exactly the same EO chain length. The EO chain length quoted is an average value for the material, for example NP9 has an average EO chain length of 9.

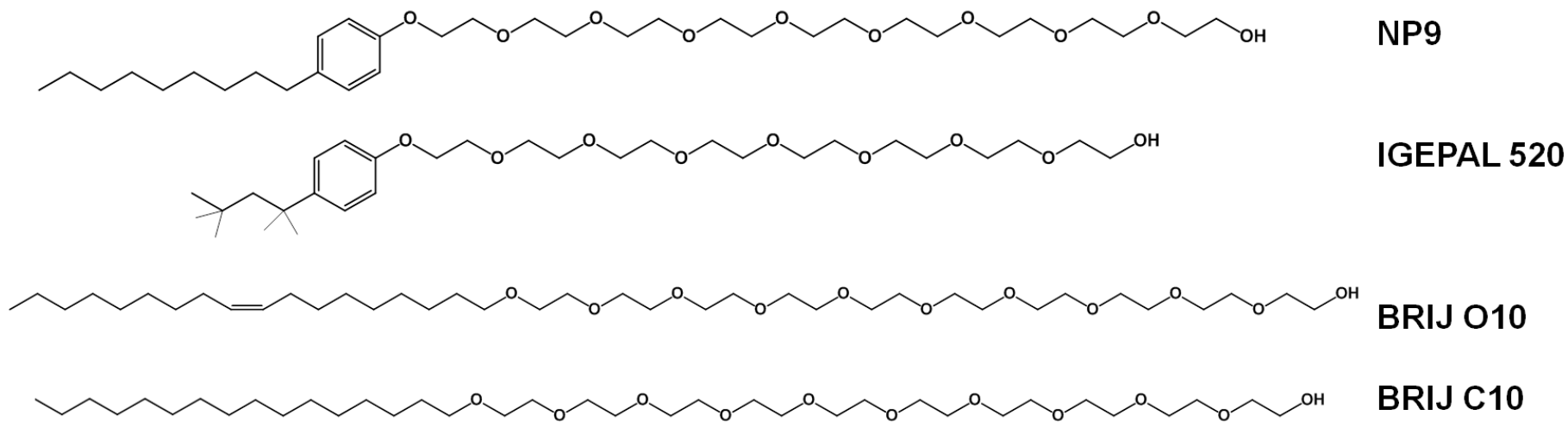

Figure 6-13 *Structures of nonionic surfactants*

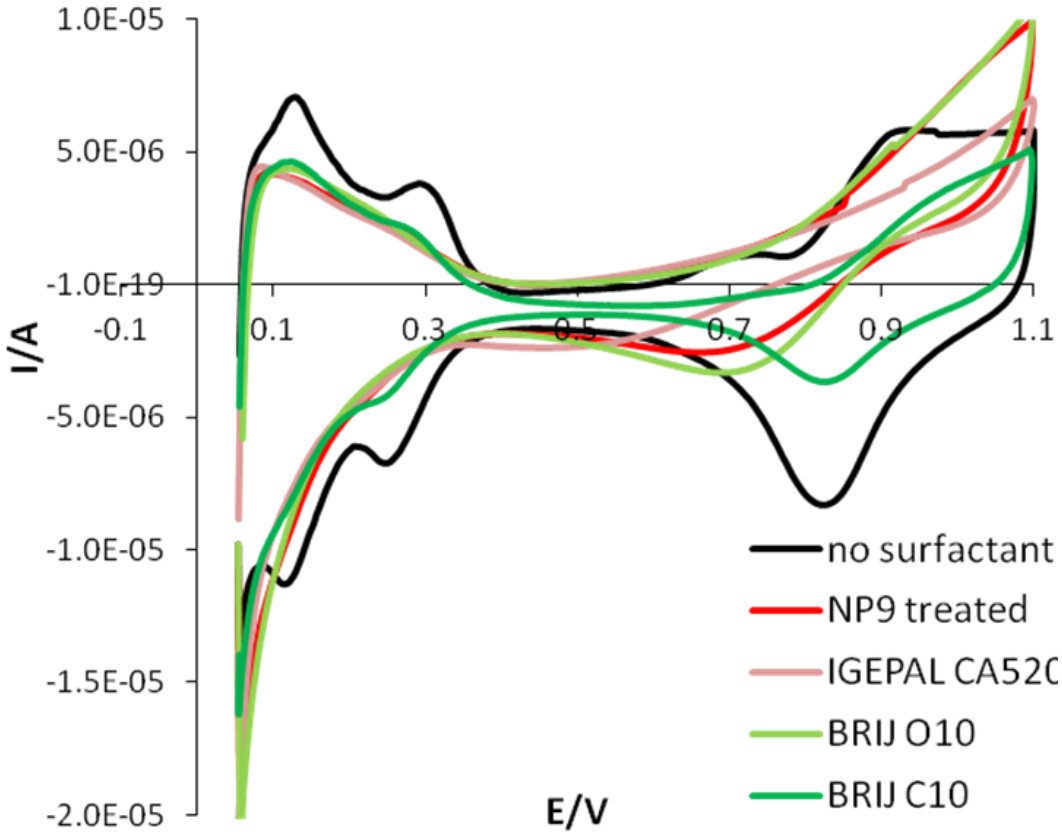

Figure 6-14 *The effect of non-ionic surfactants on CVs recorded at 25 mV/s in N_2-saturated in 0.1 M $HClO_4$ for the the 5mm Pt disc at 25^oC.*

Figure 6.14 shows the cyclic voltammograms (CVs) of the Pt disc electrode in 0.1 M $HClO_4$ after pre-adsorption of non-ionic surfactant, compared to the CV for the clean Pt disc. The voltammogram for the Pt disc electrode, in 0.1 M $HClO_4$ has the characteristic H desorption peaks [177] at 0.12 and 0.21 V, along with the corresponding cathodic adsorption peaks. These peaks are mostly lost after pre-adsorption of non-ionic surfactant as discussed in 6.1 for NP9. The effect is indistinguishable for each of the non-ionic surfactants used. The other important change in the voltammetry (Figure 6.14), is the greatly reduced magnitude of the peaks for adsorption and desorption of oxygen species on Pt, after pre-adsorption of surfactant, indicating substantially reduced binding of

OH_{ads} species. Also the position of these peaks has moved to less positive voltages indicating increased binding energy but reduced coverage of OH_{ads} species in the presence of surfactant. The magnitude of the peaks for adsorption and desorption of oxygen species is lowest for NP9 and IGEPAL CA520.

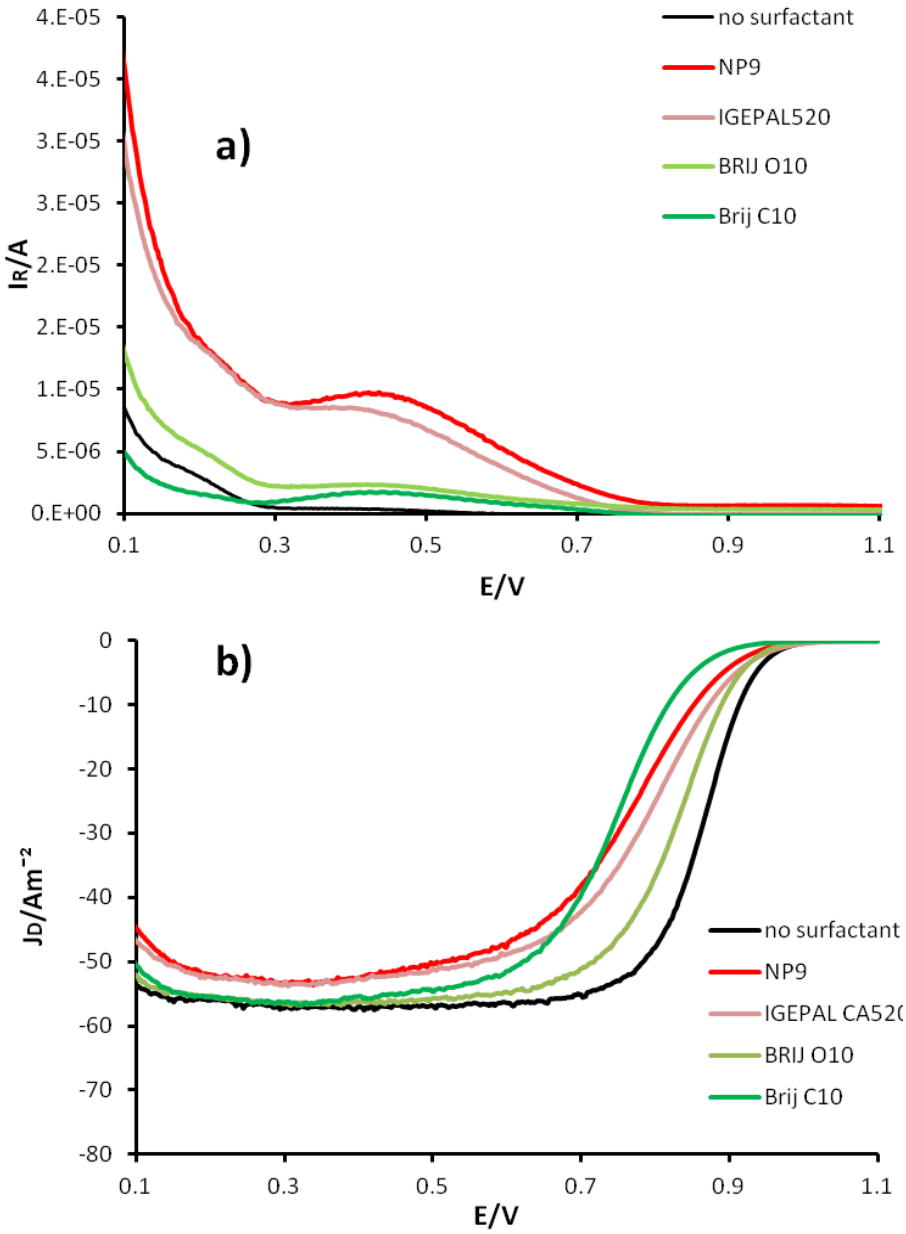

Figure 6-15 *The effect of adsorbed non-ionic surfactant on iR-corrected, background-subtracted Pt RRDE data at 1600 rpm; in O_2-saturated 0.1 M $HClO_4$ at 25 ºC. a) Ring current (ring potential held at 1.1 V), b) 0.196 cm² Pt disc current.*

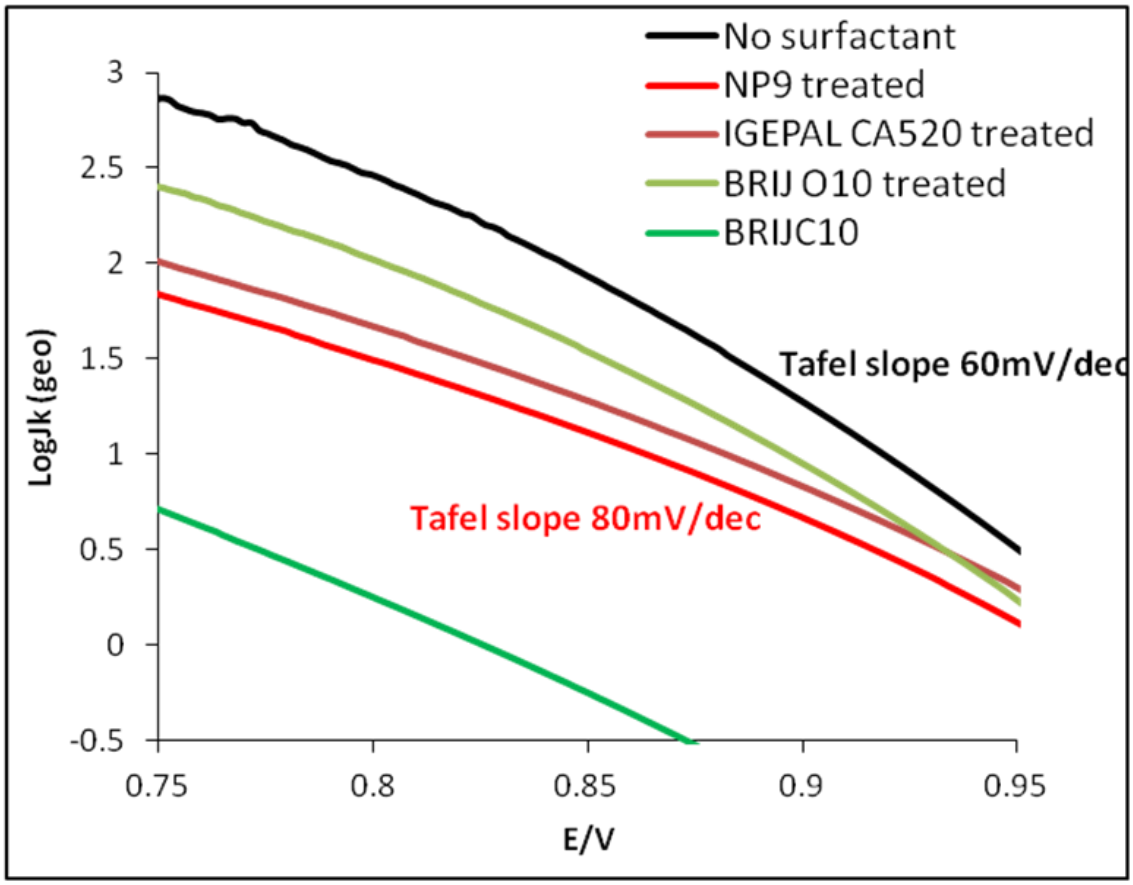

Figure 6-16 *The effect of adsorbed non-ionic surfactant on surface area specific mass transport corrected current densities (calculated from results at 1600rpm) for the ORR on Pt obtained from positive sweeps (25 mV* s^{-1}*, 1600 rpm) in 0.1 M* $HClO_4$ *saturated with* O_2 *at 25 °C. Tafel slopes shown (0.85-0.95 V), in red for NP9 treated and in black for Pt disc.*

The ORR results are shown in Figure 6.15 for the ring and disc at 1600 rpm. It is clear from these results that surfactant structure affects the ORR results. The ring currents are greatest with NP9 and IGEPAL CA520 suggesting that these materials affect the mechanism of the ORR, although the fact that the other surfactants might block the ring towards peroxide oxidation cannot be ruled out. However, these two surfactants also seem to reduce the magnitude of the limiting current on the Pt disc, which indicates that more peroxide is formed in the presence of NP9 and IGEPAL CA520.

These two surfactants also seem to reduce the magnitude of the limiting current on the Pt disc. These two surfactants have an aromatic ring in the hydrophobic chain and it is possible that this causes stronger binding to certain Pt crystal faces. All the surfactants cause $E_{½}$ to move to less positive values. Brij O10 has the least affect on the ORR but this could be because it is easily washed from the surface.

The Tafel plots (Figure 6.16) show further the effect of surfactant structure on the ORR. All the plots show a gradual change in gradient between 0.8-0.85 V. An interesting difference is the Tafel slope of 80 mV/decade (0.85-0.95 V) in the presence of NP9 and IGEPAL CA520 compared to 60 mV/decade in the other cases.

These experiments were also carried out with TTAB and poly acrylic acid (PAA) after pre adsorption, these materials appear to have no measureable effect on the electrochemistry of the disc. The likely reason for this is that either the material did not adsorb onto the Pt disc or it was very weakly adsorbed and washed off easily. Some materials, eg Brij O10, had very little effect. It is not possible to know, without further experiments, whether this surfactant has only adsorbed to give very low surface coverage, or whether it is adsorbing in such a way that it is not affecting the ORR on Pt. For example, Brij O10 may adsorb more strongly to the Pt (100) crystal faces, which are less active for the ORR in $HClO_4$.

An attempt was made to prepare Pt nanoparticles stabilized by Brij O10; this was unsuccessful and is recorded in Chapter 3, Table 3.3.

The use of PAA to prepare stable Pt nanoparticle dispersions has often been reported [109, 192, 193]. In these cases it must adsorb to the nanoparticle surface otherwise the dispersions would be unstable. It is possible that a stronger bond is formed between PAA and Pt during nanoparticle synthesis than the weak physisorption of PAA onto the Pt disc surface. This is also likely to be true for TTAB which has been used in this work to prepare stable Pt nanoparticles. Pre adsorption of TTAB onto the Pt disc had no measurable effect on the N_2 saturated CV or the ORR results. This suggests that any TTAB adsorbed onto the Pt disc was easily washed off during rinsing or the equilibration in electrolyte. Bromide, the counter ion in TTAB is known [185] to have a blocking effect on the ORR.

6.3 Conclusion

The results presented show that adsorbed surfactants on Pt surfaces reduce the measured ECSA and the magnitude of the peaks for adsorption and desorption of oxygen species on Pt,is greatly reduced, indicating substantially reduced binding of OH_{ads} species on both the Pt disc and TKK nanoparticles with surfactant adsorption. The effect on the ORR kinetics varies with surfactant structure.

Chapter 7 Single-Cell PEMFC Testing

In this chapter single cell PEMFC tests are reported. These complement the electrochemical tests described in Chapter 5, which suggest that the excess surfactant present in the Pt nanopartcles, Pt+NP9, does not have an adverse affect on the catalytic activity.

7.1 Fuel Cell Polarisation curves

The thermodynamic treatment of fuel cell reactions has been described in Chapter 2 Equations (2.4) and (2.6) describe the maximum performance that can be obtained theoretically from a fuel cell operating on hydrogen and oxygen (or air). According to this theory the cell would produce a constant voltage of 1.23 V at 25 ºC (or 1.17V at 80 ºC) [114], regardless of the current being drawn. This is not the case in practice and there are various sources of voltage losses. A typical polarisation curve is shown in Figure 7.1 and demonstrates the current-voltage (I-V) response of the cell.

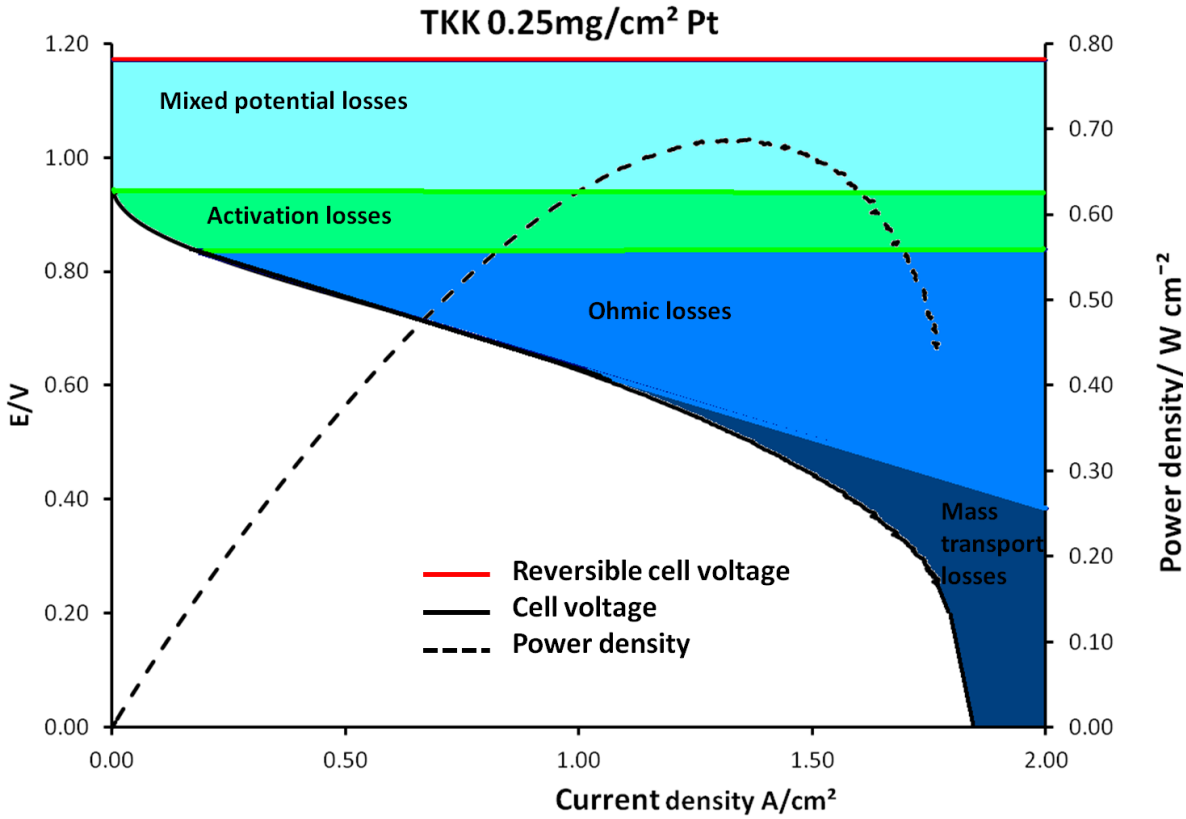

Figure 7-1 *A typical PEMFC polarisation curve (A typical PEMFC polarisation curve (70 ºC), showing contributions of mixed potential, activation, Ohmic and mass transport losses to the overall polarisation response. Obtained using the procedure described in Chapter 7*

The main sources of voltage loss are as follows.

7.1.1 Activation Losses

The activation losses are the result of slow rate or kinetics of the electrochemical reactions taking place at the electrodes and they occur in the low current region of the PEMFC polarisation curve. Electrochemical reactions involve the transfer of electrons to or from the electrode material to one or more reactants. The electrical current is the charge passed per unit time and is therefore a direct measure of the rate of the reaction.

In the PEMFC the electrochemical reactions occur on the surface of a catalyst, usually platinum. The rate of reactions at the anode and cathode in the PEMFC differ considerably. Hydrogen oxidation, at the anode, has relatively fast kinetics involving the transfer of a single electron. As a result, cell activation losses from the anode are relatively small. The ORR is a complex reaction with relatively slow kinetics, involving the transfer of 4 electrons, as described in Chapter 4. As a result the slow cathode kinetics make the largest contribution to activation losses.

The catalyst loading at the PEMFC cathode needs to be much higher than that at the anode, by a factor of 4 or more. Therefore, improvements in the cathode catalyst layer performance offer the greatest potential for reductions in Pt loading. For this reason behaviour of the ORR catalyst is the focus of this research.

7.1.2 Ohmic Losses

Ohmic resistances in the cell result in a simple linear decrease in cell voltage with increasing current. The sources of Ohmic resistance in the cell or stack consist of factors such as; the bulk electrical resistance of cell materials, contact resistances at interfaces between components, and the ionic resistance of the electrolyte membrane and catalyst layers.

7.1.3 Mass Transport Losses

Current density increases as the rate of reaction increases and there is a point at which reactants cannot be supplied quickly enough to the catalyst particles in the electrode to satisfy the current demand. The reactants are being used up quicker than they can be supplied, this causes the concentration of reactants at the electrode surface to decrease, which results in a decrease in electrode potential. Typically, the onset of mass transport limitation occurs above 1 A cm^{-2} .

7.1.4 Mixed Potential Losses

The open-circuit voltage (OCV) of the PEMFC, where no net current flows, is considerably lower than the theoretical cell voltage determined above. This is generally considered to be due to secondary reactions taking place at the cathode, for example oxidation of hydrogen that has diffused through the membrane.

7.2 Methods and Materials

7.2.1 Catalyst Ink Preparation

Pt+NP9 catalysts were synthesised on a 50 mg scale as described in Chapter 3. Inks were prepared using Vulcan XC72R to give the same Pt/C ratio as in TKK (45.9 % Pt). Nafion® dispersion was added to the inks to achieve a 1:1 ratio of

Nafion®:C, the optimum Nafion® concentration suggested in the literature [184, 194]. Inks were ultrasonicated in an ice-cold water bath for 45 minutes.

7.2.2 Reduction of Excess Surfactant in Pt+NP9/C

The Pt+NP9/C catalyst contains a large excess of surfactant. The ratio of Pt:NP9 is approximately 1:3. This is because the original Pt+NP9 is prepared in the presence of a large excess of NP9, only some of which was removed by the centrifugation described in Chapter 3.

Further reduction in the NP9 loading of the Pt+NP9/C ink was achieved by further centrifugation. The ink was diluted with Milli-Q water by a factor of ca.10. The diluted ink was centrifuged at 10,000 rpm for 20 minutes. The supernatant was discarded and the sediment, which redispersed easily, was sonicated for 30 minutes before painting onto the MEA.

7.2.3 MEA Preparation

The MEA preparation was carried out using a method similar to that suggested by Uchida [195]. The 'sonicated' catalyst ink was hand painted onto GDLs with a catalyst loading of 0.25 mg Pt cm^{-2}. The GDL was weighed before painting and again after the ink had been allowed to dry, to confirm the Pt loading. The active area of all MEAs was 16 cm^2. A thin layer of Nafion® solution (Nafion® dry weight of 0.6 mg cm^{-2}) was applied to the commercial E-TEK GDE surface. The

commercial anodes and the painted cathodes were placed on either side of untreated Nafion® 212 membranes. The MEAs were prepared by hot-pressing at 120 ºC for 2 minutes under a pressure of 500 psi. The MEA tests were performed using a Bio-logic FCT-50S PEM Fuel Cell test stand with EIS capabilities.

7.2.4 Polarisation curves

MEAs were activated by holding the cell voltage at 0.6 V for at least 6 hours, or until the current stabilised. Following activation, anodic polarisation curves were recorded from 0.25 V to open circuit, at a scan rate of 1mV s^{-1}.

7.2.5 Electrochemical Impedance Spectroscopy

In this study, a sinusoidally-varying AC current was applied to the cell, and the voltage response (also sinusoidal) was recorded. AC impedance measurements were made at DC current densities of 50 and 500 mA cm^{-2} to investigate the activation and mass transport-limited regions of the cell's polarisation response. The AC perturbation amplitude was set to 5% of the DC current, and measurements were performed at frequencies ranging from 10 kHz to 0.1 Hz.

All measurements were performed at 70 ºC with a gas relative humidity of 50 % and back pressure of 2 bar at the anode and cathode sides in H_2 and air,

respectively. Nominal reactant stoichiometries on the anode and cathode were set at 1.2 (H2) and 2.2 (air) respectively.

7.3 Results and Discussion

Polarisation curves

Figure 7.2 compares the polarisation curves for MEAs prepared using the TKK catalalyst. Two MEAs were prepared using inks containing NP9 surfactant at increasing concentration. These experiments were performed to measure the effect of the NP9 surfactant on the TKK catalyst performance. The MEA with 0.75 mg cm^{-2} NP9 has equivalent loading of NP9 surfactant to an MEA prepared with Pt+NP9/C catalyst.

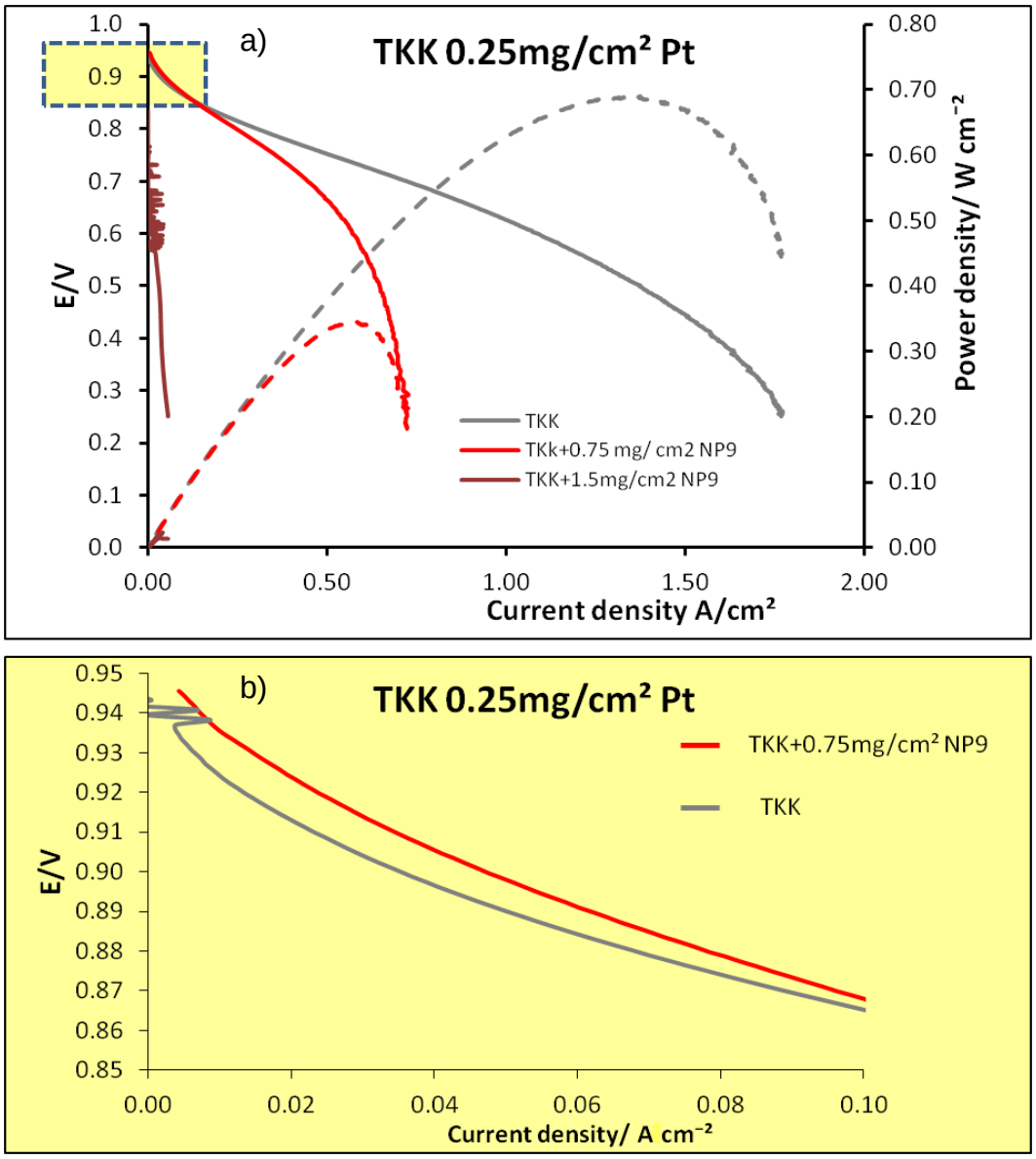

Figure 7-2 *a) Polarisation curves recorded at 2 bar g reactant back pressure for MEAs prepared from TKK,) TKK + 0.75mg/cm^{-2} NP9 and TKK + 1.5mg/cm^{-2} NP9 catalysts. Cathode Pt loading 0.25mg/cm^{-2} in each case. b)Polarisation curve a) expanded to show the behaviour at low current densities.*

It is clear from Figure 7.2 that power density at high current density is reduced with increasing surfactant concentration. The MEA with 1.5 mg cm^{-2} NP9 shows very poor performance at all current densities. The high surfactant loading is adversely affecting mass transport through the MEA. It is likely that the

surfactant is blocking the pores through which oxygen and water diffuse. Figure 7.2b shows an expanded view of the region at low current density. This graph shows that, in this region where catalytic effects dominate, the MEA with 0.75 mg cm^{-2} NP9 shows similar performance to the TKK MEA with no surfactant.

The polarisation curve for the MEA prepared with Pt+NP9/C is shown in Figure 7.3 this MEA showed relatively poor performance, at higher current densities indicating poor mass transport. The excess surfactant in Pt+NP9/C was reduced as described in section 7.2 and the results for an MEA prepared with this ink are also shown in Figure 7.3. It is clear that reduction of the NP9 loading causes improvement in MEA performance especially at higher current densities.

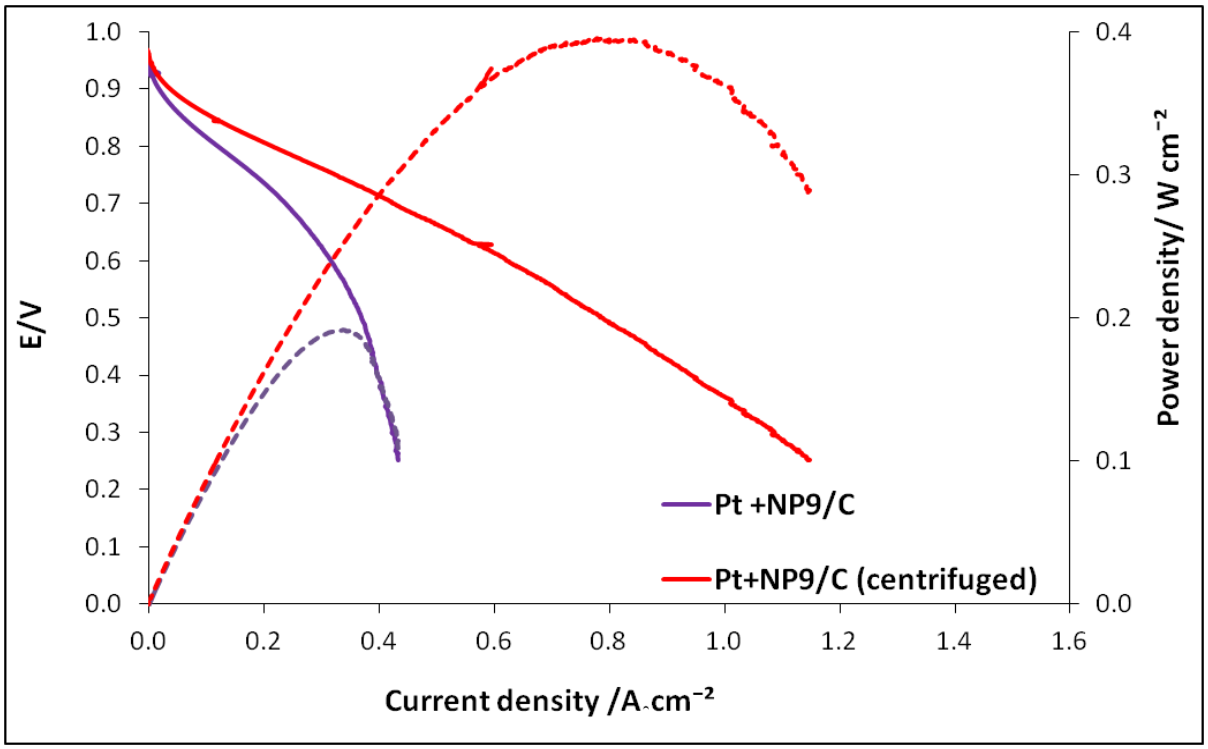

Figure 7-3 *a) Polarisation curves recorded at 2 bar g reactant back pressure for MEAs prepared from Pt+NP9/C (JN47/C) and Pt+NP9/C (JN47/C) after further purification by centrifugation. Cathode Pt loading 0.25 mg* cm^{-2} *in each case.*

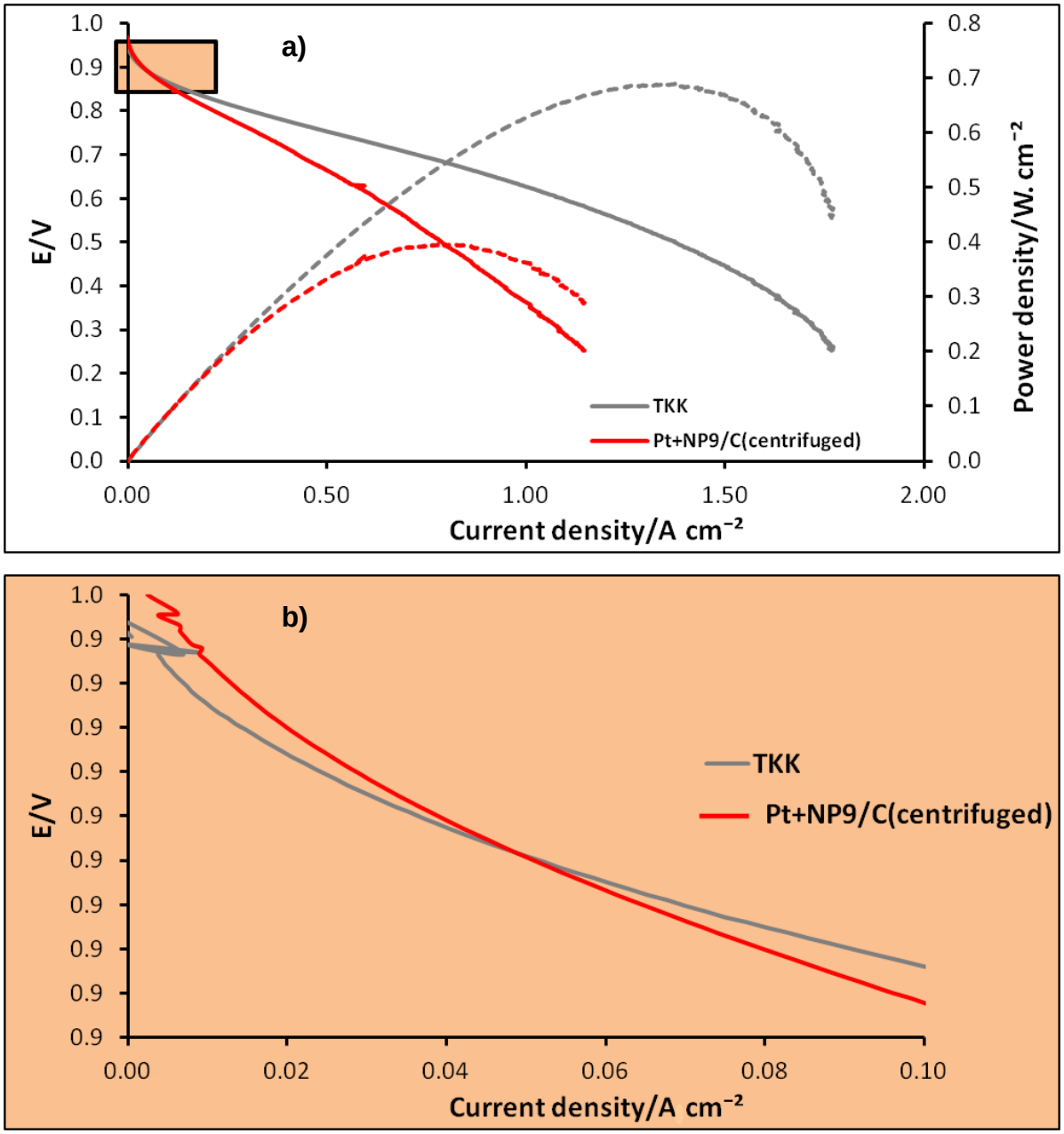

Figure 7-4 *a) Polarisation curves recorded at 2 bar g reactant back pressure for MEAs prepared from TKK, Pt+NP9/C (JN47/C) after further purification by centrifugation. Cathode Pt loading 0.25 mg cm^{-2} in each case. b) Polarisation curve a) expanded to show the behaviour at low current densities*.

Figure 7.4a) and b) compare the performance of the Pt+NP9R/C with the TKK commercial catalyst. The Pt+NP9R/C clearly shows worse performance than

TKK at current densities above 0.5 A cm^{-2} but in the catalytic region below 0.05 A cm^{-2} performance of the two MEAs is similar.

Electrochemical Impedance Spectroscopy

Electrochemical Impedance Spectroscopy (EIS) can be used to measure Ohmic, activation and mass-transport losses which contribute to the performance of the PEMFC. Detailed descriptions of the theory behind this technique are given elsewhere [196]. Typically, EIS measurements are performed at several different frequencies (ω) usually between 10 kHz and 0.1 Hz. A Nyquist plot can be drawn from the results at each frequency. The results of the EIS studies are shown in Figure 7.5-7.7 and allow comparison of the various losses which contribute to the performance of the MEAs. EIS was carried out at 2 bar back pressure and at current densities of 50 and 500 mA cm^{-2}. This allowed investigation of the activation and mass-transport dominated regions of the cells' polarisation responses. The series Ohmic resistance of the cell is the sum of the electrical resistance of cell components, as described earlier in this Chapter. This has no imaginary component and can be simplified to the first point at which the semi circle crosses the Z' axis. This is similar for each MEA, as expected.

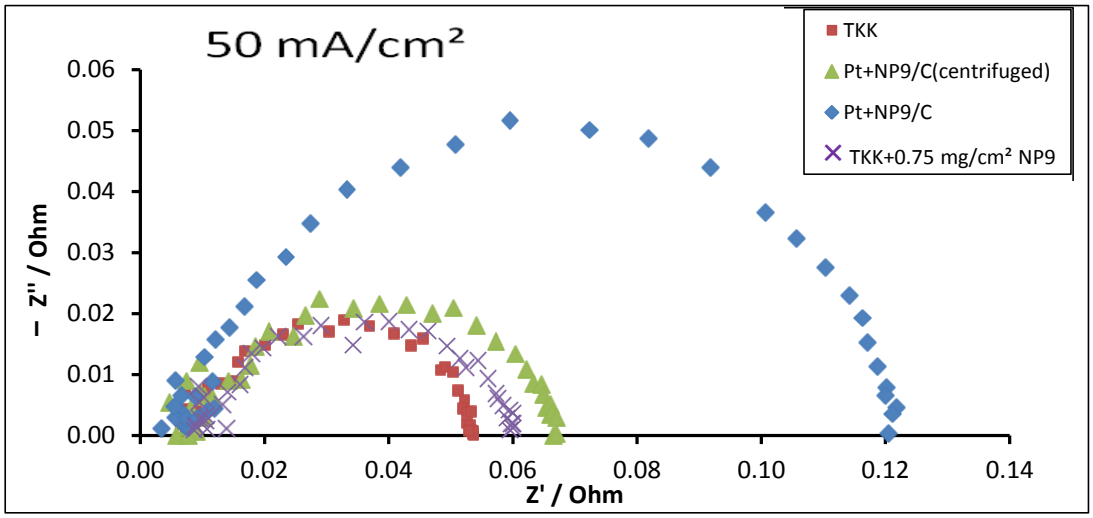

Figure 7-5 *Nyquist plots showing EIS data points (50 mA cm^{-2})*

The EIS measurements taken at 50 mA (Figure 7.5) give information about the reaction kinetics. The diameter of the arc on the Z' axis is taken as a measure of charge transfer resistance [197] due to slow kinetics, the larger the value the slower the kinetics. From Figure 7.5 it is clear that the three catalysts TKK, TKK+0.75 mg cm^{-2} NP9 and Pt+NP9R/C show similar kinetics (the diameter of the arcs on the Z' axis are similar). The Pt + NP9/C appears to have slower kinetics.

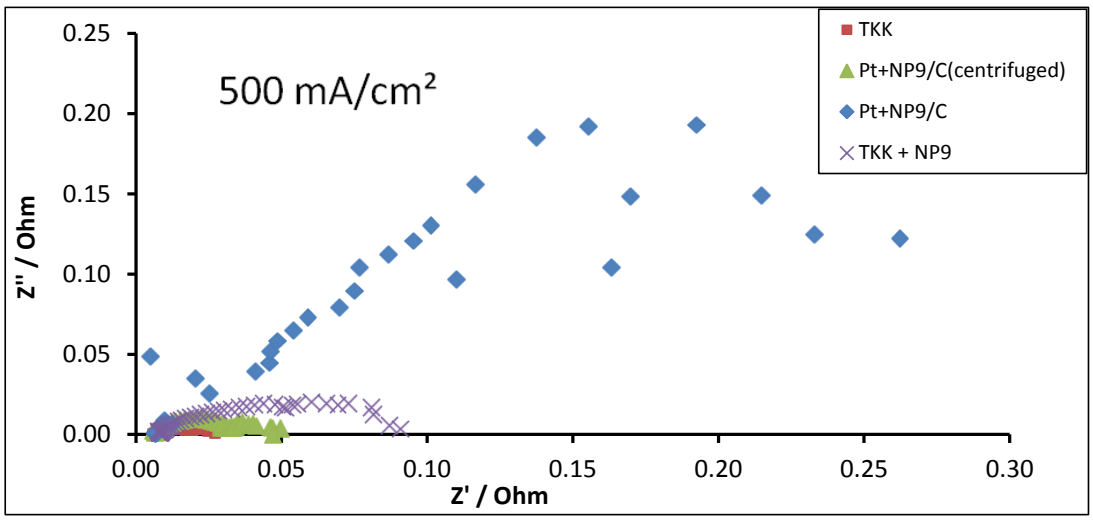

Figure 7-6 *Nyquist plots showing EIS data points (500 mA/cm^2)*

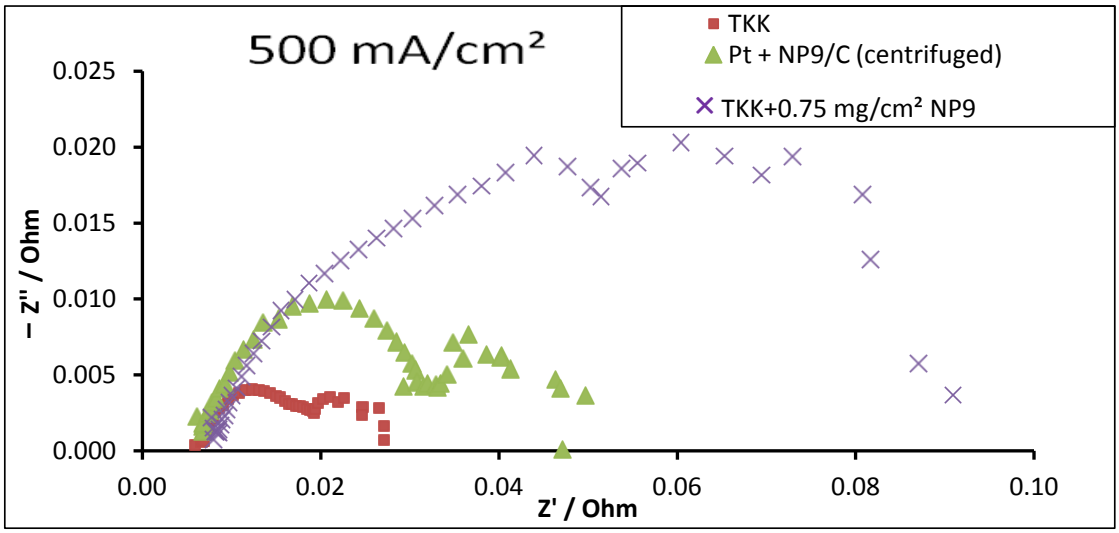

Figure 7-7 *Nyquist plots showing EIS data points (500 mA/cm^2), enlarged scale*

At 500 mA/cm^2 (Figure 7.6 and 7.7) the mass transports resistance is probed. The diameter of the arc on the Z' axis is a measure of the mass transport resistance. This value is much larger for Pt+NP9/C MEA than for the other catalysts. The TKK catalyst, without added NP9 shows the smallest mass transport resistance.

In agreement with the polarisation curve results, the EIS results suggest that the NP9 surfactant has little effect on the kinetics, but slows mass transport within the catalyst layer.

7.4 Conclusion

In conclusion, the single cell PEMFC test results reported here suggest that the NP9 surfactant has little effect on the kinetics of the oxygen reduction in the

MEA, as predicted from the RRDE experiments in Chapter 6. The surfactant does, however, have a negative effect on mass transport through the MEA. We postulate that the surfactant fills the pores and slows diffusion of oxygen and water. Previous work has shown that the mass transport properties of the catalyst layer are highly dependent on its structure [195, 198-200] The catalyst layer of the MEA consists of Pt nanoparticles dispersed over the surface of carbon agglomerates and Nafion®. The carbon agglomerates are made up of much smaller (20-40 nm) primary carbon particles. Figure 7.6 shows a schematic diagram of an MEA cross section calculated using the volumes of materials present in the catalyst layer in this work. This is for the TKK with no added surfactant. It should be pointed out that hydrated Nafion® is a soft, deformable material and that during hot pressing of the MEA it is likely to fill all the larger pores in the catalyst layer. Uchida et al. [199] studied the structure of catalyst layers and defined the pores from 0.02 to 0.04 µm to be the "primary pores" and the pores from 0.04 to 1.0 µm the "secondary pores" in the PEFC. They concluded that the Nafion® added to the catalyst layer cannot penetrate the primary pores and exists only in the secondary pores. The molecular weight of Nafion® is known to fall into the range of 10^5 to 10^6 [201].

Oxygen is likely to diffuse through channels in the Nafion® as described by Sakai [202]. In this work the MEA prepared using Pt+NP9/C consists of at least double the volume of NP9 compared to Nafion® this will completely change the structure and thickness of the catalyst layer. It is likely that the NP9 surfactant will penetrate all the pores. The molecular structure of NP9 is shown in Figure

6.13 the molecule is small relative to Nafion®, with a molecular weight of 617 [203] and will have a molecular diameter less than 0.04 µm and will be able to penetrate the primary pores.

Reduction of surfactant loading as in Pt+NP9R/C showed a marked improvement in mass transport properties. Further reduction in surfactant loading would be possible using a second dilution and centrifugation of the catalyst ink. The TKK catalyst is one of the best performing commercial catalysts and will have been optimised in every way. The carbon black used will be different from that in the Pt+NP9/C, and may have been pre treated. Caution should be applied when making direct comparisons with this catalyst. In this work it was merely used as a benchmark.

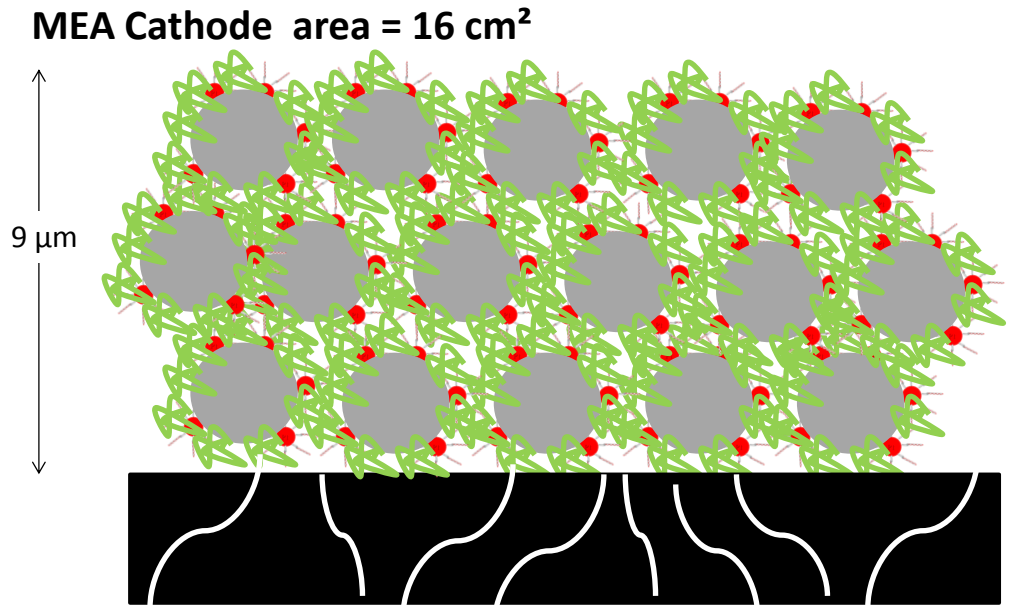

		Volume %
Pt	3.58×10^{-4} cm³	2.5 %
C	5.02×10^{-3} cm³	34.75 %
Nafion	9.05×10^{-3} cm³	62.75 %

Platinum density 21,400 kg m³
C Carbon density 1800 kg m³

Figure 7-8 *Schematic diagram showing possible composition of MEA cross section*

Chapter 8 Discussion

NP9 Surfactant

As described in Chapter 3 stable, well dispersed Pt nanoparticles with average particle diameter 2.8 nm were prepared. This is in the optimum particle size range for fuel cell performance [53, 60, 61] . The results described in Chapter 6 show that these particles show good catalytic activity towards the ORR without extensive removal of excess surfactant. A possible reason for this is that the hydrophobic portion of the NP9 surfactant adsorbs on the edge sites of the Pt nanoparticle as shown in Figure 8,1. The hydrophilic EO chain remains in solution giving the particle steric stability.

Theoretical and experimental studies by Perez- Alonzo et al. [61] and Norskov et al.[53, 204] suggest that the ORR on nanoparticles occurs mainly on terrace sites . Edge & corner sites are blocked by OH_{ads}. Adsorption of OH occurs at potentials more positive than 0.5 V and does not affect the measured ECSA, which is usually measured between 0-0.4 V. If the NP9 surfactant mainly adsorbs on edge sites (blocking OH_{ads}) ECSA will be lower because the surfactant is non-ionic and adsorbes at low and high potentials. This could explain why nanoparticles with adsorbed NP 9 surfactant exhibit lower ECSA than TKK but show similar ORR; the surfactant is adsorbing on sites which would otherwise be blocked by OH_{ads}. In 2-3 nm particles the proportion of edge & corner sites is ca. 75 %,with, 20 % (111) faces, and 5%(100) faces [53, 204]. The proposal that NP9 preferentially adsorbs on edge and corner sites is

supported by the fact that the Pt+NP9/C ECSA is about 25 % of the ECSA for the TKK catalyst with the same average Pt diameter. It is further supported by results in Chapter 6 which show that adsorbed surfactant coverage appears to be greater on the TKK film than on the Pt disc. On TKK ECSA is reduced to about 20 % of the original value, with adsorbed NP9, suggesting that on TKK the NP9 surfactant blocks about 80 % of the sites for H adsorption. This compares with the Pt disc, where ECSA is reduced to about 60 % of the original ECSA, with adsorbed NP9, suggesting that the NP9 surfactant blocks about 40 % of the sites for H adsorption. There are a higher proportion of edge and corner sites on the TKK nanoparticle than on the Pt disc.

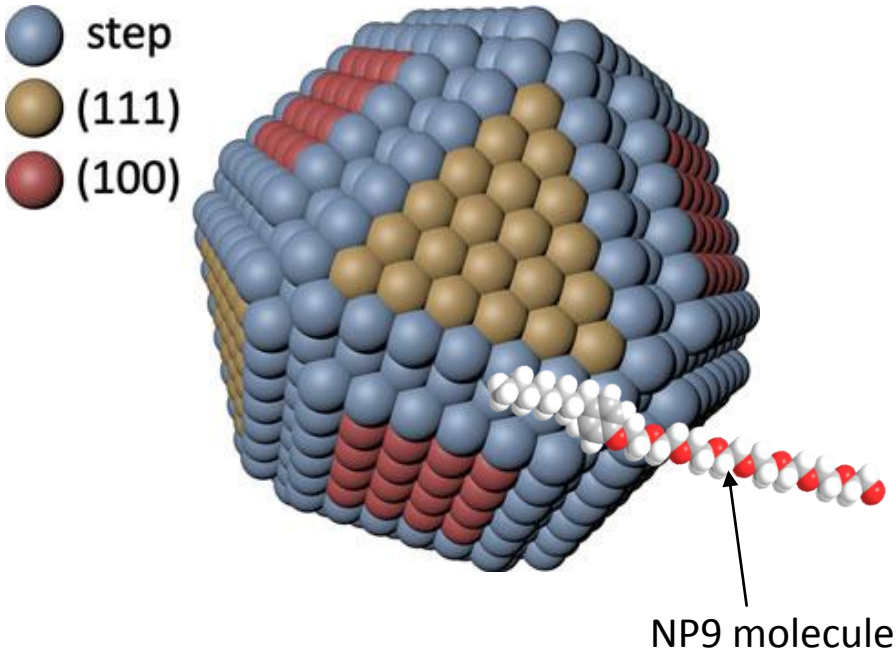

Figure 8-1 *Diagram showing how NP9 surfactant may adsorb on edge sites of Pt nanoparticle*

Further supporting evidence for the adsorption of NP9 on edge sites comes from the shape of the cyclic voltagrams for Pt with adsorbed NP9 (Figure 6.2 and 6.14) and Pt+NP9/C (Figure 5.5); all have lost the features for high co-ordination edge and corner Pt sites.

Another important difference in the voltammetry between the TKK catalyst and Pt+NP9/C films is the greatly reduced magnitude of the peaks for adsorption and desorption of oxygen species on Pt. This indicates substantially reduced binding of OH_{ads} species on the Pt+NP9/C catalyst.

TTAB

Tthe Pt+TTAB/C catalyst shows considerably worse mass activity than the Pt+NP9/C. This effect could be caused by several factors.

First, the larger size of the Pt+TTAB/C particles means that they have a smaller surface area per unit mass than the Pt+NP9/C and TKK catalysts.

Second, the activity will be reduced by the site-blocking effect of the bromide counter-ions of the cationic surfactant; bromide has been shown previously to have a detrimental effect on ORR activity[59, 185].

Third, the Pt+TTAB/C particles are mostly cubic and will mainly have Pt(100) crystal faces, which are known to be less active toward the ORR in perchloric acid solution than Pt(110) and Pt(111) faces [50-52].

It is also possible that the presence of the surfactant inhibits electron transfer between the catalyst and the carbon support, although this effect was not seen for the NP9-stabilized catalysts. It is not possible to separate the effect of bromide ions from that of the organic cation without substantial additional work. This investigation could be a topic for future work. The similarity of the RDE curves with those published [59, 185] for bromide-containing solutions is strong evidence that bromide is at least partially responsible for the lower activity of the Pt+TTAB/C catalyst.

Chapter 9 Conclusions and Further Work

9.1 Conclusions

First, with careful choice of surfactant used in the synthesis of Pt nanoparticles, it is possible to prepare catalysts that perform well in terms of activity and selectivity towards the $4e^-$ pathway, without the need for extensive surfactant removal processes. It may not be necessary to remove all the surfactant used in the preparation of nanoparticles and the surfactants may have a beneficial effect. Here, well-dispersed Pt nanoparticles were prepared using the non-ionic surfactant NP9. These particles show good catalytic activity towards the ORR without extensive removal of surfactant. The results presented show that adsorbed surfactant NP9 on Pt nanoparticle surfaces reduces the measured ECSA but does not adversely affect the ORR performance. The reason for this is thought to be that the NP9 surfactant adsorbs preferentially on edge and corner sites of the nanoparticles, which tend to be blocked by OH_{ads} in the potential range of interest. This gives the possibility to synthesise surfactant-stabilized catalysts which protect catalysts from aggregation without loss in performance.

Second, the choice of surfactant used in the preparation of catalyst nanoparticles obviously affects the nanoparticle size and shape, which in turn affects their catalytic activity. It is difficult to separate the factors involved. The Pt nanoparticles prepared with the cationic surfactant TTAB displayed RRDE

voltammetry similar to that observed for Pt in bromide-containing solutions and a greater tendency towards a $2e^-$ reduction of oxygen, suggesting that bromide ions are blocking active sites. Kinetic analysis showed that reduced mass activity was partly a result of this site-blocking and possibly shape effects, not simply a lower surface area resulting from larger particle size. In summary, by careful choice of surfactant used in the synthesis of Pt nanoparticles, it is possible to generate catalysts that perform well in terms of activity and selectivity towards the $4e^-$ pathway, without the need for extensive surfactant removal processes.

Third, the single cell PEMFC test results reported here suggest that the NP9 surfactant has little effect on the kinetics of the oxygen reduction in the MEA as predicted from the RRDE experiments. The surfactant does however, have a negative effect on mass transport properties. The surfactant may fill the pores in the catalyst layer and slow diffusion of oxygen and water.

9.2 Further Work

This research has opened several possible routes for further work:

- Pt +NP9 particles are well dispersed and reproducible, they can be used in the study of Pt loading/interparticle distance on carbon [70].

- .Single crystal studies with NP9 surfactant on Pt would help to understand the adsorption of Pt on the different crystal faces.

- . The final catalyst could be further optimised for fuel cell use using a final centrifuge step to remove excess surfactant

References

[1] D. Li, C. Wang, D. Tripkovic, S. Sun, N. M. Markovic, and V. R. Stamenkovic, "Surfactant Removal for Colloidal Nanoparticles from Solution Synthesis: The Effect on Catalytic Performance," *ACS Catalysis,* vol. 2, pp. 1358-1362, 2012/07/06 2012.

[2] J. Monzó, M. Koper, and P. Rodriguez, "Removing Polyvinylpyrrolidone from Catalytic Pt Nanoparticles without Modification of Superficial Order," *ChemPhysChem,* vol. 13, pp. 709-715, 2012.

[3] A. Malloy, "Count, size and visualize nanoparticles," *Materials Today,* vol. 14, pp. 170-173, 2011.

[4] F. Birol, "World energy outlook 2010," *International Energy Agency,* 2010.

[5] B. Petroleum, "Putting energy in the spotlight; BP statistical review of world energy June 2005," *Retrieved August,* vol. 23, p. 2005, 2005.

[6] McKinsey and A. Company, "portfolio of power-trains for Europe: a fact-based analysis," ed: Report, 2010.

[7] P. Stevens, "The 'Shale Gas Revolution':Developments and Changes," in *Royal Institute of International Affairs*, ed, 2012.

[8] T. Lipman, R. Ramos, and D. Kammen, "An Assessment of Battery and Hydrogen Energy Storage Systems Integrated with Wind Energy Resources in California. California Energy Commission, PIER Energy-Related Environmental Research," CEC-500-2005-136. Available at/http://www. energy. ca. gov/pier/final_project_reports/CEC-500-2005-136. html S2005.

[9] M. Beaudin, H. Zareipour, A. Schellenberglabe, and W. Rosehart, "Energy storage for mitigating the variability of renewable electricity sources: An updated review," *Energy for Sustainable Development,* vol. 14, pp. 302-314, 2010.

[10] M. H. Ali, *Wind Energy Systems: Solutions for Power Quality and Stabilization*: CRC Press, 2012.

[11] T. Scholte and P. Vaags, "Burning velocities of mixtures of hydrogen, carbon monoxide and methane with air," *Combustion and Flame,* vol. 3, pp. 511-524, 1959.

[12] D. Gielen and M. Taylor, "Modelling industrial energy use: the IEAs energy technology perspectives," *Energy Economics,* vol. 29, pp. 889-912, 2007.

[13] D. MacKay, *Sustainable Energy-without the hot air*: UIT Cambridge, 2008.

[14] A. Stambouli and E. Traversa, "Fuel cells, an alternative to standard sources of energy," *Renewable and Sustainable Energy Reviews,* vol. 6, pp. 297-306, 2002.

[15] S. Lasher, J. Sinha, Y. Yang, and J. Marcinkoski, "VA 5 Cost Analyses of Fuel Cell Stack/Systems," *TIAX LLC, in DOE's 2007 Annual Progress Report,* 2007.

[16] P. L. Adcock, R. T. Barton, C. D. Dudfield, P. J. Mitchell, P. Naylor, and A. Newbold, "Prospects for the application of fuel cells in electric vehicles," *Journal of Power Sources,* vol. 37, pp. 201-207, 1992.

[17] J.-H. Wee, "Applications of proton exchange membrane fuel cell systems," *Renewable and Sustainable Energy Reviews,* vol. 11, pp. 1720-1738, 2007.

[18] I. Staffell, R. Green, and K. Kendall, "Cost targets for domestic fuel cell CHP," *Journal of Power Sources,* vol. 181, pp. 339-349, 2008.

[19] R. K. Shah, U. Desideri, K.-L. Hsueh, and A. V. Vikar, "Research opportunities and challenges in fuel cell science and engineering," in *Proceedings of the 4th Baltic Heat Transfer Conference Kaunas, August*, 2003, pp. 25-27.

[20] B. G. Pollet, I. Staffell, and J. L. Shang, "Current status of hybrid, battery and fuel cell electric vehicles: From electrochemistry to market prospects," *Electrochimica Acta,* vol. 84, pp. 235-249, 2012.
[21] R. K. Ahluwalia, X. Wang, J. Kwon, A. Rousseau, J. Kalinoski, B. James, and J. Marcinkoski, "Performance and cost of automotive fuel cell systems with ultra-low platinum loadings," *Journal of Power Sources,* vol. 196, pp. 4619-4630, 2011.
[22] E. Carlson, P. Kopf, J. Sinha, S. Sriramulu, and Y. Yang, "Cost Analysis of PEM Fuel Cell," *TIAX LLC Cambridge, Massachusetts,* 2005.
[23] B. G. Pollet, I. Staffell, and J. L. Shang, "Current status of hybrid, battery and fuel cell electric vehicles: From electrochemistry to market prospects," *Electrochimica Acta,* vol. 84, pp. 235-249, 2012.
[24] J. D. Hoefelmeyer, R. Koodali, G. Sereda, D. Engebretson, H. Fong, J. Puszynski, R. Shende, and P. Ahrenkiel, "USD Catalysis Group for Alternative Energy," 2011.
[25] O. Z. Sharaf and M. F. Orhan, "An overview of fuel cell technology: Fundamentals and applications," *Renewable and Sustainable Energy Reviews,* vol. 32, pp. 810-853, 2014.
[26] D. Cohen, "Earth audit," *New Scientist,* vol. 194, pp. 34-41, 2007.
[27] R. G. Cawthorn, "The platinum group element deposits of the Bushveld Complex in South Africa," *Platinum Metals Review,* vol. 54, pp. 205-215, 2010.
[28] G. Hoogers, *Fuel cell technology handbook*: CRC press, 2002.
[29] R. J. Allen and H. G. Petrow, "Finely particulated colloidal platinum compound and sol for producing the same, and method of preparation of fuel cell electrodes and the like employing the same," ed: Google Patents, 1977.
[30] S. Srinivasan, E. Ticianelli, C. Derouin, and A. Redondo, "Advances in solid polymer electrolyte fuel cell technology with low platinum loading electrodes," *Journal of Power Sources,* vol. 22, pp. 359-375, 1988.
[31] K. A. Mauritz and R. B. Moore, "State of understanding of Nafion," *Chemical reviews,* vol. 104, pp. 4535-4586, 2004.
[32] K. Malek, M. Eikerling, Q. Wang, T. Navessin, and Z. Liu, "Self-organization in catalyst layers of polymer electrolyte fuel cells," *The Journal of Physical Chemistry C,* vol. 111, pp. 13627-13634, 2007.
[33] J. Zhang, *PEM fuel cell electrocatalysts and catalyst layers: fundamentals and applications*: Springer, 2008.
[34] J. Kerres, "State of art of membrane development," *J. Membr. Sci,* vol. 185, pp. 3-27, 2001.
[35] M. Doyle, G. Rajendran, W. Vielstich, A. Lamm, and H. Gasteiger, "In Handbook of Fuel Cell Fundamentals," *Technology, and Applications,* p. 351, 2003.
[36] T. Ralph, G. Hards, J. Keating, S. Campbell, D. Wilkinson, M. Davis, J. St-Pierre, and M. Johnson, "Low Cost Electrodes for Proton Exchange Membrane Fuel Cells Performance in Single Cells and Ballard Stacks," *Journal of the Electrochemical Society,* vol. 144, pp. 3845-3857, 1997.
[37] P. Hamilton and B. Pollet, "Polymer electrolyte membrane fuel cell (PEMFC) flow field plate: design, materials and characterisation," *Fuel cells,* vol. 10, pp. 489-509, 2010.
[38] H. Wolf and M. Willert-Porada, "Electrically conductive LCP–carbon composite with low carbon content for bipolar plate application in polymer electrolyte membrane fuel cell," *Journal of Power Sources,* vol. 153, pp. 41-46, 2006.
[39] http://www.40fires.org/Wiki.jsp?page=How *a Fuel Cell Works*.

[40] J. K. Nørskov, J. Rossmeisl, A. Logadottir, L. Lindqvist, J. R. Kitchin, T. Bligaard, and H. Jonsson, "Origin of the overpotential for oxygen reduction at a fuel-cell cathode," *The Journal of Physical Chemistry B,* vol. 108, pp. 17886-17892, 2004.

[41] C. Cui, L. Gan, H.-H. Li, S.-H. Yu, M. Heggen, and P. Strasser, "Octahedral PtNi Nanoparticle Catalysts: Exceptional Oxygen Reduction Activity by Tuning the Alloy Particle Surface Composition," *Nano Letters,* vol. 12, pp. 5885-5889, 2012/11/14 2012.

[42] P. Strasser, S. Koh, T. Anniyev, J. Greeley, K. More, C. Yu, Z. Liu, S. Kaya, D. Nordlund, and H. Ogasawara, "Lattice-strain control of the activity in dealloyed core–shell fuel cell catalysts," *Nature Chemistry,* vol. 2, pp. 454-460, 2010.

[43] J. Solla-Gullón, F. Vidal-Iglesias, and J. Feliu, "Shape dependent electrocatalysis," *Annual Reports Section" C"(Physical Chemistry),* vol. 107, pp. 263-297, 2011.

[44] T. Schmidt, N. Markovic, V. Stamenkovic, P. Ross, G. Attard, and D. Watson, "Surface characterization and electrochemical behavior of well-defined Pt-Pd {111} single-crystal surfaces: A comparative study using Pt {111} and palladium-modified Pt {111} electrodes," *Langmuir,* vol. 18, pp. 6969-6975, 2002.

[45] A. R. Tao, S. Habas, and P. Yang, "Shape control of colloidal metal nanocrystals," *Small,* vol. 4, pp. 310-325, 2008.

[46] Z. Peng and H. Yang, "Designer platinum nanoparticles: Control of shape, composition in alloy, nanostructure and electrocatalytic property," *Nano Today,* vol. 4, pp. 143-164, 2009.

[47] N. Markovic, H. Gasteiger, and P. N. Ross, "Kinetics of oxygen reduction on Pt (hkl) electrodes: implications for the crystallite size effect with supported Pt electrocatalysts," *Journal of the Electrochemical Society,* vol. 144, pp. 1591-1597, 1997.

[48] J. Perez, H. M. Villullas, and E. R. Gonzalez, "Structure sensitivity of oxygen reduction on platinum single crystal electrodes in acid solutions," *Journal of Electroanalytical Chemistry,* vol. 435, pp. 179-187, 1997.

[49] V. R. Stamenkovic, B. Fowler, B. S. Mun, G. Wang, P. N. Ross, C. A. Lucas, and N. M. Marković, "Improved Oxygen Reduction Activity on Pt3Ni(111) via Increased Surface Site Availability," *Science,* vol. 315, pp. 493-497, January 26, 2007 2007.

[50] J. Zhang, H. Yang, J. Fang, and S. Zou, "Synthesis and oxygen reduction activity of shape-controlled Pt3Ni nanopolyhedra," *Nano Letters,* vol. 10, pp. 638-644, 2010.

[51] C.-H. Cui, H.-H. Li, X.-J. Liu, M.-R. Gao, and S.-H. Yu, "Surface Composition and Lattice Ordering-Controlled Activity and Durability of CuPt Electrocatalysts for Oxygen Reduction Reaction," *ACS Catalysis,* vol. 2, pp. 916-924, 2012.

[52] J. X. Wang, H. Inada, L. Wu, Y. Zhu, Y. Choi, P. Liu, W.-P. Zhou, and R. R. Adzic, "Oxygen reduction on well-defined core− shell nanocatalysts: particle size, facet, and Pt shell thickness effects," *Journal of the American Chemical Society,* vol. 131, pp. 17298-17302, 2009.

[53] G. Tritsaris, J. Greeley, J. Rossmeisl, and J. K. Nørskov, "Atomic-Scale Modeling of Particle Size Effects for the Oxygen Reduction Reaction on Pt," *Catalysis letters,* vol. 141, pp. 909-913, 2011.

[54] M. Nesselberger, S. Ashton, J. C. Meier, I. Katsounaros, K. J. Mayrhofer, and M. Arenz, "The particle size effect on the oxygen reduction reaction activity of Pt catalysts: Influence of electrolyte and relation to single crystal models," *Journal of the American Chemical Society,* vol. 133, pp. 17428-17433, 2011.

[55] C. Coutanceau, P. Urchaga, S. Brimaud, and S. Baranton, "Colloidal Syntheses of Shape-and Size-Controlled Pt Nanoparticles for Electrocatalysis," *Electrocatalysis,* vol. 3, pp. 75-87, 2012.
[56] K. Kinoshita, "Particle size effects for oxygen reduction on highly dispersed platinum in acid electrolytes," *Journal of the Electrochemical Society,* vol. 137, pp. 845-848, 1990.
[57] H. Yano, J. Inukai, H. Uchida, M. Watanabe, P. K. Babu, T. Kobayashi, J. H. Chung, E. Oldfield, and A. Wieckowski, "Particle-size effect of nanoscale platinum catalysts in oxygen reduction reaction: an electrochemical and 195Pt EC-NMR study," *Physical Chemistry Chemical Physics,* vol. 8, pp. 4932-4939, 2006.
[58] Y. Sun, L. Zhuang, J. Lu, X. Hong, and P. Liu, "Collapse in crystalline structure and decline in catalytic activity of Pt nanoparticles on reducing particle size to 1 nm," *Journal of the American Chemical Society,* vol. 129, pp. 15465-15467, 2007.
[59] N. M. Marković, H. A. Gasteiger, B. N. Grgur, and P. N. Ross, "Oxygen reduction reaction on Pt(111): effects of bromide," *Journal of Electroanalytical Chemistry,* vol. 467, pp. 157-163, 1999.
[60] M. Shao, A. Peles, and K. Shoemaker, "Electrocatalysis on platinum nanoparticles: particle size effect on oxygen reduction reaction activity," *Nano Letters,* vol. 11, pp. 3714-3719, 2011.
[61] F. J. Perez-Alonso, D. N. McCarthy, A. Nierhoff, P. Hernandez-Fernandez, C. Strebel, I. E. Stephens, J. H. Nielsen, and I. Chorkendorff, "The Effect of Size on the Oxygen Electroreduction Activity of Mass-Selected Platinum Nanoparticles," *Angewandte Chemie International Edition,* vol. 51, pp. 4641-4643, 2012.
[62] K. Mayrhofer, B. Blizanac, M. Arenz, V. Stamenkovic, P. Ross, and N. Markovic, "The impact of geometric and surface electronic properties of Pt-catalysts on the particle size effect in electrocatalysis," *The Journal of Physical Chemistry B,* vol. 109, pp. 14433-14440, 2005.
[63] S. Mukerjee and J. McBreen, "Effect of particle size on the electrocatalysis by carbon-supported Pt electrocatalysts: an in situ XAS investigation," *Journal of Electroanalytical Chemistry,* vol. 448, pp. 163-171, 1998.
[64] J. Greeley, J. Rossmeisl, A. Hellmann, and J. K. Norskov, "Theoretical Trends in Particle Size Effects for the Oxygen Reduction Reaction," *Zeitschrift für Physikalische Chemie,* vol. 221, pp. 1209-1220, 2007/10/01 2007.
[65] V. Stamenkovic, B. S. Mun, K. J. Mayrhofer, P. N. Ross, N. M. Markovic, J. Rossmeisl, J. Greeley, and J. K. Nørskov, "Changing the activity of electrocatalysts for oxygen reduction by tuning the surface electronic structure," *Angewandte Chemie,* vol. 118, pp. 2963-2967, 2006.
[66] K. J. J. Mayrhofer, D. Strmcnik, B. B. Blizanac, V. Stamenkovic, M. Arenz, and N. M. Markovic, "Measurement of oxygen reduction activities via the rotating disc electrode method: From Pt model surfaces to carbon-supported high surface area catalysts," *Electrochimica Acta,* vol. 53, pp. 3181-3188, 2008.
[67] M. Watanabe, H. Sei, and P. Stonehart, "The influence of platinum crystallite size on the electroreduction of oxygen," *Journal of Electroanalytical Chemistry and Interfacial Electrochemistry,* vol. 261, pp. 375-387, 1989.
[68] M. Watanabe, S. Saegusa, and P. Stonehart, "Electro-catalytic activity on supported platinum crystallites for oxygen reduction in sulphuric acid," *Chemistry Letters,* pp. 1487-1490, 1988.

[69] M. Watanabe, S. Saegusa, and P. Stonehart, "High platinum electrocatalyst utilizations for direct methanol oxidation," *Journal of Electroanalytical Chemistry and Interfacial Electrochemistry,* vol. 271, pp. 213-220, 1989.
[70] J. Speder, L. Altmann, M. Bäumer, J. J. Kirkensgaard, K. Mortensen, and M. Arenz, "The particle proximity effect: from model to high surface area fuel cell catalysts," *RSC Advances,* vol. 4, pp. 14971-14978, 2014.
[71] J. J. Pietron, Y. Garsany, O. Baturina, K. E. Swider-Lyons, R. M. Stroud, D. E. Ramaker, and T. L. Schull, "Electrochemical observation of ligand effects on oxygen reduction at ligand-stabilized Pt nanoparticle electrocatalysts," *Electrochemical and Solid State Letters,* vol. 11, pp. B161-B165, 2008.
[72] B. Derjaguin, "Theory of the stability of strongly charged lyophobic sols and the adhesion of strongly charged particles in solutions of electrolytes," *Acta Physicochim. USSR,* vol. 14, pp. 633-662, 1941.
[73] E. J. W. Verwey, J. T. G. Overbeek, and K. Van Nes, *Theory of the stability of lyophobic colloids: the interaction of sol particles having an electric double layer*: Elsevier New York, 1948.
[74] T. F. Tadros, *Colloids in Paints* vol. 6: Wiley-VCH, 2010.
[75] E. W. Fischer, "Elektronenmikroskopische Untersuchungen zur Stabilität von Suspensionen in makromolekularen Lösungen," *Colloid & Polymer Science,* vol. 160, pp. 120-141, 1958.
[76] R. Ottewill and M. J. Schick, "Nonionic surfactants," *Vol. 1Marcel Dekker, New York,* p. 657, 1967.
[77] D. Napper, "Flocculation studies of sterically stabilized dispersions," *Journal of Colloid and Interface Science,* vol. 32, pp. 106-114, 1970.
[78] D. Napper, "Flocculation studies of non-aqueous sterically stabilized dispersions of polymer," *Trans. Faraday Soc.,* vol. 64, pp. 1701-1711, 1968.
[79] D. Napper, "Steric stabilization and the Hofmeister series," *Journal of Colloid and Interface Science,* vol. 33, pp. 384-392, 1970.
[80] W. Heller and T. L. Pugh, "``Steric protection"of hydrophobic colloidal particles by adsorption of flexible macromolecules," *The Journal of Chemical Physics,* vol. 22, pp. 1778-1778, 1954.
[81] B. Vincent, Ed., *Coagulation kinetics and structure formation* Plenium press, NewYork and London,1987.
[82] Y. Borodko, S. M. Humphrey, T. D. Tilley, H. Frei, and G. A. Somorjai, "Charge-Transfer Interaction of Poly(vinylpyrrolidone) with Platinum and Rhodium Nanoparticles," *The Journal of Physical Chemistry C,* vol. 111, pp. 6288-6295, 2007/05/01 2007.
[83] C. Bock, H. Halvorsen, and B. MacDougall, "Catalyst Synthesis Techniques," in *PEM Fuel Cell Electrocatalysts and Catalyst Layers*, ed: Springer, 2008, pp. 447-485.
[84] H. Lee, C. Kim, S. Yang, J. W. Han, and J. Kim, "Shape-Controlled Nanocrystals for Catalytic Applications," *Catalysis Surveys from Asia,* vol. 16, pp. 14-27, 2012.
[85] T. Ahmadi, Z. Wang, A. Henglein, and M. El-Sayed, ""Cubic" colloidal platinum nanoparticles," *Chemistry of Materials,* vol. 8, pp. 1161-1163, 1996.
[86] C.-W. Chen, D. Tano, and M. Akashi, "Colloidal platinum nanoparticles stabilized by vinyl polymers with amide side chains: Dispersion stability and catalytic activity in aqueous electrolyte solutions," *Journal of Colloid and Interface Science,* vol. 225, pp. 349-358, 2000.

[87] W. Yang, Y. Ma, J. Tang, and X. Yang, ""Green synthesis" of monodisperse Pt nanoparticles and their catalytic properties," *Colloids and Surfaces A: Physicochemical and Engineering Aspects,* vol. 302, pp. 628-633, 2007.
[88] Z. Liu and S. P. Jiang, "Synthesis of PDDA–Pt nanoparticles for the self-assembly of electrode/Nafion membrane interface of polymer electrolyte fuel cells," *Journal of Power Sources,* vol. 159, pp. 55-58, 2006.
[89] A. Miyazaki and Y. Nakano, "Morphology of platinum nanoparticles protected by poly (N-isopropylacrylamide)," *Langmuir,* vol. 16, pp. 7109-7111, 2000.
[90] I. Burgess, C. A. Jeffrey, X. Cai, G. Szymanski, Z. Galus, and J. Lipkowski, "Direct Visualization of the Potential-Controlled Transformation of Hemimicellar Aggregates of Dodecyl Sulfate into a Condensed Monolayer at the Au(111) Electrode Surface," *Langmuir,* vol. 15, pp. 2607-2616, 1999/04/01 1999.
[91] C. Gutig, B. P. Grady, and A. Striolo, "Experimental studies on the adsorption of two surfactants on solid-aqueous interfaces: adsorption isotherms and kinetics," *Langmuir,* vol. 24, pp. 4806-4816, 2008.
[92] S. Hahakura, S. Isoda, T. Ogawa, S. Moriguchi, and T. Kobayashi, "Formation of ultrafine platinum particles in an aqueous solution with a surfactant," *Journal of Crystal Growth,* vol. 237–239, Part 3, pp. 1942-1945, 2002.
[93] S. H. H. Lee, S. Kweskin, D. Butcher, G. Samorjai and P. Yang, *Angew. Chem. Int. Ed.,* vol. 45, 2006.
[94] R. Guidelli and M. L. Foresti, "The inhibitory effect of neutral organic surfactants upon simple electrode reactions," *Journal of Electroanalytical Chemistry and Interfacial Electrochemistry,* vol. 77, pp. 73-96, 1977.
[95] R. Guidelli, M. L. Foresti, and M. R. Moncelli, "On the inhibitory effect of neutral organic surfactants upon simple electrode reactions at high surface coverages," *Journal of Electroanalytical Chemistry and Interfacial Electrochemistry,* vol. 113, pp. 171-191, 1980.
[96] Z. Liu, M. Shamsuzzoha, E. T. Ada, W. M. Reichert, and D. E. Nikles, "Synthesis and activation of Pt nanoparticles with controlled size for fuel cell electrocatalysts," *Journal of Power Sources,* vol. 164, pp. 472-480, 2007.
[97] M. Chen, I. Burgess, and J. Lipkowski, "Potential controlled surface aggregation of surfactants at electrode surfaces–A molecular view," *Surface Science,* vol. 603, pp. 1878-1891, 2009.
[98] M. Jaschke, H. J. Butt, H. E. Gaub, and S. Manne, "Surfactant Aggregates at a Metal Surface," *Langmuir,* vol. 13, pp. 1381-1384, 1997/03/01 1997.
[99] Y.-H. Chung, D. Y. Chung, N. Jung, and Y.-E. Sung, "Tailoring the Electronic Structure of Nanoelectrocatalysts Induced by a Surface-Capping Organic Molecule for the Oxygen Reduction Reaction," *The Journal of Physical Chemistry Letters,* vol. 4, pp. 1304-1309, 2013.
[100] Z.-Y. Zhou, X. Kang, Y. Song, and S. Chen, "Ligand-mediated electrocatalytic activity of Pt nanoparticles for oxygen reduction reactions," *The Journal of Physical Chemistry C,* vol. 116, pp. 10592-10598, 2012.
[101] S. Cavaliere, F. Raynal, A. Etcheberry, M. Herlem, and H. Perez, "Direct electrocatalytic activity of capped platinum nanoparticles toward oxygen reduction," *Electrochemical and solid-state letters,* vol. 7, pp. A358-A360, 2004.
[102] S. Cavaliere-Jaricot, A. Etcheberry, M. Herlem, V. Noël, and H. Perez, "Electrochemistry at capped platinum nanoparticle Langmuir Blodgett films: A study of the influence of platinum amount and of number of LB layers," *Electrochimica Acta,* vol. 52, pp. 2285-2293, 2007.

[103] J. Turkevich, P. C. Stevenson, and J. Hillier, "A study of the nucleation and growth processes in the synthesis of colloidal gold," *Discussions of the Faraday Society,* vol. 11, pp. 55-75, 1951.
[104] J. Turkevich, P. C. Stevenson, and J. Hillier, "The formation of colloidal gold," *The Journal of Physical Chemistry,* vol. 57, pp. 670-673, 1953.
[105] G. Frens, *Nat. Phys. Sci,* vol. 241, pp. 20-22, 1973.
[106] H. Lee, S. E. Habas, S. Kweskin, D. Butcher, G. A. Somorjai, and P. Yang, "Morphological Control of Catalytically Active Platinum Nanocrystals," *Angewandte Chemie,* vol. 118, pp. 7988-7992, 2006.
[107] G. N. Glavee, K. J. Klabunde, C. M. Sorensen, and G. C. Hadjipanayis, "Borohydride reduction of nickel and copper ions in aqueous and nonaqueous media. Controllable chemistry leading to nanoscale metal and metal boride particles," *Langmuir,* vol. 10, pp. 4726-4730, 1994.
[108] G. N. Glavee, K. J. Klabunde, C. M. Sorensen, and G. C. Hadjipanayis, "Borohydride reduction of cobalt ions in water. Chemistry leading to nanoscale metal, boride, or borate particles," *Langmuir,* vol. 9, pp. 162-169, 1993.
[109] A. B. Mayer, J. E. Mark, and S. H. Hausner, "Colloidal platinum-polyacid nanocatalyst systems," *Die Angewandte Makromolekulare Chemie,* vol. 259, pp. 45-53, 1998.
[110] V. K. LaMer and R. H. Dinegar, "Theory, production and mechanism of formation of monodispersed hydrosols," *Journal of the American Chemical Society,* vol. 72, pp. 4847-4854, 1950.
[111] H. Reiss, "The growth of uniform colloidal dispersions," *The Journal of Chemical Physics,* vol. 19, p. 482, 1951.
[112] H. Ataee-Esfahani, L. Wang, Y. Nemoto, and Y. Yamauchi, "Synthesis of bimetallic Au@ Pt nanoparticles with Au core and nanostructured Pt shell toward highly active electrocatalysts," *Chemistry of Materials,* vol. 22, pp. 6310-6318, 2010.
[113] L. Lu, G. Sun, H. Zhang, H. Wang, S. Xi, J. Hu, Z. Tian, and R. Chen, "Fabrication of core-shell Au-Pt nanoparticle film and its potential application as catalysis and SERS substrate," *J. Mater. Chem.,* vol. 14, pp. 1005-1009, 2004.
[114] C.-J. Zhong, J. Luo, B. Fang, B. N. Wanjala, P. N. Njoki, R. Loukrakpam, and J. Yin, "Nanostructured catalysts in fuel cells," *Nanotechnology,* vol. 21, p. 062001, 2010.
[115] D. García-Gutiérrez, C. Gutiérrez-Wing, M. Miki-Yoshida, and M. José-Yacamán, "HAADF study of Au-Pt core-shell bimetallic nanoparticles," *Applied Physics A,* vol. 79, pp. 481-487, 2004.
[116] N. Braidy, G. R. Purdy, and G. A. Botton, "Equilibrium and stability of phase-separating Au–Pt nanoparticles," *Acta Materialia,* vol. 56, pp. 5972-5983, 2008.
[117] G. Schmid, A. Lehnert, J. O. Malm, and J. O. Bovin, "Ligand-Stabilized Bimetallic Colloids Identified by HRTEM and EDX," *Angewandte Chemie International Edition in English,* vol. 30, pp. 874-876, 1991.
[118] A. BRZANA, B. CARR, M. WRIGHT, A. MALLOY, P. HOLE, and J. SMITH, "THE REAL-TIME AND DIRECT MULTI-PARAMETER ANALYSIS OF INDIVIDUAL NANO-PARTICLES IN SOLUTION," ed: Nanocon, 2009.
[119] R. Pecora, *Dynamic light scattering: applications of photon correlation spectroscopy*: Springer, 1985.
[120] W. Winter, "Measurement of suspended particles by quasi-elastic light scattering, Barton E. Dahneke, Ed., Wiley, New York, 1983, 570 pp. Price: $39.95," *Journal of Polymer Science: Polymer Letters Edition,* vol. 21, pp. 1020-1020, 1983.

[121] L. D'Souza, A. Suchopar, and R. M. Richards, "In situ approaches to establish colloidal growth kinetics," *Journal of Colloid and Interface Science,* vol. 279, pp. 458-463, 2004.
[122] R. D. Boyd, S. K. Pichaimuthu, and A. Cuenat, "New approach to inter-technique comparisons for nanoparticle size measurements; using atomic force microscopy, nanoparticle tracking analysis and dynamic light scattering," *Colloids and Surfaces A: Physicochemical and Engineering Aspects,* vol. 387, pp. 35-42, 2011.
[123] R. Finsy, "Particle sizing by quasi-elastic light scattering," *Advances in Colloid and Interface Science,* vol. 52, pp. 79-143, 1994.
[124] W. Anderson, D. Kozak, V. A. Coleman, Å. K. Jämting, and M. Trau, "A comparative study of submicron particle sizing platforms: Accuracy, precision and resolution analysis of polydisperse particle size distributions," *Journal of Colloid and Interface Science,* vol. 405, pp. 322-330, 2013.
[125] W. Rasband. (2007, 2007). ImageJ. *Software*.
[126] K. Kendall and M. R. Kosseva, "Nanoparticle aggregation influenced by magnetic fields," *Colloids and Surfaces A: Physicochemical and Engineering Aspects,* vol. 286, pp. 112-116, 2006.
[127] C. M. Hoo, N. Starostin, P. West, and M. L. Mecartney, "A comparison of atomic force microscopy (AFM) and dynamic light scattering (DLS) methods to characterize nanoparticle size distributions," *Journal of Nanoparticle Research,* vol. 10, pp. 89-96, 2008.
[128] J. Turkevich, "Colloidal gold. Part II," *Gold Bulletin,* vol. 18, pp. 125-131, 1985.
[129] S. Diegoli, A. L. Manciulea, S. Begum, I. P. Jones, J. R. Lead, and J. A. Preece, "Interaction between manufactured gold nanoparticles and naturally occurring organic macromolecules," *Science of The Total Environment,* vol. 402, pp. 51-61, 2008.
[130] G. Mie, "Articles on the optical characteristics of turbid tubes, especially colloidal metal solutions," *Ann. Phys,* vol. 25, pp. 377-445, 1908.
[131] S. Eustis and M. A. El-Sayed, "Why gold nanoparticles are more precious than pretty gold: noble metal surface plasmon resonance and its enhancement of the radiative and nonradiative properties of nanocrystals of different shapes," *Chemical Society Reviews,* vol. 35, pp. 209-217, 2006.
[132] H. Wang, C. S. Levin, and N. J. Halas, "Nanosphere arrays with controlled sub-10-nm gaps as surface-enhanced Raman spectroscopy substrates," *Journal of the American Chemical Society,* vol. 127, pp. 14992-14993, 2005.
[133] Y. Abate, A. Schwartzberg, D. Strasser, and S. R. Leone, "Nanometer-scale size dependent imaging of cetyl trimethyl ammonium bromide (CTAB) capped and uncapped gold nanoparticles by apertureless near-field optical microscopy," *Chemical Physics Letters,* vol. 474, pp. 146-152, 2009.
[134] E. C. Dreaden, L. A. Austin, M. A. Mackey, and M. A. El-Sayed, "Size matters: gold nanoparticles in targeted cancer drug delivery," *Therapeutic delivery,* vol. 3, pp. 457-478, 2012.
[135] D. T. Tran, "GOLD-CONTAINING BIMETALLIC NANOPARTICLES," PhD, School of Metallurgy and Materials,University of Birmingham, 2010.
[136] A. Henglein, "Preparation and Optical Aborption Spectra of AucorePtshell and PtcoreAushell Colloidal Nanoparticles in Aqueous Solution," *The Journal of Physical Chemistry B,* vol. 104, pp. 2201-2203, 2000/03/01 2000.
[137] J. Fennell, D. He, A. M. Tanyi, A. J. Logsdail, R. L. Johnston, Z. Y. Li, and S. L. Horswell, "A Selective Blocking Method To Control the Overgrowth of Pt on Au

Nanorods," *Journal of the American Chemical Society,* vol. 135, pp. 6554-6561, 2013/05/01 2013.
[138] S. Foiles, M. Baskes, and M. Daw, "Embedded-atom-method functions for the fcc metals Cu, Ag, Au, Ni, Pd, Pt, and their alloys," *Physical Review B,* vol. 33, p. 7983, 1986.
[139] C. Kittel, "Introduction to Solid State Physics . USA: John Willey & Sons," ed: Inc, 1996.
[140] A. J. Bard and R. Faulkner L, *Electrochemical Methods: Fundamentals and Applications*: Wiley, New York, 2001.
[141] E. J. Biddinger, D. von Deak, H. S. Marsh, and U. S. Ozkan, "RRDE catalyst ink aging effects on selectivity to water formation in ORR," *Electrochemical and solid-state letters,* vol. 13, pp. B98-B100, 2010.
[142] M. Inaba, H. Yamada, J. Tokunaga, and A. Tasaka, "Effect of agglomeration of Pt/C catalyst on hydrogen peroxide formation," *Electrochemical and solid-state letters,* vol. 7, pp. A474-A476, 2004.
[143] A. Ohma, K. Fushinobu, and K. Okazaki, "Influence of Nafion< sup>®</sup> film on oxygen reduction reaction and hydrogen peroxide formation on Pt electrode for proton exchange membrane fuel cell," *Electrochimica Acta,* vol. 55, pp. 8829-8838, 2010.
[144] W. Albery and S. Bruckenstein, "Ring-disc electrodes. Part 2.—Theoretical and experimental collection effciencies," *Trans. Faraday Soc.,* vol. 62, pp. 1920-1931, 1966.
[145] U. Paulus, T. Schmidt, H. Gasteiger, and R. Behm, "Oxygen reduction on a high-surface area Pt/Vulcan carbon catalyst: a thin-film rotating ring-disk electrode study," *Journal of Electroanalytical Chemistry,* vol. 495, pp. 134-145, 2001.
[146] Y. Garsany, O. A. Baturina, K. E. Swider-Lyons, and S. S. Kocha, "Experimental Methods for Quantifying the Activity of Platinum Electrocatalysts for the Oxygen Reduction Reaction," *Analytical Chemistry,* vol. 82, pp. 6321-6328, 2010/08/01 2010.
[147] J. S. Jirkovský, M. Halasa, and D. J. Schiffrin, "Kinetics of electrocatalytic reduction of oxygen and hydrogen peroxide on dispersed gold nanoparticles," *Physical Chemistry Chemical Physics,* vol. 12, pp. 8042-8053, 2010.
[148] N. Wakabayashi, M. Takeichi, M. Itagaki, H. Uchida, and M. Watanabe, "Temperature-dependence of oxygen reduction activity at a platinum electrode in an acidic electrolyte solution investigated with a channel flow double electrode," *Journal of Electroanalytical Chemistry,* vol. 574, pp. 339-346, 2005.
[149] A. J. Bard and L. R. Faulkner, *Electrochemical methods: fundamentals and applications* vol. 2: Wiley New York, 1980.
[150] www.pineinst.com/echem/files/RRDE_EFFICIENCY.XLS
[151] N. M. Marković and P. N. Ross Jr, "Surface science studies of model fuel cell electrocatalysts," *Surface Science Reports,* vol. 45, pp. 117-229, 2002.
[152] A. Rodes, K. El Achi, M. Zamakhchari, and J. Clavilier, "Hydrogen probing of step and terrace sites on Pt (S)-[< i> n</i>(111)×(100)]," *Journal of Electroanalytical Chemistry and Interfacial Electrochemistry,* vol. 284, pp. 245-253, 1990.
[153] J. Clavilier, K. E. Actii, M. Petit, A. Rodes, and M. Zamakhchari, "Electrochemical monitoring of the thermal reordering of platinum single-crystal surfaces after metallographic polishing from the early stage to the equilibrium surfaces," *Journal of Electroanalytical Chemistry and Interfacial Electrochemistry,* vol. 295, pp. 333-356, 1990.

[154] G. A. Attard, J. E. Gillies, C. A. Harris, D. J. Jenkins, P. Johnston, M. A. Price, D. J. Watson, and P. B. Wells, "Electrochemical evaluation of the morphology and enantioselectivity of Pt/graphite," *Applied Catalysis A: General,* vol. 222, pp. 393-405, 2001.
[155] G. A. Attard, J.-Y. Ye, P. Jenkins, F. J. Vidal-Iglesias, E. Herrero, and S.-G. Sun, "Citrate adsorption on Pt {hkl} electrodes and its role in the formation of shaped Pt nanoparticles," *Journal of Electroanalytical Chemistry,* vol. 688, pp. 249-256, 2013.
[156] J. Solla-Gullón, P. Rodríguez, E. Herrero, A. Aldaz, and J. M. Feliu, "Surface characterization of platinum electrodes," *Physical Chemistry Chemical Physics,* vol. 10, pp. 1359-1373, 2008.
[157] F. J. Vidal-Iglesias, R. M. Arán-Ais, J. Solla-Gullón, E. Herrero, and J. M. Feliu, "Electrochemical characterization of shape-controlled Pt nanoparticles in different supporting electrolytes," *ACS Catalysis,* vol. 2, pp. 901-910, 2012.
[158] T. Schmidt, H. Gasteiger, G. Stäb, P. Urban, D. Kolb, and R. Behm, "Characterization of High-Surface-Area Electrocatalysts Using a Rotating Disk Electrode Configuration," *Journal of the Electrochemical Society,* vol. 145, pp. 2354-2358, 1998.
[159] H. A. Gasteiger, S. S. Kocha, B. Sompalli, and F. T. Wagner, "Activity benchmarks and requirements for Pt, Pt-alloy, and non-Pt oxygen reduction catalysts for PEMFCs," *Applied Catalysis B: Environmental,* vol. 56, pp. 9-35, 2005.
[160] J. Robinson, R. Greef, R. Peat, L. Peter, and D. Pletcher, "Instrumental Methods in Electrochemistry," ed: Ellis Horwood, 1993.
[161] T. Schmidt, *HA Gasteiger in Handbook of Fuel Cells–Fundamentals, Technology and Applications, W. Vielstich, A. Lamm, HA Gasteiger, Editors, Vol. 2* vol. 2: John Wiley & Sons, Hoboken, New Jersey, 2003.
[162] R. R. Adžić and J. X. Wang, "Structures of surface adlayers and oxygen reduction kinetics," *Solid State Ionics,* vol. 150, pp. 105-114, 2002.
[163] N. A. Anastasijević, V. Vesović, and R. R. Adžić, "Determination of the kinetic parameters of the oxygen reduction reaction using the rotating ring-disk electrode: Part II. Applications," *Journal of Electroanalytical Chemistry and Interfacial Electrochemistry,* vol. 229, pp. 317-325, 1987.
[164] N. Anastasijević, V. Vesović, and R. Adžić, "Determination of the kinetic parameters of the oxygen reduction reaction using the rotating ring-disk electrode: Part I. Theory," *Journal of Electroanalytical Chemistry and Interfacial Electrochemistry,* vol. 229, pp. 305-316, 1987.
[165] A. Damjanovic, M. Genshaw, and J. M. Bockris, "Distinction between intermediates produced in main and side electrodic reactions," *The Journal of Chemical Physics,* vol. 45, p. 4057, 1966.
[166] D. Sepa, M. Vojnovic, L. M. Vracar, and A. Damjanovic, "Different views regarding the kinetics and mechanisms of oxygen reduction at Pt and Pd electrodes," *Electrochimica Acta,* vol. 32, pp. 129-134, 1987.
[167] N. M. Marković, R. R. Adžić, B. D. Cahan, and E. B. Yeager, "Structural effects in electrocatalysis: oxygen reduction on platinum low index single-crystal surfaces in perchloric acid solutions," *Journal of Electroanalytical Chemistry,* vol. 377, pp. 249-259, 1994.
[168] A. J. Bard, "Inner-sphere heterogeneous electrode reactions. Electrocatalysis and photocatalysis: the challenge," *Journal of the American Chemical Society,* vol. 132, pp. 7559-7567, 2010.

[169] M. Arenz and N. M. Markovic, "Half-Cell Investigations of Cathode Catalysts for PEM Fuel Cells: From Model Systems to High-Surface-Area Catalysts," *Fuel Cell Science: Theory, Fundamentals, and Biocatalysis,* vol. 4, p. 283, 2011.
[170] E. Claude, T. Addou, J.-M. Latour, and P. Aldebert, "A new method for electrochemical screening basedon the rotating ring disc electrode and its applicationto oxygen reduction catalysts," *Journal of applied electrochemistry,* vol. 28, pp. 57-64, 1998.
[171] N. M. Markovic, H. A. Gasteiger, and P. N. Ross Jr, "Oxygen reduction on platinum low-index single-crystal surfaces in sulfuric acid solution: rotating ring-Pt (hkl) disk studies," *The Journal of Physical Chemistry,* vol. 99, pp. 3411-3415, 1995.
[172] S. A. M. van Stroe-Biezen, F. M. Everaerts, L. J. J. Janssen, and R. A. Tacken, "Diffusion coefficients of oxygen, hydrogen peroxide and glucose in a hydrogel," *Analytica Chimica Acta,* vol. 273, pp. 553-560, 1993.
[173] M. Hitchman, T. Elbing, and J. Winefordner, "Chemical Analysis," *Measurement of Dissolved Oxygen,* vol. 49, 1978.
[174] M. Tarasevich, A. Sadkowski, and E. Yeager, "Kinetics and mechanisms of electrode processes," *Comprehensive Treatise of Electrochemistry,* vol. 7, pp. 301-398, 1983.
[175] D. Sepa, M. Vojnovic, and A. Damjanovic, "Reaction intermediates as a controlling factor in the kinetics and mechanism of oxygen reduction at platinum electrodes," *Electrochimica Acta,* vol. 26, pp. 781-793, 1981.
[176] I. Takahashi and S. S. Kocha, "Examination of the activity and durability of PEMFC catalysts in liquid electrolytes," *Journal of Power Sources,* vol. 195, pp. 6312-6322, 2010.
[177] N. Marković and P. Ross Jr, "Surface science studies of model fuel cell electrocatalysts," *Surface Science Reports,* vol. 45, pp. 117-229, 2002.
[178] N. Alexeyeva, K. Tammeveski, A. Lopez-Cudero, J. Solla-Gullón, and J. Feliu, "Electroreduction of oxygen on Pt nanoparticle/carbon nanotube nanocomposites in acid and alkaline solutions," *Electrochimica Acta,* vol. 55, pp. 794-803, 2010.
[179] S. Park, S. A. Wasileski, and M. J. Weaver, "Electrochemical infrared characterization of carbon-supported platinum nanoparticles: A benchmark structural comparison with single-crystal electrodes and high-nuclearity carbonyl clusters," *The Journal of Physical Chemistry B,* vol. 105, pp. 9719-9725, 2001.
[180] B. Grgur, N. Markovic, and P. Ross, "Electrooxidation of H2, CO, and H2/CO mixtures on a well-characterized Pt70Mo30 bulk alloy electrode," *The Journal of Physical Chemistry B,* vol. 102, pp. 2494-2501, 1998.
[181] A. López-Cudero, J. Solla-Gullón, E. Herrero, A. Aldaz, and J. M. Feliu, "CO electrooxidation on carbon supported platinum nanoparticles: Effect of aggregation," *Journal of Electroanalytical Chemistry,* vol. 644, pp. 117-126, 2010.
[182] F. Gloaguen, P. Convert, S. Gamburzev, O. Velev, and S. Srinivasan, "An evaluation of the macro-homogeneous and agglomerate model for oxygen reduction in PEMFCs," *Electrochimica Acta,* vol. 43, pp. 3767-3772, 1998.
[183] J. Perez, E. Gonzalez, and E. Ticianelli, "Oxygen electrocatalysis on thin porous coating rotating platinum electrodes," *Electrochimica Acta,* vol. 44, pp. 1329-1339, 1998.
[184] O. J. Curnick, "Ionomer-stabilised Pt and Pt-Ti bimetallic electrocatalysts for the proton exchange membrane fuel cell," University of Birmingham, 2012.

[185] N. M. Marković, C. A. Lucas, H. A. Gasteiger, and P. N. Ross, "Bromide adsorption on Pt(100): rotating ring-Pt(100) disk electrode and surface X-ray scattering measurements," *Surface Science,* vol. 365, pp. 229-240, 1996.
[186] O. Antoine and R. Durand, "RRDE study of oxygen reduction on Pt nanoparticles inside Nafion®: H2O2 production in PEMFC cathode conditions," *Journal of applied electrochemistry,* vol. 30, pp. 839-844, 2000.
[187] K. L. Hsueh, D. T. Chin, and S. Srinivasan, "Electrode kinetics of oxygen reduction: A theoretical and experimental analysis of the rotating ring-disc electrode method," *Journal of Electroanalytical Chemistry and Interfacial Electrochemistry,* vol. 153, pp. 79-95, 1983.
[188] J. Wu, X. Z. Yuan, J. J. Martin, H. Wang, J. Zhang, J. Shen, S. Wu, and W. Merida, "A review of PEM fuel cell durability: degradation mechanisms and mitigation strategies," *Journal of Power Sources,* vol. 184, pp. 104-119, 2008.
[189] K. J. J. Mayrhofer, J. C. Meier, S. J. Ashton, G. K. H. Wiberg, F. Kraus, M. Hanzlik, and M. Arenz, "Fuel cell catalyst degradation on the nanoscale," *Electrochemistry Communications,* vol. 10, pp. 1144-1147, 2008.
[190] M. J. Rosen and M. Dahanayake, *Industrial utilization of surfactants: principles and practice*: AOCS press Champaign, IL, 2000.
[191] R. J. Hunter, *Introduction to modern colloid science* vol. 7: Oxford University Press Oxford, 1993.
[192] K. Matsuzawa, T. Fukushima, and M. Inaba, "Shape-Controlled Platinum Nanoparticles of Different Sizes and Their Electrochemical Properties," *Electrocatalysis,* vol. 1, pp. 169-177, 2010/09/01 2010.
[193] A. Toge, T. Yokono, M. Saito, H. Daimon, A. Tasaka, and M. Inaba, "Oxygen Reduction Reaction Activity of Shape Controlled Pt Catalysts," *ECS Transactions,* vol. 41, pp. 2283-2288, 2011.
[194] E. Antolini, L. Giorgi, A. Pozio, and E. Passalacqua, "Influence of Nafion loading in the catalyst layer of gas-diffusion electrodes for PEFC," *Journal of Power Sources,* vol. 77, pp. 136-142, 1999.
[195] M. Uchida, Y. Aoyama, N. Eda, and A. Ohta, "New Preparation Method for Polymer-Electrolyte Fuel Cells," *Journal of the Electrochemical Society,* vol. 142, pp. 463-468, 1995.
[196] X.-Z. Yuan, *Electrochemical impedance spectroscopy in PEM fuel cells: fundamentals and applications*: Springer, 2010.
[197] S. Zhang, X.-Z. Yuan, J. N. C. Hin, H. Wang, J. Wu, K. A. Friedrich, and M. Schulze, "Effects of open-circuit operation on membrane and catalyst layer degradation in proton exchange membrane fuel cells," *Journal of Power Sources,* vol. 195, pp. 1142-1148, 2010.
[198] M. Moein-Jahromi and M. Kermani, "Performance prediction of PEM fuel cell cathode catalyst layer using agglomerate model," *International Journal of Hydrogen Energy,* vol. 37, pp. 17954-17966, 2012.
[199] M. Uchida, Y. Aoyama, N. Eda, and A. Ohta, "Investigation of the Microstructure in the Catalyst Layer and Effects of Both Perfluorosulfonate Ionomer and PTFE-Loaded Carbon on the Catalyst Layer of Polymer Electrolyte Fuel Cells," *Journal of the Electrochemical Society,* vol. 142, pp. 4143-4149, 1995.
[200] D. Rohendi, E. H. Majlan, A. B. Mohamad, W. R. Wan Daud, A. A. Hassan Kadhum, and L. K. Shyuan, "Characterization of electrodes and performance tests on MEAs with varying platinum content and under various operational conditions," *International Journal of Hydrogen Energy,* vol. 38, pp. 9431-9437, 2013.

[201] X. Zhang, S. W. Tay, L. Hong, and Z. Liu, "< i> In situ</i> implantation of PolyPOSS blocks in Nafion< sup>®</sup> matrix to promote its performance in direct methanol fuel cell," *Journal of Membrane Science,* vol. 320, pp. 310-318, 2008.
[202] T. Sakai, H. Takenaka, and E. Torikai, "Gas diffusion in the dried and hydrated Nafions," *Journal of the Electrochemical Society,* vol. 133, pp. 88-92, 1986.
[203] http://www.sigmaaldrich.com/catalog/product/aldrich/521078.
[204] L. Li, A. H. Larsen, N. A. Romero, V. A. Morozov, C. Glinsvad, F. Abild-Pedersen, J. Greeley, K. W. Jacobsen, and J. K. Nørskov, "Investigation of Catalytic Finite-Size-Effects of Platinum Metal Clusters," *The Journal of Physical Chemistry Letters,* vol. 4, pp. 222-226, 2012.